Modelling displacement and stress fields in hydrothermal regions: the case of a thermo-poro-elastic inclusion in a poro-elastic half-space

Relatore:
Prof.ssa Maria Elina Belardinelli

Correlatori:
Prof. Maurizio Bonafede
Dott. Massimo Nespoli

Presentata da:
Lorenzo Mantiloni

Sommario

Le regioni idrotermali sono interessate da una grande varietà di fenomeni naturali, tra cui episodi di rigonfiamento e subsidenza del suolo. Tra di esse, le caldere offrono l'occasione di studiare le complesse interazioni tra i processi magmatici in profondità e le dinamiche dei fluidi di cui sono imbevute le rocce porose nella crosta superficiale. Oltre a questo, le caldere rappresentano uno dei maggiori pericoli derivanti da eventi naturali sul pianeta, e ciò rende lo studio del loro comportamento e delle loro caratteristiche di grande importanza.

Una di queste aree idrotermali soggette a instabilità periodiche è la caldera dei Campi Flegrei, nell'Italia meridionale. Una delle crisi più recenti ha avuto luogo tra il 1982 e il 1984, e sia la sua evoluzione che le sue potenziali cause sono state oggetto di numerosi studi e ricerche, che hanno visto l'applicazione di diversi modelli di sorgenti deformative nel tentativo di riprodurre i dati della deformazione osservata in superficie e dell'attività sismica del periodo.

Questa tesi si propone lo scopo di introdurre un modello di sorgente deformativa che prevede una regione termo-poro-elastica inclusa in un solido poro-elastico semi-illimitato, e svilupparlo nel caso in cui questa regione abbia forma cilindrica e subisca cambiamenti di temperatura e pressione di poro al suo interno. Viene fornita una soluzione semi-analitica per i campi di spostamento e sforzi così generati sia all'interno che all'esterno della sorgente deformativa, e i risultati sono paragonati a quelli ottenuti tramite un approccio completamente numerico, insieme a quelli di altri tre modelli.

Lo spostamento verticale risultante alla superficie libera è in buon accordo con quello prodotto dal modello di Mogi, e riproduce il pattern di deformazione verticale osservato presso i Campi Flegrei durante la crisi del 1982-84. Tuttavia, vi sono delle differenze nelle ampiezze delle componenti dello spostamento tra il nostro modello e gli altri due considerati. I risultati per il campo di sforzi sul piano mediano della sorgente indicano un regime di sforzo compressivo al suo interno, mentre si evidenzia un regime distensivo nella regione al di sopra fino alla superficie libera, e un regime trascorrente nella regione esterna del semispazio. Questo è in accordo con la distribuzione eterogenea dei meccanismi focali ottenuti dai dati sismologici relativi allo stesso episodio presso i Campi Flegrei.

Alla fine dell'opera, sono discussi i limiti di applicabilità del modello e ne sono indicati alcuni possibili sviluppi ulteriori.

Abstract

Hydrothemal regions are affected by a wide variety of phenomena, including ground inflation and deflation episodes. Among them, calderas offer the opportunity to study the complex interaction between magmatic processes at depth and permeable rocks filled with fluids in the upper crust. In addition to this, they also represent one of the most relevant natural hazards on the planet, making the understanding of their features and dynamics even more important.

One of such hydrothermal areas is the Campi Flegrei caldera in southern Italy. One of the most recent episodes of unrest took place between 1982 and 1984, and a lot of research has been conducted into its unfolding and its causes, seeing the application of different deformation source models to reproduce the observed data of ground displacement and seismicity.

The present work aims at introducing a source model consisting of a thermo-poro-elastic region embedded in a homogeneous semi-infinite poro-elastic medium, and developing it for the case where the region has the shape of a cylinder and undergoes changes in temperature and pore pressure. A semi-analytical solution for the displacement and stress fields both within and outside the source is provided, and comparisons are made between these results and those obtained through a fully numerical approach, as well as those of three other source models.

The resulting uplift at the free surface is in good agreement with that of the Mogi source model, and it approximates the pattern of the vertical ground deformation recorded during the 1982-84 Campi Flegrei unrest episode. However, there are differences in the amplitudes of the displacement field components between our model and the other two considered. Results for the stress field on the median plane of the source suggest a compressive stress environment in its interior, while a distensive regime is highlighted in the region above the source up to the free surface and a strike-slip environment extends over the outer regions of the half-space, in agreement with the heterogeneous distribution of focal mechanisms retrieved from the seismic data accompanying the above-mentioned unrest episode.

In the end, the limits of applicability of the model are discussed, and further developments are proposed.

Introduction

Volcanic areas are home to some of the most fascinating and hazardous natural phenomena that can be experienced on our planet. Among them, caldera regions are affected by a variety of complex and, in most cases, still poorly understood magmatic and hydrothermal activities.

The interplay between deep magmatic intrusions and the surrounding media, which are often permeable and filled with fluids of different nature, can lead to a wide range of surface manifestations, such as degassing, hot springs, fumaroles and considerable ground deformation on relatively short timescales. In addition, the presence of magmatic activity at shallow depths poses a major hazard to the whole region hosting the caldera, as these areas are known to have caused some of the biggest eruptions in geological history all over the world.

It is thereby of great scientific and social relevance to advance the research on the processes in which these regions are involved, and in order to do that, there is a need for more complex and accurate theoretical models to describe and reproduce the data sets collected on the ground.

The purpose of this work is to discuss a deformation source model to be applied to the description of ground displacement in hydrothermal regions, consisting of a cylinder-shaped thermo-poro-elastic inclusion embedded in a semi-infinite poro-elastic solid.

The analytical solutions for the displacement and stress fields within such an inclusion have already been provided by Lamberti (2017) for the case of an infinite space. What we want to attempt is to develop the same model assuming a space bounded by a free surface, thus analyzing the displacement and stress fields produced both on it and at different depths.

Furthermore, we want to compare the results we will obtain to those of other simple source models typically employed to fit surface deformation data in volcanic areas. In order to validate our results, we will discuss them in the light of a particular case study: the Campi Flegrei caldera in southern Italy. The area is known to have experienced several cycles of inflation and deflation over the centuries and even in very recent times, and it was affected by a well-studied phase of unrest, characterized by increased seismicity and ground uplift, between 1982 and 1984.

We will focus our attention on the pattern of the ground displacement recorded at that time, together with the models that have been proposed to explain the phenomenon in terms of magmatic and hydrothermal processes, and we will try to understand how our model could fit into such a complex case.

The work will be divided into five chapters with an additional appendix, and their plan will be the following:

- The first chapter will be devoted to the introduction and description of the

Campi Flegrei caldera, with particular attention on its geological features and the characteristics of the 1982-84 and more recent unrest episodes. We will discuss some of the deformation source models proposed over the years and also the models used to describe its hydrothermal system. Finally, we will introduce the source model that will be developed throughout the rest of the work.

- The second chapter will lay out the theoretical premises and techniques we will use to provide a solution to our problem: namely, Eshelby's method will be explained, the representation of displacement fields by means of elastic Green's functions and the rheology of poro-elastic media will be discussed, and the Green's function for a half-space will be derived.

- The third chapter will describe in detail the characteristics of our deformation source and the parameters we will use in our model; then, it will provide a semi-analytical solution for the displacement and stress fields both within the inclusion and the surrounding medium. Results at the free surface will be presented and discussed as well, together with comparisons between them and the results obtained for the same case through a fully numerical model.

- The fourth chapter will compare our results to those of three other models assuming pressurized cavities at depth. Moreover, we will attempt to justify the assumptions we make with respect to more sofisticated models of hydrothermal regions, and we will discuss the possible applications of our model to the Campi Flegrei area.

- The fifth chapter will contain a summary of the work and its results, ending with some conclusive remarks.

Contents

Chapter 1

Modelling the unrest in hydrothermal regions

The purpose of this chapter is to give some insight into the geological phenomena that can occur in hydrothermal regions, such as calderas. These include ground deformation, changes in temperature, flux and chemical composition of the fluids exsolved from the ground and seismicity associated with changes in the stress field.

One of the most remarkable of such events is represented by bradyseisms: these are episodes of uplift or subsidence which can involve the surface of entire regions and produce significant, or even conspicuous, ground deformation (up to tens of meters of vertical displacement) in a relatively short time (from months to decades). This can occur for several geophysical reasons, none of which is easy to be identified and discriminated from others.

In the following sections, we will go through the phenomenology and the dynamics of these processes, and discuss how they can be understood and modeled in terms of deformation sources, taking the example of one of the most studied and monitored volcanic region in the world: the Campi Flegrei caldera.

1.1   Ground motion in hydrothermal areas

Hydrothermal regions are affected by a complex set of interactions in which water and other fluids circulate within the Earth's crust and transfer heat and mass towards the surface, usually involving the convection of hot waters through underground permeable media.

These phenomena are set in motion by the presence of some kind of igneous activity at a certain depth, be it a magma chamber linked to a volcanic vent or a crystallizing magmatic intrusion. For this reason, hydrothermal manifestations are often included among the examples of secondary volcanism. The water and the fluids involved in these processes can be derived directly from the cooling and crystallization of the magmatic body, or they can originate from external sources (for instance, groundwater of meteoric origin seeping down to the surroundings of the intrusion, and thus being heated).

The presence of a system of hot and pressurized fluids driven towards the surface through a complex network of cracks, faults and interconnected cavities makes the rocks more permeable, although the presence of impermeable layers is also possible. Hydrothermal regions are characterized by a wide variety of phenomena that can occur on relatively short timescales.

Moreover, as geothermal regions are a manifestation of volcanism, even if in most cases pertaining to volcanic systems which have shown no signs of activity for millennia or are regarded as extinct, they might pose a serious hazard to any population center present in their proximity.

Therefore, the study and the modelling of these regions and their dynamics are not only an interesting scientific topic, but also a very important issue to be addressed in order to improve our comprehension of volcanic hazard and the way it can be assessed.

Hydrothermal regions are found in many areas of the Earth's surface, both on the continents and on the ocean floor. In some cases, they are associated with large depressions, known as *calderas*, which often show a very complex geologic structure, and whose origin is to be attributed to the collapse of an ancient magma chamber after one or more major eruptive events. Calderas represent the most explosive volcanic areas on the Earth, and depending on the volume of magma involved in their eruptions, they are able to cause catastrophes affecting entire continents and alter the climate on a global scale.

The surface manifestations of hydrothermal activity, namely geysers, fumaroles and hot springs, are often found inside calderas, and the changes observed in their behaviour provide valuable evidence on the processes going on at depth. Furthermore, changes in the temperature and pressure of hydrothermal fluids flowing through porous rocks can lead to the deformation of the whole underground region affected by the phenomenon, and the consequences of this can result in gradual but significant ground displacement all over the area.

Such massive ground motion is referred to as *bradyseism*, a term derived from Greek meaning "slow movement", and it can be due not only to hydrothermal processes, but also to the filling or the emptying of a magma chamber, or to the emplacement of a new magmatic body. As as consequence, when dealing with episodes of uplift in areas known for having been affected by volcanic acitivity, it is of the utmost importance to discriminate between the two cases.

Bradyseisms have been observed in many volcanic regions all around the globe, and sometimes they have preceded or accompanied volcanic eruptions, although there are several historic records of episodes that seem to be part of cycles of inflation and deflation, which did not lead to eruptive events. Calderas, in particularly, are where the most remarkable bradyseisms can occur.

Notable examples of regions like these are the Yellowstone National Park and the Long Valley caldera in the U.S.A., but one of the most studied of such regions is the Campi Flegrei (Phlegraeans Fields) caldera in southern Italy: a veritable open air laboratory where it is possible to analyze and try to model a very complex interplay of geophysical processes involving seismic, volcanic, tectonic and hydrothermal activity.

1.2   The Campi Flegrei caldera

Campi Flegrei caldera is a volcanic district located in the Campania region in southern Italy: it covers a wide area on the coast north-west of Naples, containing even parts of the city itself. There is a wide scientific literature addressing the several
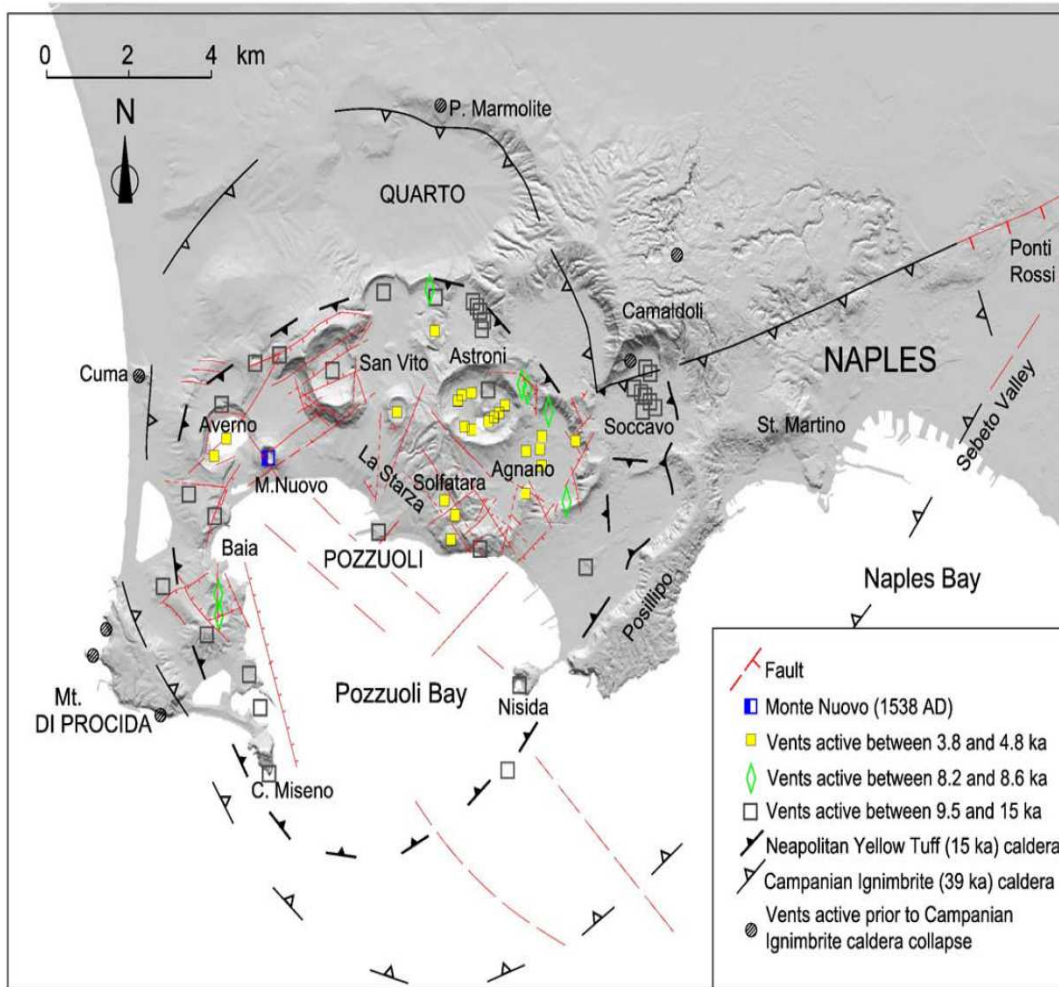
Figure 1.1: Location of Campi Flegrei caldera and its main morphological features, including the marine terrace named "La Starza", the nearby city of Pozzuoli, the Solfatara crater, Monte Nuovo and the volcanic vents which have been active in the past (after Moretti et al., 2013).

aspects of this area from different points of view, and a long series of historic records of the events it has been involved in.

The caldera is characterized by a complex morphological structure and is partially submerged. As reported in fig. (1.1), it shows a broadly circular symmetry, bounded to the east by the hills of Posillipo and Camaldoli, and to the west by the reliefs of Monte Procida. Its center can be identified with a raised marine terrace, named "La Starza", while its southern half is currently below sea level and defines the Gulf of Pozzuoli.

Exhaustive descriptions of the structure of Campi Flegrei have been provided by many authors (e.g. D'Auria et al., 2014 and De Vivo, 2006).

A brief history

Volcanic activity has occurred in Campi Flegrei since 47.000 years ago (De Vivo, 2006), but the origin of its current shape is most likely due to two major eruptive episodes. The oldest one, known as the Campanian Ignimbrite eruption, occurred approximately 39.000 years BP , while the earliest one, known as the Neapolitan Yellow Tuff eruption, happened 14.900 years BP (Troise et al., 2018).

Both the eruptions had massive consequences on the whole region, reshaping its geological features and creating pyroclastic deposits and stratifications which are well recognizable nowadays (for example, the second episode owes its name to the typical tuff which constitutes the main bedrock of the city of Naples and has been the most used building material in its historical architecture, as reported by Colella et al., 2017).

After the latter event, the area experienced three other periods of activity between 12.000 and 3800 years BP (Dvorak and Mastrolorenzo, 1991), followed by a period of quiescence which terminated in 1538 AD with the last magmatic eruption. This final episode gave rise to the scoria cone of Monte Nuovo, and it was likely triggered by the progressive transfer of magma from a deep source to a shallower one beneath the caldera center (Di Vito et al., 2016).

Both before and after this last episode, throughout ancient, classical, medieval and modern times, the whole caldera has experienced a long series of bradyseisms, undergoing several cycles of subsidence and uplift. Several locations along the coast of the Bay of Pozzuoli which were inhabited during the Roman period were gradually submerged during the Early Middle Ages, and a decade-long phase of inflation preceeded the Monte Nuovo eruption, totaling more than 17m of uplift (Di Vito et al., 2016).

These periods of unrest were accompanied by seismicity and increase in hydrothermal activities, and most of them are well documented in the historical chronicles. Good reconstructions of each phase of unrest can be found in papers such as Di Vito et al. (1999) or Di Vito et al. (2016).

One of the most remarkable evidence of these processes are the ruins of an ancient roman market, known as the "Serapeum", in the city of Pozzuoli (whose location can be seen in fig. 1.1). Its excavation, at the half of the 18th century, brought to the light the presence, on its three high standing columns, of holes of lithodomes [1],

---
[1]Lithodome is a genus of bivalve molluscs which are able to bore holes for shelter in limestone

a proof of an earlier marine submersion and evidence of sea level fluctuations in the area (among the first works on the subject, we can cite Babbage (1847)).

Following the last eruption, the caldera underwent a long period of subsidence until the first half of the 20th century. Then, a new phase of uplift began, reaching its peaks in two major bradyseisms in 1969-1972 and, above all, 1982-1984. A huge increase in seismic activity marked both the episodes, especially the latter one. At the end of 1984 the uplift trend stopped, and a subsidence phase with a much slower rate ensued, lasting until 2005, when a new period of inflation took over.

In the following we will give attention especially to the more recent episodes, from the 1982-84 bradyseism to the present day, and the next paragraph is devoted to a more detailed description of this last period.

Two recent episodes: the 1982-84 bradyseism and the 2005-still ongoing uplift

The overall trend of ground motion over the whole Campi Flegrei caldera during the last 1000 years has been dominated by subsidence, with an average rate of 1.7 cm/year (Troise et al., 2018). There have been, however, several phases of inflation. The last one started in the early 1950s, interrupting the long lasting subsidence which followed Monte Nuovo eruption. A first event between 1950 and 1952 totaled about 0.75 m of uplift, then culminating in the peak between 1969 and 1972, at the end of which a further 1.77 m uplift was recorded at the point of maximum deformation, located in Pozzuoli (Gaudio et al., 2010). This led to a first evacuation at Rione Terra, due to the consequences of ground deformation on buildings and infrastructures.

The new and most considerable phase of unrest started in 1982, with a marked increase of the ground deformation rate during the first half of 1983 (up to about 10 cm/month, D'Auria et al. (2014)). The deformation rate reached peaks of about 1 m/year, then it started decreasing during the second half of 1984, and it reverted to subsidence in January 1985. The total uplift measured in Pozzuoli from January 1982 to November 1984 was 1.80 m.

The vertical deformation revealed by leveling data showed a bell-shaped pattern centered around the area of Pozzuoli harbour, coinciding with the point of maximum deformation (as reported in fig. 1.2). The overall spatial pattern of uplift was nearly axi-symmetric, and it remained remarkably unchanged during the whole period (Bonafede and Ferrari, 2009).

One of the most relevant aspects of the 1982-84 unrest was the important increase in seismic activity, while the two previous episodes of uplift were accompanied by weak to moderate seismicity. Starting from the second half of 1982, there was a gradual increase in both the number and the magnitude of earthquakes (D'Auria et al., 2014), which became particularly marked at the beginning of 1983. The rate of seismicity remained almost stationary during 1984, although intense seismic swarms were recorded and widely felt by the population.

The total amount of seismic events for the 1982-84 unrest consists of about 16,000 recorded earthquakes, with magnitudes ranging from 0.5 to 4.2. The epicenters were mostly located between Pozzuoli and the ancient volcanic vent of Agnano (fig. 1.1),

---

or other kinds of rocks.
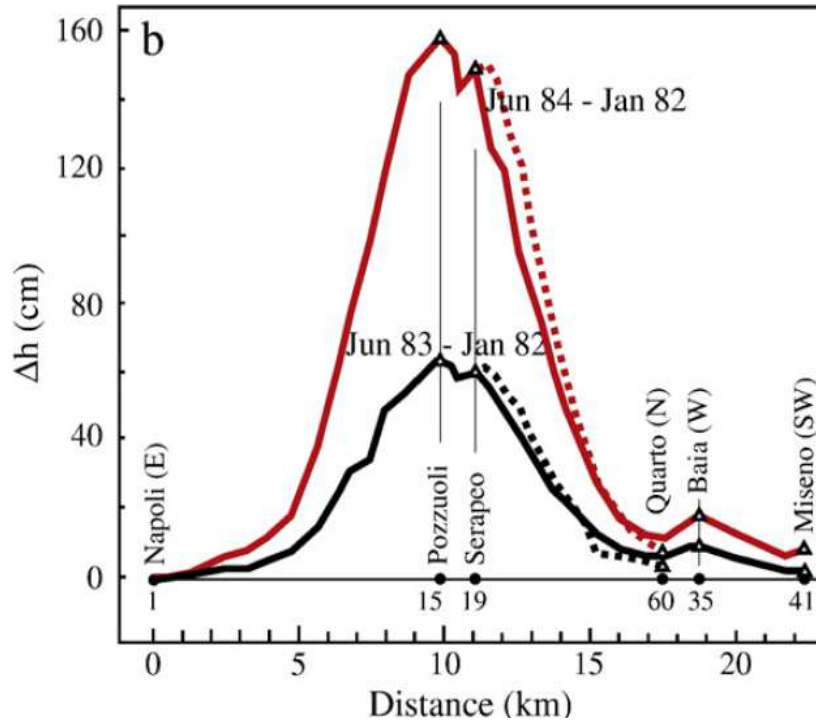
Figure 1.2: Spatial pattern of uplift measured on a baseline between Napoli and Pozzuoli (see the map in fig. 1.1) in June 1983 (black) and in June 1984 (red) with respect to January 1982; the approximate axial symmetry is shown by the dotted lines (Pozzuoli–Quarto): the maximum uplift was always found close to the center of Pozzuoli (after Trasatti et al., 2011).

with another cluster located in the Pozzuoli harbour; the hypocenters were generally above 5 km depth (D'Auria et al., 2014). The series of seismic swarms, together with fears for an imminent eruption in the area, prompted the partial evacuation of the town of Pozzuoli during the last two years of the crisis (Troise et al., 2018).

As we already mentioned, the uplift ceased by the beginning of 1985, and a twenty-year long phase of subsidence followed, lasting up to 2003 and leading to the partial recovery of the preceding ground displacement, although there has been a permanent ground uplift after the 1984 peak. The rate of subsidence was of about 4 cm/year on average, but it decreased progressively and it stopped around 2004. Complessively, about 80 cm of ground uplift were recovered.

The ensuing period, starting from 2005, has seen a new trend of ongoing uplift. Its rate, though far smaller than that of 1982-84, has gradually increased during the last years, showing an approximately exponential trend. In fact, a really striking aspect of this last phase is that there is a remarkable symmetry between its main uplift trend and the main subsidence trend of the previous period (Moretti et al., 2018).

Moreover, the shape of ground deformation has remained practically unaltered during both up and down movements, regardless of the differences in their amounts, and it has maintained the same features it showed during the 1982-84 episode (namely, the bell-shaped pattern around the area of Pozzuoli, Troise et al., 2018). These are key observations to take into account, as they could tell us something about the mechanisms these processes are driven by.
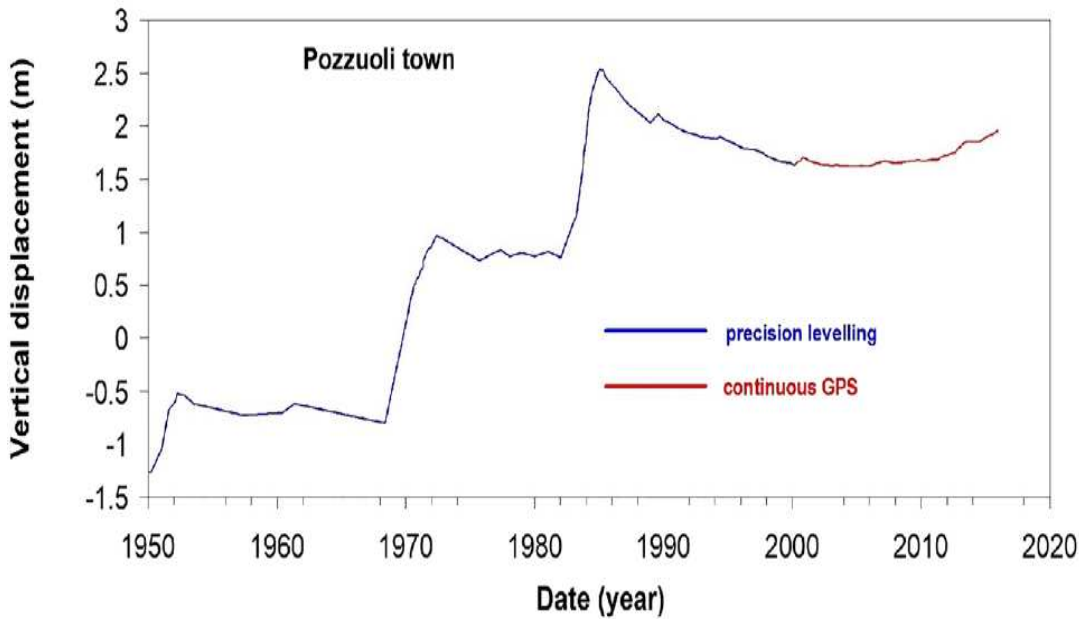
Figure 1.3: Chronogram of the maximum vertical ground displacement in the Campi Flegrei area. Sharp uplifts characterized unrest episodes occurred in 1950–52, 1969–72 and 1982–84. A 20 year-long subsidence took place at the end of the 1982–84 crisis. A new unrest phase started around year 2005, characterized by a lower uplift rate than during the previous uplift episodes (after Moretti et al., 2018).

Both the subsidence and the recent uplift phases were characterized by minor peaks of uplift superimposed on the global trend, which have always been followed by a fast recovery of their whole deformation. They are referred to as "mini-uplifts", among other authors, by Gaeta et al. (2003), and they seem to recur once every four years.

The most recent and noticeable of such episodes occurred between 2011 and 2013, and it was characterized by a temporary, sharp increase in the uplift rate, up to 16 cm/year: this likely affected the decision of the italian Civil Protection to raise the alert level for the area, even if the rate later decreased to the previous values. A further, minor uplift episode could also be recognized in 2016.

Interestingly, the seismicity seems to confirm an increasing trend in the last decade, though still far from the peak of the 1982-84 unrest.

A summary chronogram of the maximum vertical displacement measured in Pozzuoli during the last seven decades is reported in fig. 1.3.

A first valuable piece of information we can deduce from the analysis of the geological history of Campi Flegrei, even regarding very recent times, is that brady-seisms and, more generally, ground deformation and unrest episodes are not necessarily followed by magmatic eruptions within the caldera system: as a matter of fact, they hardly ever are.

A consideration like this compels us to reconsider the role played by ascending magmatic intrusions and hydrothermal processes in originating these unique phenomena.

Observing and measuring the ground motion at Campi Flegrei

The studies of ground motion at Campi Flegrei took the first step with the observations of the height of bands of molluscs bores on the columns of the Serapeum in Pozzuoli. These observations remained the only means of measuring the ground movement in the area until the very beginning of the 20th century, and even today they are especially valuable in reconstructing the changes in the coastline and the sea level, and thus the history of past cycles of inflation and deflation.

Precision levellings started to be carried out at Pozzuoli harbour in 1905, and continued throughout the century (Troise et al., 2018). They accounted for the monitoring of all the major uplift episodes from 1950 to 1984. The first vertical levellings in the 1970s, together with Electro-optical Distance Measuring and tide gauge records in the 1980s (Trasatti et al., 2011; Trasatti et al., 2015), allowed to reconstruct the deformation pattern all over the area during the 1982-84 bradyseism and the following phases.

In 2000, a permanent GPS station was installed at Rione Terra, a neighborhood of the town of Pozzuoli, and this has led to more precise and, most importantly, continuous set of geodetic data.

Finally, the last 20 years have seen the employ of space geodetic techniques, such as InSAR (Interferometric Synthetic Aperture Radar) surveys, which have provided a reliable set of data on the ongoing deformation trend and the "mini-uplift" episodes. For example, the last significant uplift event was monitored by the COSMO-SkyMed mission, whose space segment consists of four satellites equipped with SAR sensors, from February 2011 to December 2013 (Trasatti et al., 2015).

We briefly mention other crucial data sets. Seismic data have been provided by the network of seismic stations managed by the Osservatorio Vesuviano, with occasional contribution from foreign institutes and universities (D'Auria et al., 2014), while geochemical data have been collected with good continuity since 1982 (Troise et al., 2018), consisting of the analysis of chemical species in the fluids emitted from fumaroles, mainly located in the Solfatara crater.

Gravimetry surveys have also provided valuable insights on the geology of the caldera, and seismic tomography studies (Chiarabba and Moretti, 2006) have shed light on the elastic structure of the shallow crust (in particular, they have evidenced a high $\frac{v_p}{v_s}$ [2] anomaly in the caldera center at shallow depths, interpreted as the presence of a liquid aquifer, and another lower anomaly located between 2 and 4 km).

Finally, the stratigraphy of some parts of the caldera has been investigated through drillings, like the Campi Flegrei Deep Drilling Project (Natale et al., 2016), enabling researchers to gather information on the characteristics, temperature and parameters of rocks in the shallow crust, up to 3 km depth.

We conclude the section pointing out that, according to Zollo et al. (2008), the whole Neapolitan volcanic area is fed by a permanent, large molten body in the form of a wide (> 200 km^2) and thin (about 1 km) sill, located between 7 and 10 km depth. Besides, there are other authors advocating the presence of a shallow and smaller magmatic reservoir at a depth between 3 and 4 km beneath the caldera (e.g. Arienzo et al., 2010, Trasatti et al., 2011).

---

[2] v_p and v_s are, respectively, the velocities of compressional and shear waves in an elastic medium.

Any model employed for the area should also consider the interaction between these two reservoirs, especially when suggesting direct magma emplacement to explain ground deformation.

In addition to this, it is useful to include the dynamics of the caldera into the tectonic environment of the Campania margin, which is characterized by extensional structures and normal fault activity (Lima et al., 2009).

1.3 Modelling the unrest and its causes

The scientific literature of the last 60 years has provided a series of reliable source models to reproduce surface deformation in volcanic areas: these include pressurized cavities of various shapes, tensile cracks filled by pressurized fluids and inflating inclusions, all embedded in a medium which, be it layered or homogeneous, should take into account the known properties of the crust of the region they are to be applied to. In the case of Campi Flegrei, and more generally of calderas, a porous medium and the presence of fluids should be considered.

When considering the phenomena associated with caldera unrest, one of the most critical points is to discriminate between the effects directly attributable to shallow magma intrusions and those due to hydrothermal processes, which may involve interaction with magmatic bodies at depth anyway.

With respect to the 1982-84 unrest at Campi Flegrei, this has led to two main schools of thought in the course of the last decades: the first one sees the episode as a direct consequence of magma ascension and emplacement at a shallow depth, while the second one advocates the role of the geothermal system in accounting for the bradyseism. These two points of view have led to many interpretations in disagree with each other, eventually merging in some works stressing their interplay, and this has continued as well into the scientific literature on the more recent phase of inflation.

In the next subsection, we are going to review some of the source models that have been applied to Campi Flegrei to understand the causes of the 1982-84 and subsequent unrest episodes.

1.3.1 Deformation sources

The simplest source one can consider for the deformation of a volcanic region is a pressurized sphere embedded in a homogeneous and elastic half-space, assuming that the radius of the sphere is smaller than its depth. This is known as the Mogi source (Mogi, 1958), and it can represent an idealization of a magma chamber. A schematic representation of the model is available in fig. 1.4.

The model developed by K. Mogi provides an analytical solution to this problem, and it is characterized by only four parameters (namely, the coordinates of the center of the source (x_s, y_s, z_s) and the change of the hydrostatic pressure in the sphere ΔP). As it constitutes the simplest model available, it is still employed nowadays as a test model, when data are scarce, or when the ground displacement shows some axial symmetry.

When regarding the 1982-84 bell-shaped deformation pattern at Campi Flegrei (fig. 1.2), many authors have found that it can be nicely fitted by a Mogi source
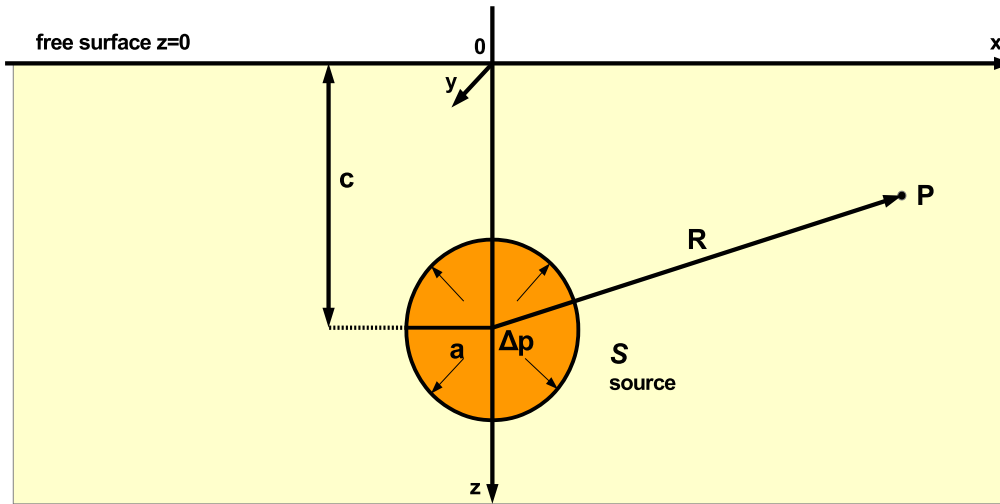
Figure 1.4: Schematic picture of a Mogi source (S) as a pressurized spherical cavity (shaded in orange) of radius a and at depth c with overpressure Δp, embedded in a homogeneous half-space (shaded in pale yellow). P is the point where the strain and stress fields are to be computed, while R is the distance between the point and the center of the source.

located at about 3 km depth beneth the center of the caldera (e.g. Berrino et al., 1984).

Other authors have generalized the Mogi model to a viscoelastic rheology (Bonafede et al., 1986), and even a viscoelastic shell model has been considered, in which viscoelastic properties are assigned only to a spherical shell surrounding a magma chamber. Moreover, the Mogi source is equivalent to an isotropic distribution of force dipoles (the so-called "center of dilation") or of tensile dislocations (Bonafede and Ferrari, 2009).

Another class of source models is represented by pressurized ellipsoidal cavities: these can assume a wide variety of shapes and orientations, depending on the length and disposition of the three axes. Davis (1986) provided solutions for the surface displacement field due to an arbitrarily oriented ellipsoidal cavity in an elastic half-space using Eshelby's elastic inclusion theory (Eshelby, 1957) and Mindlin's half-space point force solution (Mindlin, 1936) (these are the same theoretical premises we will adopt in the rest of this work).

With respect to Campi Flegrei, it has been shown by Battaglia et al. (2006) that a pressurized penny-shaped crack (which can be seen as a degenerate ellipsoid, with a vanishing minor axis) at 2.6 km depth, probably filled with magmatic fluids (supercritical water), is the most probable source of the 1982-84 unrest. Other authors (Amoruso et al., 2008) have proposed the same source model, supporting however the presence of magma at its interior, and also considering a layered embedding medium.

Among the other examples of source models we can refer to, there is the rectangular dislocation, whose analytical expression for the displacement and stress fields in an elastic half-space was developed by Okada (1992).

According to D'Auria et al. (2014), after inverting the 1982-84 ground deformation data set, the Okada rectangular crack is the best suited from a statistical point of view, allowing for the assumption of the presence of a sub-horizontal tensile dis-

location beneath the Pozzuoli area, possibly filled with fluids of magmatic nature.
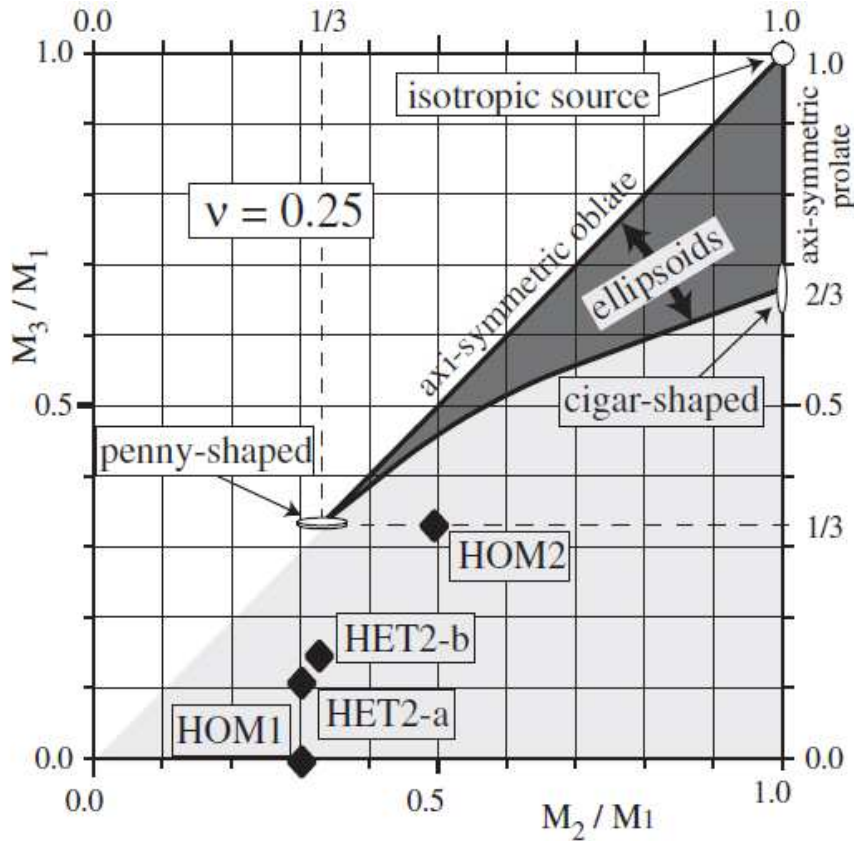
Figure 1.5: Ratios of eigenvalues M3/M1 and M2/M1 admissible for pressurized ellipsoids (dark gray subset) in the Poisson approximation ($\nu = 0.25$). By assumption, $M1 \geq M2 \geq M3$ (light gray area). The four solid diamonds stand for the source models for the 1982-84 unrest considered in the work which the figure is taken from, none of which falls into the ellipsoid area (after Trasatti et al., 2011).

One last consideration (Trasatti et al., 2011) arises from the fact that all these models assume a particular source mechanism and typically neglect the medium heterogeneities, thus biasing the estimation of source parameters.

Deformation sources can be described, more generally, in terms of a suitable moment tensor density distribution over a certain spatial extent (e.g. Aki and Richards, 2002). If the source dimension is small enough with respect to its depth, the surface displacement can be reproduced by adopting the point-source approximation, and so by retrieving a suitable moment tensor M_{ij} from the inversion of data. With regard to ellipsoidical source models (Davis, 1986) a pressurized ellipsoid can be described by a moment tensor, with the principal axes orientation being directly related to that of the principal stress axes. The three moment tensor eigenvalues

16

(M_i) are inversely proportional to the length of the ellipsoid axes ($a > b > c$).

It can be shown (Trasatti et al., 2011) that by plotting the ratios $\frac{M_2}{M_1}$ vs $\frac{M_3}{M_1}$ of the eigenvalues of the moment tensor, it is possible to identify which values correspond to ellipsoidal sources, and which not. If the retrieved values for (M_i) do not fit into the ellipsoid region of the plot, as it was the case of the 1982-84 ground deformation, then assuming an ellipsoidal source is no longer the best choice, and other kinds of models have to be taken into account. Following this approach, Trasatti et al. (2011) concluded that a mixed mode dislocation, both shear and tensile, through which a magma volume might have intruded, is the most suitable interpretation of their best fit moment tensor.

1.3.2   The debate on magmatic and hydrothermal origins for the 1982-1984 episode

As explained by Lima et al. (2009), models of bradyseisms can be explained assuming three scenarios, all of which ultimately depend on the presence of a magma body at depth, even if the role of magma in driving the phenomenon is different.

One scenario involves shallow magmatic intrusions of different shapes. This interpretation of both the 1982-84 and the 2011-13 unrest episodes has been suggested and shared by many authors, such as Dvorak and Berrino (1991) and Macedonio et al. (2014).

The recent sequence of up and down movements is interpreted as the effect of injections of magma at shallow depths, as part of a model in which sill-like magma intrusion at the discontinuity between two layers can generate uplift at surface, followed by subsidence when magma stops intruding and spreads laterally.

A two-reservoir model is also suggested, according to which the Campi Flegrei volcanic system could be fed by shallow magma accumulations between 3 and 4 km depth due to magma transfer from the deeper underlying source which feeds the whole volcanic region (Troise et al., 2018).

Purely magmatic models, however, find it difficult to explain the observed long lasting subsidence after the 1982-84 peak (Troise et al., 2018). Moreover, several seismic tomography surveys, like the reflection tomography Project Serapis (Judenherc and Zollo, 2004), have found no evidence of shallow magma batches in the 3-4 km depth range (while they have highlighted the large sill at about 8 km depth we mentioned in section 1.2). Even the temperature profiles inferred from deep drilling projects are generally incompatible with the presence of magma at shallow depths (Trasatti et al., 2011).

A second class of models also involve fresh magma input, but it views the bradyseism as due to the injection of magmatic fluids into the overlying crust, inducing fluid overpressure in the shallow hydrothermal system and the inflation of the host rocks. In this frame, subsidence could result from a decrease in the flux of magmatic fluids entering the system, or a rapid permeability increase (and pore pressure decrease) that occurs when the fluid pressure exceeds the local strength of the crust, leading to failures in the elastic matrix of the porous media.

The third scenario considers bradyseisms as the result of the complex interplay between processes operating on two very different timescales.

The longest one is associated with the cooling and crystallization of a magma volume at shallow depth, accompanied by generation of magmatic fluids, and it may be seen as the direct cause of a long-term trend of inflation. The minor and shorter uplift episodes are interpreted as the consequence of the episodic expulsion of fluids pressurized at the lithostatic pressure of their source region into an overlying hydrostatically pressured hydrothermal system.

A two-reservoir model like this has been proposed for Campi Flegrei by Lima et al. (2009): it contemplates the crystallization of a volatile-rich magma body at 6 km depth, and the subsequent release of magmatic fluids into a deep lithostatically-pressured aquifer. This one is separated from a more shallow hydrostatic aquifer by a low-permeability region at about 3 km depth.

Bradyseism episodes are seen as driven by the episodic and transient connection between these two systems, which is provided when the overpressure of the underlying fluids is enough to induce major breaches in the separating brittle and impermeable layer. This would also account for seismic swarms during unrest phases. If connectivity is established and fluids start migrating towards the shallow aquifer, then their volume tends to increase considerably as they move from a lithostatic-pressured region to a hydrostatic-pressured one. As a result, the temperature increase associated with volume increase will lead to a decrease in the solubility of silica in the fluids. Subsequent precipitation of silica in the porous matrix will lead to the self-sealing of the cracks and the pores, thus aiding in the reestablishment of isolated reservoirs.

The information provided by geochemical data is particularly crucial in discriminating magmatic from hydrothermal unrest mechanisms. In fact, the analysis of the ratios between concentrations of chemical species found in fumarolic gases, in particular $\frac{H_2O}{CO_2}$, can give insights of the presence of a magma intrusion at shallow depths. If that is the case, then the ratio increases because the water content in the gases exsolved from the ground would increase too, as magmatic steam is released in huge quantities into the hydrothermal system while the intrusion is cooling (Troise et al., 2018). Data collected in the 1982-84 period show indeed a sharp peak in water content, suggesting possible injections of magmatic fluids from a shallow source (Moretti et al., 2018), and even if there has been no evidence of similar trends during the more recent "mini-uplift" episodes, increases in the content of other species typically associated with magmatic fluids have been observed (Chiodini et al., 2015).

D'Auria et al. (2014), through a joint inversion of the focal mechanisms obtained from the 1982-84 seismic data series, were able to identify the principal stress axes orientation in the area: a subvertical σ_1 (that is, the minimum principal stress axis, whose direction corresponds to that of maximum compression) and a sub-horizontal σ_3 (which is the maximum principal stress axis, corresponding to the direction of maximum tension).

This would imply the presence of a prevailing extensional stress regime. According to the authors, this is mainly the reflection of the stationary background regional field, although the stress field within the region of unrest showed both spatial and temporal changes during the 1982-84 crisis, this being interpreted as linked to the intrusion of fluids, possibly of magmatic origin, within a shallow planar structure.

It is to say that focal mechanisms retrieved from the data show a very heterogeneous distribution among the different typologies (fig. 1.6).
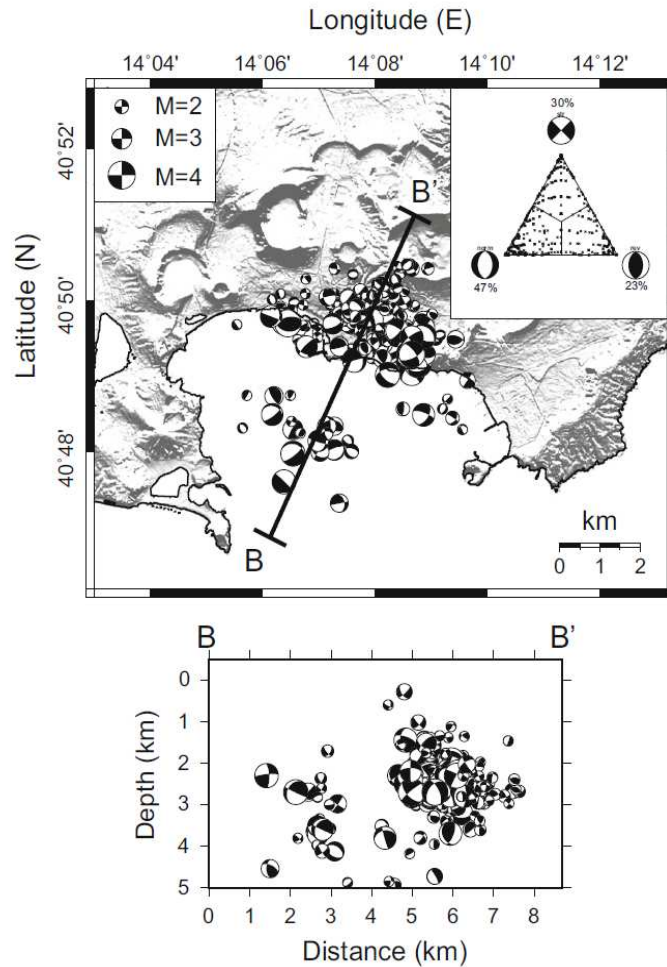
Figure 1.6: Focal mechanism data set relative to the 1982-84 unrest episode, represented both on a map of Campi Flegrei (top figure) and along the B-B' cross-section (bottom figure). The triangular diagram within the inset on the top right shows the distribution of observed focal mechanism types among normal, inverse and strike-slip, highlighting their heterogeneity (after D'Auria et al., 2014).

Recently a retrospective study (Troise et al., 2018) proposed that enough evidence had been provided to the hypothesis of a sill-like magma intrusion beneath the Pozzuoli area as the source of the 1982-1984 unrest. Its emplacement and the subsequent cooling and crystallization may have accounted for both the uplift and the following subsidence phase. The shallow magma sill may have solidified by 2000, and the prevailing gases injected afterwards, likely being the cause of the minor unrest episodes in recent years, may have originated from the deep magma reservoir into the hydrothermal system, possibly through the two-reservoir mechanism proposed by Lima et al. (2009).

The next and last section of this chapter will be devoted to the introduction of the source model that will be discussed and developed throughout the rest of our work, and which could also be applied to ground deformation observed in hydrothermal regions.

1.4 A first approach: the thermo-poro-elastic inclusion

If we aim to reproduce the ground deformation pattern accompanying an unrest episode in a hydrothermal region such as a caldera, then every kind of model, no matter how sofisticated it may be, should take into account at least the properties of the underlying medium.

In the case of Campi Flegrei, even if the stratigraphy shows a very complex structure, we can assume, to a first approximation, a homogeneous poro-elastic half-space. The latter assumption is necessary because, similarly to previous studies, we are interested in estimating the displacement field where it can be measured, that is at the Earth surface. Being free of traction, provided that the atmospheric pressure and winds are neglected, the Earth surface can be in fact approximated as the surface delimitating a half-space. Besides, as the majority of papers we have gone through agrees on the fact that the deformation source (be it a magmatic intrusion or a volume of overpressured magmatic fluids) responsible for the 1982-84 unrest is located between 2 and 5 km beneath the caldera center (Trasatti et al., 2011; Trasatti et al., 2015; Troise et al., 2018), our model should consider the presence of a free surface also because the source horizontal dimension, if estimated from the caldera dimension, is bigger than its depth, and therefore it is not possible to assume an infinite space.
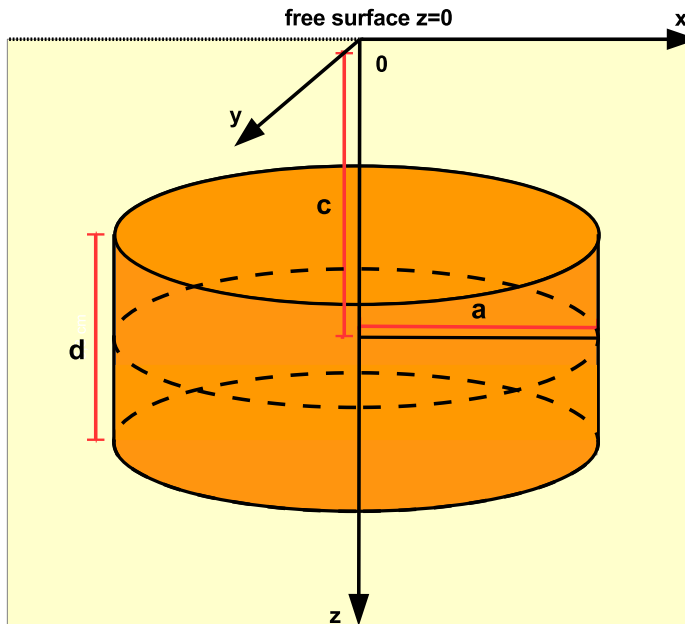
Figure 1.7: Schematic picture of a cylinder-shaped thermo-poro-elastic inclusion (highlighted in orange) with radius a and thickness d, located at depth c and embedded in a poro-elastic half-space (highlighted in pale yellow). The median plane of the cylinder is drawn for completeness, and ideally the thickness of the cylinder should be far smaller than its depth.

The source model we intend to discuss in our work consists of a cylinder-shaped thermo-poro-elastic inclusion embedded in a poro-elastic medium with a free surface (as it is shown in fig. 1.7). The inclusion undergoes a change in temperature and

pore pressure so that displacement and stress fields are induced both in its interior and within the surrounding half-space.

If we manage to provide solutions (by analytical or numerical methods) to this kind of problem, then we could evaluate the displacement at the free surface, enabling ourselves to confront these results with the field collected data.

The case of a cylinder-shaped thermo-poro-elastic inclusion in an infinite space has already been discussed by Lamberti (2017), and it can give valuable insights on the stress regime within the source region, provided that its depth is big enough to ignore the effects of the free surface.

Here we aim at providing solutions to the case in which the proximity of the free surface can no longer be neglected, as in the case of Campi Flegrei.

The approach we will be following is similar to that employed by Davis (1986): we will avail of the Eshelby method to retrieve the strain and stress fields within and outside the inclusion, and then we will provide the elastostatic Green's function for an half-space while accounting for the rheology of the media. In the end, both through analytical expressions and numerical techniques, we will evaluate these fields and focus on the displacement at the surface, comparing it to the results from other source models.

All of these steps will be carried out and developed in the course of the following chapters, the next one being devoted to the presentation of the theoretical procedure we will follow.

Chapter 2

Eshelby's method and its application to a thermo-poro-elastic inclusion in a half-space

In the first section of this chapter we give a brief introduction of the "Eshelby's method", which refers to the formal solution of a class of problems involving inclusions of arbitrary shape undergoing inelastic transformations in an elastic space. This method was first laid out by John D. Eshelby between the late Fifties and the early Sixties.

Then, in the following sections, we illustrate how to express the displacement field in an elastic medium by means of the Green's functions and how to generalize the procedure in the case of a thermo-poro-elastic source of deformation.

Eventually, a generalisation of the Green's tensor for the case of an elastic space bounded by a free surface is discussed and provided.

2.1 Eshelby's method for the elastic inclusion

In his first article on the subject (Eshelby, 1957), Eshelby focused on giving a solution to a certain cathegory of continuum-mechanics problems in which the uniformity of an elastic medium is perturbed by the presence of a region that either has changed its volume and shape, or has different elastic parameters with respect to the rest of the space.

Here we are interested in both these cases.

The first problem to be introduced is the following: a region, which will be referred to as the *inclusion*, bounded by a closed surface S in a homogeneous, elastic material, which will be named the *matrix*, undergoes a spontaneous change in volume and shape such that, were there no constraints imposed by the surrounding medium, it would result in an arbitrary homogeneous deformation e_{ij}^*, called the *stress-free strain*.

An approach like this can be used to describe several processes (Eshelby provided the example of a twin forming inside a crystal, among others). These include phase transformation, some plastic deformations and thermal expansion. We will be especially interested in the latter one.

Eshelby set the aim of evaluating the final strain and stress fields both within the region and the surrounding medium, with the help of a set of "*imaginary cutting, straining and welding operations*", to quote his own words. Before we are able to go through all of them, we must discuss the further assumptions he made:

- The inclusion and the matrix are joint together, and will remain so throughout all the course of the transformation. Thus, if we consider any pair of adjacent points immediately inside and outside the region-enclosing surface S, there is no relative displacement between them at the end of the process.

- Both the inclusion and the matrix are unstressed before the transformation, and they share the same elastic constants.

- In the original article, no assumptions were made on the spatial extension of the matrix in the first place, and the solutions hold in a generic case. However, in the following sections a further assumption will be made, which is that the matrix is bounded by a free surface. In any case, either if the space surrounding the inclusion is assumed to be infinite or bounded, we can solve for the displacement and stress fields in an analytical way.

The beginning of the problem thus sees the inclusion still joined to the outer medium, while the initial stress field is zero within both of them. The set of operations devised by Eshelby are the following, and they are also illustrated in fig. 2.1:

1. Make a cut along S and remove the inclusion from the matrix, leaving behind a cavity with the same volume and shape. At the end of the process, the inclusion will still be unstressed, as well as the matrix, and their original shape is preserved thanks to Kirchhof's uniqueness theorem.

2. Allow the inclusion to undergo its transformation of volume and shape under vanishing tractions on S, which results in the uniform stress-free strain e_{ij}^* (in that it occurs without changing the stress field, which remains zero).

3. In order to fit the inclusion back inside the cavity, bring it back to its original volume and shape through the application of surface tractions T_j on S. These can be expressed as $T_j = \tau_{ij}^* n_i$, where n_i is the $i-th$ component of the normal to the inclusion surface S, and $\tau_{ij}^* = -(\lambda e_{kk}^* \delta_{ij} + 2\mu e_{ij}^*)$ is the stress tensor derived from e_{ij}^*, resulting in a strain $-e_{ij}^*$. The $-$ sign in the expression for τ_{ij}^* is due to the fact that we need to remove the former strain e_{ij}^* in order to restore the original shape and volume of the inclusion.

4. Put the inclusion back into the cavity and weld the material together across S, being careful to maintain the applied surface tractions, which now become an infinitesimal layer of body forces spread all over S. At this stage, every point in the matrix and the inclusion is in the same position it was in the beginning (so the displacement field is still zero everywhere), and the matrix is still unchanged (namely, unstressed), whereas the stress inside the inclusion amounts to τ_{ij}^*.

5. The layer of body forces introduced before on each element dS of S is given by $dF_i = \tau_{ij}^* n_j dS$. To get rid of it, apply a further distribution $dF_i = -\tau_{ij}^* n_j dS$ over S. This is equivalent to letting the body forces which kept the inclusion in its former shape relax, and allowing the matrix to constrain the inclusion. This new, opposite layer of body forces leads to a non-zero displacement field within both the matrix and the inclusion u_i^c, the superscript c meaning "constrained".
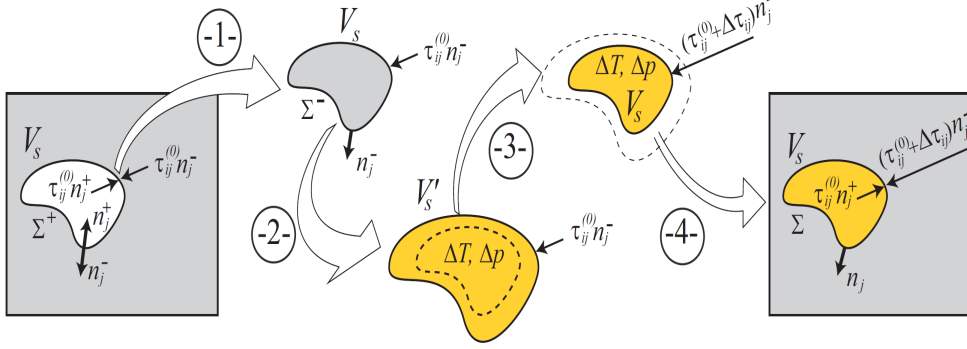
Figure 2.1: Graphical illustration of the conceptual steps devised by Eshelby (1957). The TPE region is yellow. The last two steps in the text are summarized in the fourth step in the picture (by courtesy of M. Bonafede).

In order to evaluate the displacement field u_i^c, Eshelby availed himself of the representation theorem, which provides general ways of calculating the displacement at a generic point in space in terms of the quantities that caused the motion (in particular, he resorted to the formulae reported by Love, 1927).

From u_i^c it is then possible to derive the related strain field for the whole space:

$$e_{ij}^c = \frac{1}{2}\left(\frac{\partial u_i^c}{\partial x_j} + \frac{\partial u_j^c}{\partial x_i}\right) \tag{2.1.1}$$

If the matrix is an homogeneous, isotropic elastic medium, then, according to the elastic constitutive relation $\tau_{ij} = \lambda e_{kk}\delta_{ij} + 2\mu e_{ij}$, the stress field within it is given as well by

$$\tau_{ij}^c = \lambda\frac{\partial u_k^c}{\partial x_k}\delta_{ij} + 2\mu e_{ij}^c \tag{2.1.2}$$

where λ and μ are the Lamé's constants, and ν is the Poisson's ratio.

The stress field inside the inclusion, however, differs from the latter, in that there already is the stress τ_{ij}^*. The "internal" stress field is thus given by

$$\tau_{ij}^{in} = \tau_{ij}^c + \tau_{ij}^* \tag{2.1.3}$$

At this stage, it is both necessary and instructive to understand how the displacement field u_i^c is derived, and to go through a brief presentation of the elastic Green's function.

2.2 The elastic Green's function and the displacement field

As discussed in many textbooks (such as Aki and Richards, 2002), one of the major aims of the theory of elasticity is the representation of the displacement field due to realistic sources in terms of the one produced by the simplest of sources, which is an unidirectional unit impulse, precisely localized in both space and time (i.e., a delta-function body force). When considering a static source, as it is the case, the displacement field is given by the elastic Green's function.

Generally speaking, for a body in static equilibrium, the stress τ_{ij} and the body force F_j acting on it must satisfy the following set of partial differential equations:

$$\frac{\partial \tau_{ij}}{\partial x_i} + F_j = 0 \quad \forall j \tag{2.2.1}$$

If the body in question obeys the elastic constitutive relation $\tau_{ij} = C_{ijkl}e_{kl}$, where C_{ijkl} are the general elastic coefficients and e_{kl} is the strain field, eq. 2.2.1 can be expressed in terms of the displacement field u_k:

$$C_{ijkl}\frac{\partial^2 u_k}{\partial x_l x_i} + F_j = 0 \quad \forall j \tag{2.2.2}$$

When the body force F_j is a unit point force in the $m-th$ direction (namely, $F_j(\mathbf{x}) = \delta(|\mathbf{x}-\mathbf{x}'|)\delta_{jm})$ centered at the point $\mathbf{x}'$, as stated before, the solution of eq. 2.2.2 at a point $\mathbf{x}$ is precisely the elastic Green's function $G_{km}(\mathbf{x},\mathbf{x}')$:

$$u_k = G_{km}(\mathbf{x},\mathbf{x}')F_m(\mathbf{x}') \tag{2.2.3}$$

In other words, $G_{km}(\mathbf{x},\mathbf{x}')$ yields the displacement in the $k-th$ direction at point $\mathbf{x}$ due to a point force in the $m-th$ direction at $\mathbf{x}'$.

When dealing with a distribution of body forces, the overall displacement field can be expressed as the integral of the right term in eq. 2.2.3 over the space where these forces are present.

Going back to the Eshelby's problem, the displacement field originated by the layer of body forces $dF_i = -\tau_{ij}^* n_j dS$ can be obtained through an integral over the infinitesimal volume $V(S)$ where these forces are present:

$$u_i = \int_{V(S)} G_{ij}(\mathbf{x},\mathbf{x}')dF_j(\mathbf{x}') = -\int_{S} G_{ik}(\mathbf{x},\mathbf{x}')\tau_{kj}^* n_j(\mathbf{x}')dS(\mathbf{x}') \tag{2.2.4}$$

If the Gauss' theorem is applied to the last term of 2.2.4, we obtain the following expression:

$$-\int_{S} G_{ik}(\mathbf{x},\mathbf{x}')\tau_{kj}^* n_j(\mathbf{x}')dS(\mathbf{x}') = -\int_{V_S} \frac{\partial G_{ik}}{\partial x_j'}(\mathbf{x},\mathbf{x}')\tau_{kj}^* dv(\mathbf{x}') - \int_{V_S} G_{ik}(\mathbf{x},\mathbf{x}')\frac{\partial \tau_{kj}^*}{\partial x_j'}dv(\mathbf{x}')$$

$$\tag{2.2.5}$$

where the last term on the right side of the equation is zero, as τ_{kj}^* is constant.

The surface integral can thus be converted into a volume integral over V_S, which is the volume of the inclusion (and it is not to be confused with the volume $V(S)$,

which coincides with the layer around the surface of the inclusion where the body forces dF_i are applied), through the infinitesimal volume element $dv(\mathbf{x}')$:

$$u_i = - \int_{V_S} \frac{\partial G_{ik}}{\partial x'_j}(\mathbf{x}, \mathbf{x}')\tau^*_{kj}dv(\mathbf{x}') \qquad (2.2.6)$$

After having laid out the general solution to Eshelby's problems, it is time to explain and deal with the specific case of a thermo-poro-elastic region within an homogeneous, isotropic and elastic half-space. The way the solution given in eq. 2.2.6 can be adjusted to this new case of study is the aim of section 2.4. However, before we can go through that, it is necessary to give some insight into what poro-elastic media are, and which constitutive relations they obey. This is what the next section is devoted to.

2.3   Poro-elastic media

In this section we introduce the poro-elasticity theory, in the form that was first set by Biot (1941). In this work, he addressed the issue of describing the response of soil to an applied load. It constitutes a useful framework by which the rheology of media such as those found in a region affected by hydrothermal phenomena (as a caldera may be) can be effectively addressed.

A poro-elastic material can be seen as a medium made of a solid skeletal portion, which is supposed to behave as an elastic material, called *matrix* or *frame*, and is interspersed with cavities, called *pores* or *voids*, filled with a fluid, be it gas or liquid.

The configuration of a poro-elastic material is defined by the following quantities:

- The *porosity* is defined as the volume of empty space per unit volume of the medium. A further distinction can be made between this kind of porosity, which is the *total porosity*, and the *effective porosity*, which is the volume of interconnected void space per unit volume of the medium. While the former takes into account every kind of pores, even those isolated and surrounded by impervious material, the latter is referred only to the pores which are able to transfer fluids from one to another.

- The *fluid content* v_i is defined as the volume of the $i-th$ species of fluid inside the pores per unit volume of the medium, and it is a dimensionless quantity. If the material is saturated with a single type of fluid (typically water), then v coincides with the porosity.

- The *pore pressure* p is the pressure of the fluid filling the voids, acting normally to the surface of the cavities. It can be assumed as uniform throughout the pore space of a volume element, provided that the fluid migration through the pore network is slow enough to make the pressure differences negligible.

- The *confining pressure* or *mean pressure* P_c comes into account when a stress field is applied to the porous medium; it corresponds to the isotropic part of the stress tensor, namely $P_c \dot{=} -\frac{1}{3}\tau_{kk}$, and it is not to be confused with the pore pressure p.

- The strain and stress tensors e_{ij} and τ_{ij} are defined in the same way as in the discussion of elastic materials. The former provides the change of distance between two infinitesimal volume elements centered around the points $\mathbf{x}$ and $\mathbf{x} + d\mathbf{x}$ according to the definition $ds^2 - ds_0^2 = 2e_{ij}dx_idx_j$, where ds and ds_0 are, respectively, the infinitesimal distance at the end and at the beginning of the deformation process, and e_{ij} is defined as in eq. 2.1.1. The latter is defined as the $j-th$ component of the surface force applied on the $i-th$ infinitesimal coordinate surface (i.e., a surface whose normal coincides with the $i-th$ axis of the reference system). The only difference to be taken into account is that the distances and the surface, though still infinitesimal with respect to the macroscopic scale of the problem, should be large enough to characterize volumes of material including a significant amount of cavities and solid matrix, so that e_{ij} and τ_{ij} are sensitive to the contribution of both the elastic skeletal portion and the fluid inside the pores.

A material can be addressed as poro-elastic if the deformations from a state of equilibrium to another are reversible. It should also satisfy the assumption of isotropy. Additional assumptions concern the flow of the fluids through the connected cavities, which should be described by Darcy's law (see the Appendix, section 6.1). Furthermore, the elastic matrix is supposed to obey the linear elastic constitutive relations for small strain.

To obtain the constitutive relations for a poro-elastic material, we may first consider a cubic-shaped element big enough so that its volume is large compared to the volume of any of its pores, and its dimensions are large with respect to the distances between one cavity and another; at the same time, it should be small enough compared to the length scales of the phenomena we are analyzing. The first assumption makes it possible to consider the element as homogeneous; the second one allows it to be taken as infinitesimal in our mathematical discussion.

If we allow the element to undergo a reversible deformation, then the macroscopic variables e_{ij}, τ_{ij}, v, p must be state functions, and this, in turns, means that we can express a set of them with respect to the others (for instance, in an isothermal transformation, we could write e_{ij} and v in terms of τ_{ij} and p). Moreover, if the strain and the variation of fluid content are small, then these relations can be expected to be linear.

Following these assumptions, let us consider our volume element at its initial state of equilibrium, before the transformation occurs, being described by $p_0, v_0, \tau_{ij}^0, e_{ij}^0$. Since no deformation has yet occurred, we can set $e_{ij}^0 = 0$. At the end of the process, we expect these quantities to have changed of amounts $\Delta p, \Delta v, \Delta \tau_{ij}$ and $\Delta e_{ij} = e_{ij}$, respectively. For the sake of a simpler notation, in the following of this section the first three amounts will be referred to as $p \doteq \Delta p$, $v \doteq \Delta v$ and $\tau_{ij} \doteq \Delta \tau_{ij}$.

Now we are going to analyze two different experimental setups: a deformation occurring with constant pore pressure, and another with constant stress.

Constant pore pressure deformation ($p = 0$)

In the first case, which is illustrated in fig. 2.2, the poro-elastic specimen has its surface open to the atmosphere: this means that the fluid filling the voids is free to flow out during the transformation up to the point where the pore pressure equals
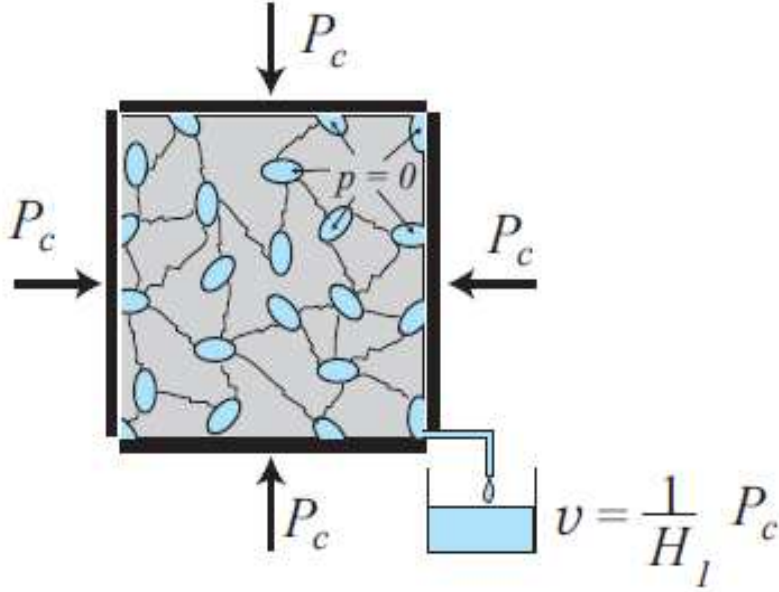
Figure 2.2: Compression of a volume element of poro-elastic material under constant pore pressure (drained conditions): the unit volume expels a quantity v of fluid which is proportional to the confining pressure P_c through the constant $\frac{1}{H_1}$. (By courtesy of M. Bonafede)

the atmospheric pressure, so that the final pore pressure is equal to the initial one, and $p = 0$. Such a transformation is what goes by the name of *drained test*, and in a case like this, the constitutive relation is the same as for a purely elastic material, as expressed in eq. 2.1.2. The strain tensor is given by

$$e_{ij} = \frac{1}{2\mu}\left(\tau_{ij} - \frac{\nu}{1+\nu}\tau_{kk}\delta_{ij}\right) \tag{2.3.1}$$

where μ and ν are respectively the drained modulus of rigidity and the drained Poisson's modulus, which can considerably differ from the moduli of a homogeneous elastic medium (or from those of the elastic matrix alone).

In this kind of transformation, the fluid content of the material must change in order to keep the pore pressure constant, so we can assume a linear relation between v and τ_{ij}:

$$v = a_{ij}\tau_{ij} \tag{2.3.2}$$

where a_{ij} must be an isotropic tensor of rank 2 in order for v to be a scalar, and so $a_{ij} = a\delta_{ij}$. If we define the quantity $H_1 = \frac{1}{3a}$, which has the same dimensions of a stress, we can write

$$v = \frac{1}{3H_1}\tau_{kk} = -\frac{1}{H_1}P_c \tag{2.3.3}$$

$\frac{1}{H_1}$ stands for the volume of fluid flowing out from a unit volume of material per unit confining pressure P_c applied to the surface of the medium while keeping the pore pressure constant.
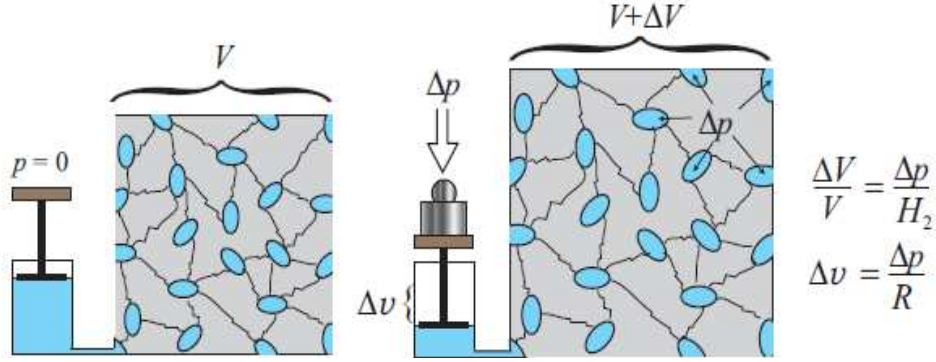
Figure 2.3: Strain of a volume element of poro-elastic material under constant stress deformation (free-expansion condition): the increase in volume of the material is proportional to the pore pressure change Δp through the constant $\frac{1}{H_2}$, and the volume of injected fluid Δv is proportional to Δp through the constant $\frac{1}{R}$. (By courtesy of M. Bonafede)

Constant stress deformation ($\tau_{ij} = 0$)

In the second case, as illustrated in fig. 2.3, there are no tractions applied to the surface of the poro-elastic volume element, so that it can undergo a stress-free expansion. Moreover, in order to control the fluid volume injected, the specimen itself is wrapped in an impermeable, albeit flexible, membrane, which is completely closed except for a tube through which fluid can be injected inside its pore network withouth applying any traction to its surface.

Since the material is free to expand, the injection of new fluid causes a change in the content of volume v and pore pressure p, without any additional stress, so $\tau_{ij} = 0$. Also in this case, we can expect the strain e_{ij} due to p to be described by a linear relation:

$$e_{ij} = b_{ij}p = \frac{1}{3H_2}p\delta_{ij} \qquad (2.3.4)$$

where b_{ij} must be an isotropic tensor of rank 2, too, and it can be written as $b_{ij} = \frac{1}{3H_2}\delta_{ij}$. The quantity H_2 we have introduced has the same dimensions of a stress, and $\frac{1}{H_2}$ represents the increase in the volume of the specimen per unit volume of the material for a unit increase in pore pressure.

The linear relation between v and p can be written as $v = \frac{1}{R}p$, where also R has the dimensions of a stress, and $\frac{1}{R}$ stands for the increase in the volume of fluid inside the pores per unit volume of the material, led by a unit increase in pore pressure.

General deformation of a poro-elastic material

If the specimen undergoes a deformation in which both the stress and the pore pressure change, then, thanks to the fact that e_{ij} is a state function, the process can be split into two distinct transformations: at first, the new stress is applied in drained conditions ($p = 0$), and subsequently the pore pressure is changed while keeping the

stress constant ($\tau_{ij} = 0$). This procedure leads to the following constitutive relations:

$$e_{ij} = \frac{1}{2\mu}\left(\tau_{ij} - \frac{\nu}{1+\nu}\tau_{kk}\delta_{ij}\right) + \frac{1}{3H_2}p\delta_{ij} \tag{2.3.5a}$$

$$v = \frac{1}{3H_1}\tau_{kk} + \frac{1}{R}p \tag{2.3.5b}$$

It can be noticed, according to eq. 2.3.5a, that the deviatoric strain tensor $e'_{ij} = e_{ij} - \frac{1}{3}e_{kk}\delta_{ij}$ is independent of changes in pore pressure, and it depends only on the deviatoric stress tensor, as it can be seen if we evaluate e_{kk} from 2.3.5a and substitute it in the definition of e'_{ij}:

$$e'_{ij} = \frac{1}{2\mu}\left(\tau_{ij} - \frac{1}{3}\tau_{kk}\delta_{ij}\right) = \frac{1}{2\mu}\tau'_{ij} \tag{2.3.6}$$

As a consequence, the modulus of rigidity μ does not depend on p. Even the bulk modulus K and the Poisson's modulus ν are defined in the same way as for an elastic medium, the difference being that the drained condition $p = 0$ must be verified. In particular, the drained bulk modulus is defined as the ratio of the infinitesimal mean pressure increase to the resulting relative decrease of the volume:

$$K = -V\left(\frac{\partial P_c}{\partial V}\right)_p = \frac{2\mu(1+\nu)}{3(1-2\nu)} \tag{2.3.7}$$

Finally, it can be proved, considering the expression of the strain energy per unit volume of the poro-elastic material, that $H_1 = H_2 \doteq H$. In view of this, eq. 2.3.5a and 2.3.5b can be rewritten as

$$e_{ij} = \frac{1}{2\mu}\left(\tau_{ij} - \frac{\nu}{1+\nu}\tau_{kk}\delta_{ij}\right) + \frac{1}{3H}p\delta_{ij} \tag{2.3.8a}$$

$$v = \frac{1}{3H}\tau_{kk} + \frac{1}{R}p \tag{2.3.8b}$$

2.4 Thermo-poro-elastic inclusion in a poro-elastic half-space

The approach and results of Eshelby's method can still be employed if the elastic inclusion of arbitrary shape is replaced by one which is made of a thermo-poro-elastic medium. This means that it will obey a different constitutive relation between stress and strain. The surrounding matrix is homogeneous, isotropic and poro-elastic too, even if drained conditions are assumed.

The first step is to evaluate the stress-free strain e^*_{ij} inside the inclusion once it has been removed from the matrix and allowed to undergo a change in temperature ΔT and pore pressure Δp.

It can be shown that the constitutive relation for e_{ij} we derived at the end of the previous section (eq. 2.3.8a) can be further generalized to the case of a thermo-poro-elastic medium undergoing changes in stress τ_{ij}, pore pressure Δp and temperature ΔT:

$$e_{ij} = \frac{1}{2\mu}\left(\tau_{ij} - \frac{\nu}{1+\nu}\tau_{kk}\delta_{ij}\right) + \frac{1}{3H}\Delta p\delta_{ij} + \frac{1}{3}\alpha\Delta T \tag{2.4.1}$$

where α is the coefficient of thermal expansion of the material.

Since the transformation undergone by the inclusion is stress-free, eq. 2.4.1 can be rewritten as follows:

$$e_{ij}^* = \frac{1}{3H}\Delta p \delta_{ij} + \frac{1}{3}\alpha \Delta T \delta_{ij} = e_0 \delta_{ij} \tag{2.4.2}$$

where

$$e_0 = \frac{1}{3H}\Delta p + \frac{1}{3}\alpha \Delta T \tag{2.4.3}$$

for a shorter notation.

If all the forces involved in Eshelby's method are applied in drained and isothermal conditions (that is, by keeping the pore pressure and the temperature unvaried both inside and outside the inclusion), then the thermo-poro-elastic medium behaves as if it were purely elastic, and so the assumption in section 2.1 which stated that the inclusion and the matrix were both elastic can still be made.

As stated in section 2.1, the stress field due to the restoration of the inclusion to its original shape, after the stress-free strain e_{ij}^* has taken place, is

$$\tau_{ij}^* = -(\lambda e_{kk}^* \delta_{ij} + 2\mu e_{ij}^*) \tag{2.4.4}$$

If the stress-free strain is such as in eq. 2.4.2, then τ_{ij}^* can be written as

$$\tau_{ij}^* = -(3\lambda + 2\mu)e_0 \delta_{ij} = -3Ke_0 \delta_{ij} \tag{2.4.5}$$

where $K = \lambda + \frac{2}{3}\mu$ is the drained isothermal bulk modulus in an isotropic medium, and λ and μ are still the Lamé's parameters, but in drained isothermal conditions.

When applying the body-force layer $dF_i = -\tau_{ij}^* n_j dS$ over the surface S of the inclusion, as in step 5 of the Eshelby's method (section 2.1), the displacement field for the whole space is given by eq. 2.2.6, which can be written as

$$u_i^c(\mathbf{x}) = 3Ke_0 \int\limits_S G_{ik}(\mathbf{x}, \mathbf{x}')n_k(\mathbf{x}')dS(\mathbf{x}') = 3Ke_0 \int\limits_{V_S} \frac{\partial G_{ik}}{\partial x_k'}(\mathbf{x}, \mathbf{x}')dv(\mathbf{x}') \tag{2.4.6}$$

Now, the next step would be to carry out the partial derivatives of the Green's tensor as they are in the right term of eq. 2.4.6. Here, however, a further problem arises.

If the matrix were an unbounded, homogeneous and isotropic elastic medium, then it could be proven that the Green's function G_{ik} would be the Somigliana's tensor, which depends only on the distance between the points $\mathbf{x}$ and $\mathbf{x}'$ and is given by

$$G_{ij}(|\mathbf{x} - \mathbf{x}'|) = \frac{1}{16\pi\mu(1-\nu)}\left[(3-4\nu)\frac{\delta_{ij}}{|\mathbf{x}-\mathbf{x}'|} + \frac{(x_i - x_i')(x_j - x_j')}{|\mathbf{x}-\mathbf{x}'|^3}\right] \tag{2.4.7}$$

where $|\mathbf{x} - \mathbf{x}'| = [(x_1 - x_1')^2 + (x_2 - x_2')^2 + (x_3 - x_3')^2]^{\frac{1}{2}}$.

Once the assumption of an infinite space is dropped, and the matrix is taken as a half-space (even though the other assumptions are left unchanged), the previous

formula for G_{ik} is no longer valid, and another expression for the Green's tensor is needed.

This is the purpose of the next and last section of this chapter, where the Mindlin's tensor, that is, the elastic Green's function for a half-space, is derived.

2.5 The Mindlin's tensor

In 1936, Raymond D. Mindlin devised a solution of the three-dimensional elasticity equations for a homogeneous, isotropic and elastic half-space when a concentrated force is acting in its interior (Mindlin, 1936). He took his premises from the Kelvin solution for the displacement and stress fields due to a point-force in an infinite solid, and the fact that it is possible to obtain the solution for any deformation source by superposing the solutions for a suitable distribution of point-forces.

Mindlin's strategy to address the issue was to consider separately two different cases, which are illustrated in fig. 2.4. In the first one, the point-force acts normally to the free surface, and is directed along the z-axis, whereas in the second one, the force acts parallel to the free surface itself (and its direction is taken along the x-axis). The reference system chosen for both these cases is a cartesian one, where the semi-infinite solid is bounded by the plane $z = 0$ and the z-axis is taken positive in the downward direction (i.e., it is penetrating into the body).
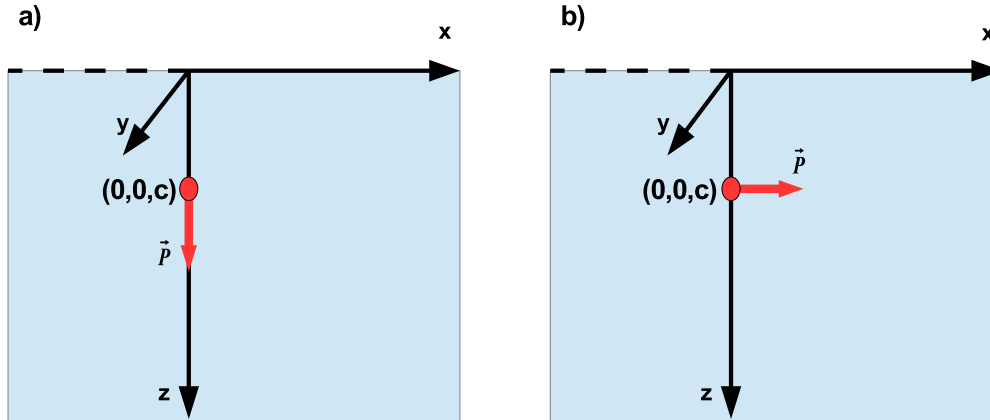
Figure 2.4: The two cases considered in Mindlin's article: a point-force applied in (0,0,+c) inside an elastic half-space normal (a) and parallel (b) to the bounding surface at z=0.

In both cases, the boundary conditions were set as follows:

- All components of the displacement and stress fields within the half-space must vanish at an infinite distance from the origin point of the reference system. This condition would be equally requested in the case of an infinite space.

- The traction acting on planes whose normal is in the $\hat{k}$ direction must vanish on the free surface defined by the plane $z = 0$ (free-surface condition). This in

turns leads to the conditions $\tau_{31} = \tau_{32} = \tau_{33} = 0$ at $z = 0$, and it is the main change to be dealt with when considering an half-space.

Mindlin expressed the displacement and stress components in terms of a Galerkin vector $\mathbf{F} = \hat{i}X + \hat{j}Y + \hat{k}Z$ and its components X, Y, Z. As far as our purpose is concerned, here we report only the expressions for the displacements:

$$u = \frac{1}{2\mu}\left[2(1-\nu)\nabla^2 X - \frac{\partial \boldsymbol{\nabla} \cdot \mathbf{F}}{\partial x}\right] \tag{2.5.1a}$$

$$v = \frac{1}{2\mu}\left[2(1-\nu)\nabla^2 Y - \frac{\partial \boldsymbol{\nabla} \cdot \mathbf{F}}{\partial y}\right] \tag{2.5.1b}$$

$$w = \frac{1}{2\mu}\left[2(1-\nu)\nabla^2 Z - \frac{\partial \boldsymbol{\nabla} \cdot \mathbf{F}}{\partial z}\right] \tag{2.5.1c}$$

where ∇^2 is Laplace's operator, μ is the modulus of rigidity and ν is the Poisson's ratio, as we will see in the next subsection. Therefore, the whole method comes down to the search of the required vector $\mathbf{F}$.

Here it is worth dwelling for a moment on what the Galerkin vector is and how it can be applied in such contexts.

2.5.1   The Galerkin vector

The Galerkin vector provides a widely used technique to remove non-vanishing tractions on the bounding surfaces of elastic half-spaces, in order for them to satisfy the free-surface condition. More generally, this technique makes it possible to get the stress and displacement fields in an elastostatic problem.

The starting point is to consider the representation of a generic displacement field in terms of a scalar and a vector potential, according to Helmholtz's theorem (which holds true for every vector field):

$$\mathbf{u} = \boldsymbol{\nabla}\phi' + \boldsymbol{\nabla} \times \boldsymbol{\Psi} \tag{2.5.2}$$

where the scalar potential ϕ' has a superscript to distinguish it from the coordinate ϕ in spherical and cylindrical bases that we will employ in the following of the work.

If this expression is substituted into the Cauchy-Navier equation, which is reported below

$$\rho_0 \frac{\partial^2 \mathbf{u}}{\partial t^2} = \mathbf{f} + (\lambda + \mu)\boldsymbol{\nabla}(\boldsymbol{\nabla} \cdot \mathbf{u}) + \mu\nabla^2\mathbf{u} \tag{2.5.3}$$

where ρ_0 is the density of the elastic medium, we obtain

$$\rho_0\left(\boldsymbol{\nabla}\frac{\partial^2 \phi'}{\partial t^2} + \boldsymbol{\nabla} \times \frac{\partial^2 \boldsymbol{\Psi}}{\partial t^2}\right) = \mathbf{f} + (\lambda + 2\mu)\boldsymbol{\nabla}(\nabla^2\phi') + \mu\boldsymbol{\nabla} \times (\nabla^2\boldsymbol{\Psi}) \tag{2.5.4}$$

If there are no body forces ($\mathbf{f} = \mathbf{0}$), then, in a static case (such that the term on the left side is identically zero), the last equation is satisfied for $\nabla^2\phi' = cost$ and $\nabla^2\boldsymbol{\Psi} = cost$, but this is not the most general solution, as the potentials ϕ' and $\boldsymbol{\Psi}$ are generally dependent from each other. Galerkin tried exactly to look for a

general solution of eq. 2.5.4, and he started from Helmholtz's representation of the displacement field, rewritten as:

$$2\mu u_i = \phi'_{,i} + e_{ijk}\Psi_{k,j} \tag{2.5.5}$$

where he assumed that the vector potential $\boldsymbol{\Psi}$ is in turn generated by a vector field $\tilde{F}_i$:

$$\Psi_k = -e_{klm}c\tilde{F}_{m,l} \tag{2.5.6}$$

where c is a constant to be determined. Substituting eq. 2.5.6 in eq. 2.5.5 and employing the identity $e_{ijk}e_{klm} = (\delta_{il}\delta_{jm} - \delta_{im}\delta_{jl})$, we obtain:

$$2\mu u_i = \phi'_{,i} + c\tilde{F}_{i,jj} - c\tilde{F}_{j,ji} = cF_{i,jj} - F_{j,ji} \tag{2.5.7}$$

where the last step is justified to the fact that $c\tilde{F}_{j,j}$ can be chosen as we please without changing the definition 2.5.6, and $F_i = \tilde{F}_i + H_i$, H_i being a suitable harmonic function ($H_{i,jj} = 0$). This representation of the displacement field can be used to simplify the static Cauchy-Navier equation $(\lambda + \mu)u_{j,jk} + \mu u_{k,jj} + f_k = 0$ through an appropriate choice of the constant c. If we substitute eq. 2.5.7 into the last equation, we obtain:

$$\left[\frac{c-1}{2(1-2\nu)} - \frac{1}{2}\right]F_{j,jiik} + \frac{c}{2}F_{k,jjii} + f_k = 0 \tag{2.5.8}$$

where $(1-2\nu) = \frac{\mu}{\lambda+\mu}$, and the first coefficient can be set to zero if $c = 2(1-\nu)$. Eq. 2.5.8 is satisfied if

$$2\mu u_i = 2(1-\nu)F_{i,jj} - F_{j,ji} \tag{2.5.9}$$

where

$$F_{k,jjii} = -\frac{f_k}{1-\nu} \tag{2.5.10}$$

The vector F_i we defined is precisely the Galerkin vector. If there are no body forces, it can be seen that F_i satisfies a biharmonic equation, that is 2.5.10. From eq. 2.5.9 it is possible to derive the expressions for the components of the displacement and stress field in terms of $F_1 = X, F_2 = Y, F_3 = Z$, as stated in eqs. 2.5.1.

The procedure followed by Mindlin to obtain the displacement and stress fields was to superpose the solution due to the single point-force in an infinite space (which he referred to as the "Kelvin's solution") and those due to a combination of five more sources, the so-called *nuclei of strain*. Notably, these could be reduced to an "image point-force" applied at $(0, 0, -c)$ and a suitable Galerkin vector: the effect of these two elements, neither of which introduce new singularities in the region occupied by the solid (namely, for $z \geq 0$), is to remove the non-vanishing boundary stresses τ_{3i} which would be given by the single-force solution on the free surface.

Let us now consider both the two cases analyzed by Mindlin, as they are illustrated in fig. 2.4.

Force normal to the boundary of a semi-infinite solid

In the first case (fig. 2.4 a), a force of intensity P is applied at point $(0, 0, +c)$ and acts in the positive z direction. Here Mindlin chose to switch to cylindrical coordinates (r, ϕ, z), as the problem will be symmetrical about the z-axis.

The Galerkin vector found by Mindlin, after converting the expressions reported in eqs. 2.5.1 to cylindrical coordinates, is given by:

$$\mathbf{F} = \left[\frac{P\hat{k}}{8\pi(1 - \nu)} \right] \left\{ R_1 + (3 - 4\nu)R_2 - 2c\frac{(z + c)}{R_2} - 4(1 - 2\nu)c\ln\left(R_2 + z + c\right) \right.$$
$$\left. + 4(1 - \nu)(1 - 2\nu)\left[(z + c)\ln\left(R_2 + z + c\right) - R_2\right] + \frac{2c^2}{R_2} \right\}$$
$$(2.5.11)$$

where

$$R_1 = \sqrt{r^2 + (z - c)^2} \tag{2.5.12}$$

is the distance between the observation point (r, ϕ, z) and the point where the force is applied, and

$$R_2 = \sqrt{r^2 + (z + c)^2} \tag{2.5.13}$$

is the distance between the observation point and the point where the image force is applied.

The only non-vanishing component of $\mathbf{F}$ is the $k - th$, as we would have expected from the symmetry of the problem.

The components of the displacement field, derived from eqs. 2.5.1 in cylindrical coordinates, are thus the following:

$$U = \frac{Pr}{16\pi\mu(1 - \nu)} \left[\frac{(z - c)}{R_1^3} + \frac{(3 - 4\nu)(z - c)}{R_2^3} - \frac{4(1 - \nu)(1 - 2\nu)}{R_2(R_2 + z + c)} + \frac{6cz(z + c)}{R_2^5} \right]$$

$$(2.5.14a)$$

$$w = \frac{P}{16\pi\mu(1 - \nu)} \left[\frac{(3 - 4\nu)}{R_1} + \frac{8(1 - \nu)^2 - (3 - 4\nu)}{R_2} + \frac{(z - c)^2}{R_1^3} \right.$$
$$\left. + \frac{(3 - 4\nu)(z + c)^2 - 2cz}{R_2^3} + \frac{6cz(z + c)^2}{R_2^5} \right]$$
$$(2.5.14b)$$

We now recall the aim we set at the beginning of this section: to find each and every component of the Green's tensor for an half-space G_{ij}, which we will refer to as the Mindlin's tensor. This would enable us to write the components of the displacement field in the same way as in eq. 2.2.3. In this case we are provided with the vertical component w, which we should be able to write as

$$w = u_3 = G_{3k}P_k \tag{2.5.15}$$

where $\mathbf{P}$ is the point-force that causes the displacement itself. However, the point-force we have considered so far has only one non-vanishing component, $P_3 = P$, so

we can obtain a first component of the tensor, namely G_{33}, straight from eq. 2.5.14b, after transforming its dependency from (r, ϕ, z) into dependency from (x_1, x_2, x_3). In the following, we will be employing the notation $x_i, i = 1, 2, 3$ to refer to cartesian coordinates, instead of (x, y, z), according to the index notation chosen to represent the displacement and stress fields.

Let us now focus on eq. 2.5.14a, or the radial component of the displacement field. This is given by $U = u_r = G_{rk}P_k = G_{rz}P_z$, so we could derive the G_{rz} component as well, although we are interested in the cartesian components. Recalling the transformation of a 2-nd rank tensor from cylindrical to cartesian coordinates, we may derive G_{23} through the following expression:

$$G_{23}(x_1, x_2, x_3) = G_{rz}(x_1, x_2, x_3)cos(\phi) - G_{\phi z}(x_1, x_2, x_3)sin(\phi) = G_{rz}(x_1, x_2, x_3)$$
(2.5.16)

where the last step arises from $\phi = 0$, if we choose the r-axis to coincide with the x-axis (and we are allowed to do so, thanks to the cylindrical symmetry of the problem).

Force parallel to the boundary of a semi-infinite solid

Now we turn our attention to the second case analyzed by Mindlin: that of a point-force parallel to the free surface and acting along the x-axis, always applied at a point $(0, 0, +c)$ (fig. 2.4 b).

Following the same approach we laid out earlier, the difference being there is no axial symmetry this time, and cartesian coordinates were employed as a consequence, he derived the Galerkin vector $\mathbf{F}$:

$$\mathbf{F} = \left[\frac{P}{8\pi(1-\nu)} \right] \left(\hat{i} \left\{ R_1 + R_2 - \frac{2c^2}{R_2} + 4(1-\nu)(1-2\nu) \left[(x_3+c) \ln(R_2+x_3+c) - R_2 \right] \right\} \right.$$
$$\left. + \hat{k} \left[\frac{2cx_1}{R_2} + 2(1-2\nu)x_1 \ln(R_2+x_3+c) \right] \right)$$
(2.5.17)

Here it is worth noticing that $\mathbf{F}$ has two non-vanishing components, namely F_1 and F_3.

The three components of the displacement field are derived accordingly, following eqs. 2.5.1:

$$u = \frac{P}{16\pi\mu(1-\nu)} \left[\frac{(3-4\nu)}{R_1} + \frac{1}{R_2} + \frac{x_1^2}{R_1^3} + \frac{(3-4\nu)x_1^2}{R_2^3} + \frac{2cx_3}{R_2^3} \left(1 - \frac{3x_1^2}{R_2^2} \right) \right.$$
$$\left. + \frac{4(1-\nu)(1-2\nu)}{(R_2+x_3+c)} \left(1 - \frac{x_1^2}{R_2(R_2+x_3+c)} \right) \right]$$
(2.5.18a)

$$v = \frac{Px_1x_2}{16\pi\mu(1-\nu)} \left[\frac{1}{R_1^3} + \frac{(3-4\nu)}{R_2^3} - \frac{6cx_3}{R_2^5} - \frac{4(1-\nu)(1-2\nu)}{R_2(R_2+x_3+c)^2} \right]$$
(2.5.18b)

$$w = \frac{Px_1}{16\pi\mu(1-\nu)} \left[\frac{x_3-c}{R_1^3} + \frac{(3-4\nu)(x_3-c)}{R_2^3} - \frac{6cx_3(x_3+c)}{R_2^5} - \frac{4(1-\nu)(1-2\nu)}{R_2(R_2+x_3+c)} \right]$$
(2.5.18c)

From these components we may derive straightly the following components of Mindlin's tensor: $G_{11} = \frac{u}{P}$, $G_{21} = \frac{v}{P}$, $G_{31} = \frac{w}{P}$.

At this point we are left with four more components that still need to be derived. In order to achieve this, we can resort to one useful class of theorems, known as the "reciprocity theorems", as it is stated in Aki and Richards (2002). These theorems provide a series of general relationships between a pair of solutions for the displacement through an elastic body. If these solutions are written in terms of Green's functions, as it is the case in eq. 2.2.3, and the problem satisfies homogeneous boundary conditions on the surface S of the body (i.e., either the displacement or the traction vanishes at every point of the surface), then an interesting property of G_{ij} arises:

$$G_{ij}(\mathbf{x}, \mathbf{x}') = G_{ji}(\mathbf{x}, \mathbf{x}') \tag{2.5.19}$$

which gives a spatial reciprocity between two components of the tensor, once the dependencies from the coordinates of the source point x_i' and those of the observation point x_i are swapped.

In our case, the problem we are considering does indeed satisfy homogeneous boundary conditions on the free surface, in that the vertical component of the traction must vanish everywhere on it. Therefore, we may employ eq. 2.5.19 to derive the components G_{12}, G_{13}, G_{32} directly from those already found, by simply swapping the dependencies from the source and receiver points.

Finally, the component G_{22} can be found in a slightly more complicated way. First, we consider again the second case of Mindlin's article (see fig. 2.4 b)), the one where the point-force is acting parallel to the free surface, only this time it acts in the positive y direction: $\mathbf{P} = \hat{j}P$. Then, the components of the displacement field are the same as in eqs. 2.5.18, provided that the dependencies from x_1 and x_2 are exchanged, and u and v switch places. This way, we are able to identify the last needed component from $v = u_2 = G_{22}P_2 = G_{22}P$.

The last step we need is to write the components of the tensor for the general case of a force applied at an arbitrary point (x_1', x_2', x_3') inside the half-space. The formulae for R_1 and R_2 are changed from the way they are defined in 2.5.12 and 2.5.13 into:

$$R_1 = \sqrt{(x_1 - x_1')^2 + (x_2 - x_2')^2 + (x_3 - x_3')^2} \tag{2.5.20a}$$

$$R_2 = \sqrt{(x_1 - x_1')^2 + (x_2 - x_2')^2 + (x_3 + x_3')^2} \tag{2.5.20b}$$

The nine components of the Mindlin's tensor are reported in the Appendix (section 6.2).

Chapter 3

Cylinder-shaped source in a half-space: resolution and results

This chapter is devoted to the explanation of the method employed to derive the displacement and stress fields due to the deformation source previously introduced, that is, the cylinder-shaped thermo-poro-elastic region embedded in a homogeneous poro-elastic half-space, following the technique laid out in chapter 2.

Particular emphasis will be given to the evaluation of the sum of partial derivatives of the Mindlin's tensor as reported in eq. 2.4.6, the separation of the problem into a singular and a non-singular part, and the way the relative integrals can be carried out.

Eventually, the results for displacements and stresses will be shown and interpreted both for the median plane of the source region and the free surface, and they will be compared to those obtained for the same case through a completely numerical approach.

3.1 The cylinder-shaped thermo-poro-elastic region

In the previous chapter we showed how it is possible, according to the Eshelby's method, to solve for the displacement and stress fields inside an elastic medium when a deformation source of arbitrary volume and shape is present inside of it.

Furthermore, we also went through the procedure Mindlin employed to evaluate the same fields when a single point-force is applied inside an elastic body bounded by a free surface, and this, in principle, would allow us to solve the same problem for whatever deformation source we choose, as it can always be expressed through an adequate distribution of point-forces.

These two powerful techniques enable us to tackle the original case we set the aim to analyze: that of a cylinder-shaped thermo-poro-elastic region (which from now on will be referred to as the "*TPE source region*") embedded in a homogeneous poro-elastic half-space, as illustrated in fig. 3.1, which undergoes a sudden increase of temperature ΔT and pore pressure Δp.

Before we start discussing the resolution of the problem, here we set once and for all the values of the parameters we will employ throughout the rest of the work. The shape of the TPE inclusion will be that of a cylinder of radius $a = 500$ meters
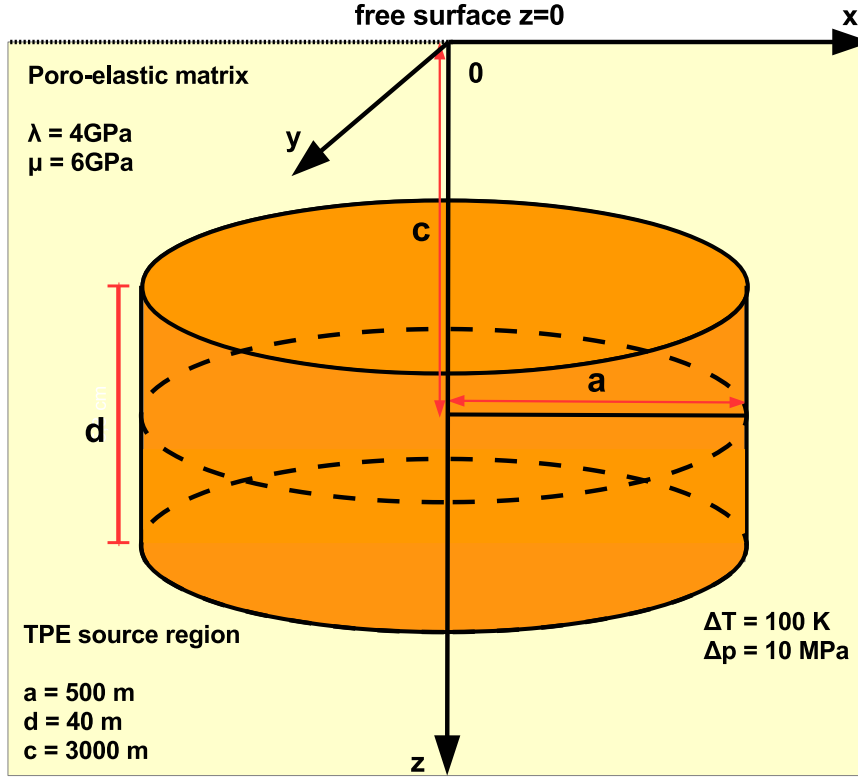
Figure 3.1: Cylinder-shaped thermo-poro-elastic inclusion (highlighted in orange) embedded in an elastic half-space (highlighted in pale yellow). The values of the elastic parameters of the matrix are shown, together with the geometric parameters of the cylinder and the changes in temperature and pore pressure within the deformation source. It is to say that the axis x, y, z will be referred to as, respectively, x_1, x_2, x_3 throughout the rest of the work.

and height $d = 40$ meters, with an aspect ratio of $\frac{d}{a} = 0.08$ (the importance of this parameter will be clear in the following of the work). The inclusion will be located at depth $c = 3000$ m beneath the free surface. The depth and the dimensions of the source region have been chosen in order to emphasize the effects of the free surface, which is the main focus of this work.

The elastic parameters in isothermal and drained conditions of the poro-elastic matrix will be $\lambda = 4$ GPa, $\mu = 6$ GPa and $\nu = \frac{\lambda}{2(\lambda+\mu)} = 0.2$. The changes in temperature and pore pressure within the inclusion will have the following respective values: $\Delta T = 100K$, $\Delta p = 10$ MPa. Finally, the thermal expansion coefficient of the TPE inclusion will be $\alpha = 3 \cdot 10^{-5}K^{-1}$, while $H = 10$ GPa (see section 2.3). These values are pertinent to highly porous sedimentary rocks (such as, for example, those constituting much of the stratigraphy of the Campi Flegrei caldera).

The first step is to recall that the effects of the changes in the TPE region on the surrounding medium can be interpreted as those caused by a traction discontinuity $-3Ke_0n_k$ acting on the surface elements $dS(\mathbf{x}')$ of the bounding surface of the inclusion. This brings us, following the same reasoning of section 2.4, to eq. 2.4.6, which is here reported for ease of reference:

$$u_i^c(\mathbf{x}) = 3Ke_0 \int_S G_{ik}(x, x')n_k(\mathbf{x}')dS(\mathbf{x}') = 3Ke_0 \int_{V_S} \frac{\partial G_{ik}}{\partial x_k'}(\mathbf{x}, \mathbf{x}')dv(\mathbf{x}')$$

where, as previously stated, $\mathbf{x}'$ gives the position of the source point, and $\mathbf{x}$ is the receiver point where we actually measure the fields.

The last term on the right is what we will be focusing on in the next section.

3.2 Sum of the Green's tensor partial derivatives

In eq. 2.4.6 we managed to express the components of the displacement field u_i^c on the basis of a triple integral on the volume of the TPE region of the sum of partial derivatives of the Green's tensor with respect to the coordinates of the source point x_k'. In particular, $\frac{\partial G_{ik}}{\partial x_k'}$ may be understood as the i-th component of the displacement field at the receiver point $\mathbf{x}$ produced by three orthogonal force dipoles with unit moment centered at the source point $\mathbf{x}'$.

If we were dealing with an unbounded elastic space, then we could employ the Kelvin-Somigliana tensor for G_{ik}, whose expression is given in eq. 2.4.7.

In that case, the sum of its partial derivatives could be carried out relatively easily, and rewritten as the gradient, with respect to the coordinates of the receiver point, of a scalar potential Φ. This, in turns, would allow for an analytical solution of the volume integral itself, and thus the displacement.

This point is worth stressing, as we will resort to this technique at least for a part of our calculations. However, as we will find out, that alone won't be enough to provide a solution to the problem as a whole.

3.2.1 The unlimited space case: the scalar potential

The case of a cylinder-shaped TPE region was considered by Lamberti (2017) for an unbounded homogeneous poro-elastic space, following the same hypothesis mentioned in the previous paragraph.

Starting as always from eq. 2.4.6 and eq. 2.4.7, the sum of partial derivatives of Somigliana tensor can be written as follows:

$$
\begin{aligned}
\frac{\partial G_{ik}}{\partial x_k'}(\mathbf{x}, \mathbf{x}') &= \frac{(1 - 2\nu)}{8\pi\mu(1 - \nu)} \frac{(x_i - x_i')}{R^3} = \frac{1 - 2\nu}{8\pi\mu(1 - \nu)} \frac{\partial}{\partial x_i'} \left(\frac{1}{R} \right) \\
&= -\frac{1 - 2\nu}{8\pi\mu(1 - \nu)} \frac{\partial}{\partial x_i} \left(\frac{1}{R} \right)
\end{aligned}
\tag{3.2.1}
$$

where

$$
R = \sqrt{(x_1 - x_1')^2 + (x_2 - x_2')^2 + (x_3 - x_3')^2}
\tag{3.2.2}
$$

and the last step is due to the fact that the derivative with respect to x_i' can be taken with respect to x_i with a simple change of sign.

Substituting the result of eq. 3.2.1 into eq. 2.4.6, and rewriting the bulk modulus as $K = \frac{2\mu(1+\nu)}{3(1-2\nu)}$, the displacement vector $\mathbf{u^c}$ can be expressed as

$$
\mathbf{u^c}(\mathbf{x}) = -e_0 \frac{1 + \nu}{4\pi(1 - \nu)} \nabla \int_{V_S} \frac{1}{|\mathbf{x} - \mathbf{x}'|} dv(\mathbf{x}') = -e_0 \frac{1 + \nu}{4\pi(1 - \nu)} \nabla \Phi(\mathbf{x})
\tag{3.2.3}
$$

where Φ is the Lamé's scalar potential, defined as

$$\Phi(\mathbf{x}) = \int\limits_{V_S} \frac{1}{|\mathbf{x} - \mathbf{x}'|} dv(\mathbf{x}') \tag{3.2.4}$$

A first piece of information on $\mathbf{u^c}$ is that it is an irrotational field, having been expressed as the gradient of a scalar potential.

Furthermore, we can notice that the potential in eq. 3.2.4 is formally equivalent to the Coulomb electrostatic potential due to a volume V_S of charge density $4\pi\epsilon_0$ (see Jackson, 1999), and therefore it satisfies the Poisson's equation inside V_S and the Laplace equation outside:

$$\nabla^2 \Phi^{in} = -4\pi \tag{3.2.5a}$$

$$\nabla^2 \Phi^{out} = 0 \tag{3.2.5b}$$

where the notation Φ^{in} and Φ^{out} refers to the potential being evaluated at a point, respectively, inside or outside the volume V_S of the TPE inclusion.

Another property of the potential Φ is that it is everywhere continuous together with its first derivatives, albeit its second derivatives suffer the following discontinuity across the surface S of the inclusion:

$$\left[\frac{\partial^2 \Phi^{out}}{\partial x_i \partial x_j} - \frac{\partial^2 \Phi^{in}}{\partial x_i \partial x_j} \right]_S = 4\pi n_i n_j \tag{3.2.6}$$

where n_i is the outward normal vector to the surface S.

Going back to the expression for the displacement $\mathbf{u}^c$ (eq. 3.2.3), we can carry out its divergence:

$$\boldsymbol{\nabla} \cdot \mathbf{u}^c = e_{kk}^c = -e_0 \frac{1+\nu}{4\pi(1-\nu)} \nabla^2 \Phi(\mathbf{x}) \tag{3.2.7}$$

which, after substituting the expressions for $\nabla^2 \Phi$ reported in eqs. 3.2.5a and 3.2.5b, enables us to find the relative volume change inside and outside the inclusion:

$$e_{kk}^c = \begin{cases} e_0 \frac{1+\nu}{(1-\nu)} = e_1 & \text{inside the inclusion} \\ 0 & \text{outside} \end{cases} \tag{3.2.8}$$

For the sake of notation, we will refer to the constant $e_0 \frac{1+\nu}{4\pi(1-\nu)}$ as e_1 in the following.

Then, if we make use of eqs. 3.2.8 and 3.2.3 in eq. 2.1.2, we can retrieve the expression for the stress tensor in the medium outside the inclusion:

$$\tau_{ij}^{out} = \tau_{ij}^c = -e_1 \frac{\mu}{2\pi} \frac{\partial^2 \Phi^{out}}{\partial x_i \partial x_j} \tag{3.2.9}$$

In the same way, we can find the expression for the stress tensor inside the inclusion by also taking into account eq. 2.1.3:

$$\tau_{ij}^{in} = \lambda e_1 \delta_{ij} - 2\mu \frac{e_1}{4\pi} \frac{\partial^2 \Phi^{in}}{\partial x_i \partial x_j} - 3K e_0 \delta_{ij} \tag{3.2.10}$$

where the last term on the right $-3K e_0 \delta_{ij}$ is the stress field τ_{ij}^* induced inside the inclusion by its restoration to its original shape and volume, according to the Eshelby's method (section 2).

It can be shown that both the displacement field and the tractions derived for this case are continuous across the inclusion surface S.

This procedure holds true for inclusions of arbitrary volume and shape, provided that a suitable expression for the scalar potential Φ is found. If we consider the case of a cylindrical source, all we have to do is find the corresponding potential.

Here we report the expressions for the components of the displacement field and the strain tensor obtained by Lamberti (2017), as they will be necessary for the purposes of the next sections. The details on how these expressions were found, starting with the retrieval of the scalar potential Φ in terms of Legendre polynomials ($P_l(x)$) series, are reported in the Appendix (section 6.3).

The displacement components are given by

$$u_r(r,\theta) = Aa\left[|\cos\theta| + \sum_{m=1}^{\infty} c_{2m}P_{2m}(\cos\theta)\frac{2m}{2m-1}\left(\frac{r}{a}\right)^{2m-1}\right] \tag{3.2.11a}$$

$$u_\theta(r,\theta) = -Aa\left[\text{sgn}(\cos\theta)\sin\theta - \sum_{m=1}^{\infty} c_{2m}\frac{dP_{2m}}{d\theta}(\cos\theta)\frac{1}{2m-1}\left(\frac{r}{a}\right)^{2m-1}\right] \tag{3.2.11b}$$

in the internal domain, and

$$u_r(r,\theta) = Aa\sum_{m=0}^{\infty} c_{2m}P_{2m}(\cos\theta)\frac{2m+1}{2m+2}\left(\frac{a}{r}\right)^{2m+2} \tag{3.2.12a}$$

$$u_\theta(r,\theta) = -Aa\sum_{m=1}^{\infty} c_{2m}\frac{dP_{2m}}{d\theta}(\cos\theta)\frac{1}{2m+2}\left(\frac{a}{r}\right)^{2m+2} \tag{3.2.12b}$$

in the external domain, where

$$A = e_1\frac{db}{2a} \tag{3.2.13}$$

The *internal* domain does not correspond tho the region inside the inclusion, but instead it represents a sphere of radius a with the same center of the cylinder. The *external* domain is defined as the outer region. Their definition is further discussed in the Appendix (section 6.3), and they are represented in fig. 6.2.

Finally, the strain tensor components are the following:

$$e_{rr} = A \sum_{m=1}^{\infty} 2m c_{2m} P_{2m}(\cos\theta) \left(\frac{r}{a}\right)^{2m-2} \quad \text{if } r \leq a, \text{ internal domain} \quad (3.2.14\text{a})$$

$$= -A \sum_{m=0}^{\infty} (2m+1) c_{2m} P_{2m}(\cos\theta) \left(\frac{a}{r}\right)^{2m+3} \quad \text{if } r \geq a, \text{ external domain} \quad (3.2.14\text{b})$$

$$e_{\theta\theta} = A \left[2\delta(\cos\theta)\frac{a}{r} + \sum_{m=1}^{\infty} \frac{c_{2m}}{2m-1} \left(\frac{d^2 P_{2m}(\cos\theta)}{d\theta^2} + 2m P_{2m}(\cos\theta) \right) \left(\frac{r}{a}\right)^{2m-2} \right]$$
$$\text{if } r \leq a, \text{ internal domain} \quad (3.2.14\text{c})$$

$$= \frac{A}{2} \left(\frac{a}{r}\right)^3 \left[1 - \sum_{m=1}^{\infty} \frac{c_{2m}}{m+1} \left(\frac{d^2 P_{2m}(\cos\theta)}{d\theta^2} - (2m+1) P_{2m}(\cos\theta) \right) \left(\frac{a}{r}\right)^{2m} \right]$$
$$\text{if } r \geq a, \text{ external domain} \quad (3.2.14\text{d})$$

$$e_{\phi\phi} = A \sum_{m=1}^{\infty} \frac{c_{2m}}{2m-1} \left(\frac{\cos\theta}{\sin\theta} \frac{d P_{2m}(\cos\theta)}{d\theta} + 2m P_{2m}(\cos\theta) \right) \left(\frac{r}{a}\right)^{2m-2}$$
$$\text{if } r \leq a, \text{ internal domain} \quad (3.2.14\text{e})$$

$$= -A \sum_{m=0}^{\infty} c_{2m} \frac{c_{2m}}{2m+2} (\cos\theta) \left(\frac{\cos\theta}{\sin\theta} \frac{d P_{2m}(\cos\theta)}{d\theta} - (2m+1) P_{2m}(\cos\theta) \right) \left(\frac{a}{r}\right)^{2m+3}$$
$$\text{if } r \geq a, \text{ external domain} \quad (3.2.14\text{f})$$

$$e_{r\theta} = A \sum_{m=1}^{\infty} c_{2m} \frac{d P_{2m}(\cos\theta)}{d\theta} \left(\frac{r}{a}\right)^{2m-2} \quad \text{if } r \leq a, \text{ internal domain} \quad (3.2.14\text{g})$$

$$= A \sum_{m=1}^{\infty} c_{2m} \frac{d P_{2m}(\cos\theta)}{d\theta} \left(\frac{a}{r}\right)^{2m+3} \quad \text{if } r \geq a, \text{ external domain} \quad (3.2.14\text{h})$$

3.2.2 The half-space case: singular and non-singular terms

In our case, as it has already been discussed, we are dealing with a semi-infinite space, so it is necessary to resort to the Mindlin's tensor, whose components have been evaluated and are reported in the Appendix (section 6.2). In the following we will employ cartesian coordinates, referring to the source point as (x'_1, x'_2, x'_3) and to the receiving point as (x_1, x_2, x_3).

Before we are actually able to carry out the volume integrals in eq. 2.4.6, it is necessary to evaluate the sums of partial derivatives. If we managed somehow to write $\frac{\partial G_{ik}}{\partial x'_k}$ as the gradient of a scalar potential $\frac{\partial \Phi}{\partial x_i}$, then it would be possible to apply the same procedure explained in the previous subsection to solve for the displacement and stress fields both within the inclusion and the matrix.

Let us start with the first component of the displacement field $u_1(\mathbf{x})$, which is given by the volume integral:

$$u_1^c(\mathbf{x}) = 3K e_0 \int_{V_S} \frac{\partial G_{1k}}{\partial x'_k}(\mathbf{x}, \mathbf{x}') dv(\mathbf{x}') \quad (3.2.15)$$

The sum of partial derivatives we have to compute is the following:

$$\frac{\partial G_{11}}{\partial x_1'} + \frac{\partial G_{12}}{\partial x_2'} + \frac{\partial G_{13}}{\partial x_3'} \tag{3.2.16}$$

and the partial derivatives, calculated from the expressions of the respective Mindlin's tensor components, are

$$\frac{\partial G_{11}}{\partial x_1'} = C(x_1 - x_1') \left\{ \frac{(3-4\nu)}{R_1^3} + \frac{1}{R_2^3} - \frac{2}{R_1^3} + \frac{3(x_1 - x_1')^2}{R_1^5} - \frac{2(3-4\nu)}{R_2^3} \right.$$
$$+ \frac{3(3-4\nu)(x_1 - x_1')^2}{R_2^5} + \frac{6x_3 x_3'}{R_2^5}\left[1 - \frac{3(x_1 - x_1')^2}{R_2^2}\right] + \frac{12x_3 x_3'}{R_2^5}\left[1 - \frac{(x_1 - x_1')^2}{R_2^2}\right]$$
$$\left. + \frac{4(1-\nu)(1-2\nu)}{R_2(R_2 + x_3 + x_3')^2}\left[3 - \frac{2(x_1 - x_1')^2}{R_2(R_2 + x_3 + x_3')} - \frac{(x_1 - x_1')^2}{R_2^2}\right] \right\} \tag{3.2.17}$$

$$\frac{\partial G_{12}}{\partial x_2'} = C(x_1 - x_1')\left\{ -\frac{1}{R_1^3} - \frac{(3-4\nu)}{R_2^3} + \frac{6x_3 x_3'}{R_2^5} + \frac{4(1-\nu)(1-2\nu)}{R_2(R_2 + x_3 + x_3')^2}\right.$$
$$\left. + (x_2 - x_2')^2\left[\frac{3}{R_1^5} + \frac{3(3-4\nu)}{R_2^5} - \frac{30x_3 x_3'}{R_2^7} - \frac{4(1-\nu)(1-2\nu)}{R_2^2(R_2 + x_3 + x_3')^3}\left(\frac{R_2 + x_3 + x_3'}{R_2} + 2\right)\right]\right\} \tag{3.2.18}$$

$$\frac{\partial G_{13}}{\partial x_3'} = C(x_1 - x_1')\left\{ -\frac{1}{R_1^3} + \frac{3(x_3 - x_3')^2}{R_1^5} - \frac{3-4\nu}{R_2^3} - \frac{3(3-4\nu)(x_3 - x_3')(x_3 + x_3')}{R_2^5}\right.$$
$$\left. + \frac{6x_3(x_3 + x_3')}{R_2^5} + \frac{6x_3 x_3'}{R_2^5} - \frac{30x_3 x_3'(x_3 + x_3')^2}{R_2^7} + \frac{4(1-\nu)(1-2\nu)}{R_2^3}\right\} \tag{3.2.19}$$

where

$$R_1 = \sqrt{(x_1 - x_1')^2 + (x_2 - x_2')^2 + (x_3 - x_3')^2} \tag{3.2.20a}$$

$$R_2 = \sqrt{(x_1 - x_1')^2 + (x_2 - x_2')^2 + (x_3 + x_3')^2} \tag{3.2.20b}$$

$$C = \frac{1}{16\pi\mu(1-\nu)} \tag{3.2.20c}$$

If we substitute the expressions in eqs. 3.2.17, 3.2.18 and 3.2.19 into eq. 3.2.16, after some lenghty calculations which will not be reported here, we get the following expression for the first sum of partial derivatives:

$$\frac{\partial G_{1k}}{\partial x_k'} = C(x_1 - x_1')\left\{\frac{2(1-2\nu)}{R_1^3} + \frac{2(1-2\nu)(3-4\nu)}{R_2^3} - \frac{12(1-2\nu)x_3(x_3 + x_3')}{R_2^5}\right\} \tag{3.2.21}$$

The second component of the displacement field is given by:

$$u_2^c(\mathbf{x}) = 3Ke_0 \int_{V_S} \frac{\partial G_{2k}}{\partial x_k'}(\mathbf{x}, \mathbf{x}')dv(\mathbf{x}') \tag{3.2.22}$$

44

The sum to evaluate this time is

$$\frac{\partial G_{21}}{\partial x_1'} + \frac{\partial G_{22}}{\partial x_2'} + \frac{\partial G_{23}}{\partial x_3'} \tag{3.2.23}$$

and the partial derivatives are given by

$$\frac{\partial G_{21}}{\partial x_1'} = C(x_2 - x_2')\left\{ -\frac{1}{R_1^3} - \frac{3 - 4\nu}{R_2^3} + \frac{6x_3 x_3'}{R_2^5} + \frac{4(1-\nu)(1-2\nu)}{R_2(R_2 + x_3 + x_3')^2} \right.$$
$$\left. + (x_1 - x_1')^2 \left[\frac{3}{R_1^5} + \frac{3(3-4\nu)}{R_2^5} - \frac{30x_3 x_3'}{R_2^7} - \frac{4(1-\nu)(1-2\nu)}{R_2^2(R_2 + x_3 + x_3')^3}\left(\frac{R_2 + x_3 + x_3'}{R_2} + 2 \right) \right] \right\} \tag{3.2.24}$$

$$\frac{\partial G_{22}}{\partial x_2'} = C(x_2 - x_2')\left\{ \frac{3 - 4\nu}{R_1^3} + \frac{1}{R_2^3} - \frac{2}{R_1^3} + \frac{3(x_2 - x_2')^2}{R_1^5} - \frac{2(3-4\nu)}{R_2^3} + \frac{3(3-4\nu)(x_2 - x_2')^2}{R_2^5} \right.$$
$$+ \frac{6x_3 x_3'}{R_2^5}\left[1 - \frac{3(x_2 - x_2')^2}{R_2^2} \right] + \frac{12x_3 x_3'}{R_2^5}\left[1 - \frac{(x_2 - x_2')^2}{R_2^2} \right]$$
$$\left. + \frac{4(1-\nu)(1-2\nu)}{R_2(R_2 + x_3 + x_3')^2}\left[3 - \frac{2(x_2 - x_2')^2}{R_2(R_2 + x_3 + x_3')} - \frac{(x_2 - x_2')^2}{R_2^2} \right] \right\} \tag{3.2.25}$$

$$\frac{\partial G_{23}}{\partial x_3'} = C(x_2 - x_2')\left\{ -\frac{1}{R_1^3} + \frac{3(x_3 - x_3')^2}{R_1^5} - \frac{3 - 4\nu}{R_2^3} - \frac{3(3-4\nu)(x_3 - x_3')(x_3 + x_3')}{R_2^5} \right.$$
$$\left. - \frac{2(3-4\nu)}{R_2^3} + \frac{6x_3(x_3 + x_3')}{R_2^5} + \frac{6x_3 x_3'}{R_2^5} - \frac{30x_3 x_3'(x_3 + x_3')^2}{R_2^7} + \frac{4(1-\nu)(1-2\nu)}{R_2^3} \right\} \tag{3.2.26}$$

Again, if we substitute eqs. 3.2.24, 3.2.25 and 3.2.26 into eq. 3.2.23, we obtain the following expression:

$$\frac{\partial G_{2k}}{\partial x_k'} = C(x_2 - x_2')\left\{ \frac{2(1-2\nu)}{R_1^3} + \frac{2(1-2\nu)(3-4\nu)}{R_2^3} - \frac{12(1-2\nu)x_3(x_3 + x_3')}{R_2^5} \right\} \tag{3.2.27}$$

Finally, the third component of the displacement field is given by

$$u_3^c(\mathbf{x}) = 3Ke_0 \int_{V_S} \frac{\partial G_{3k}}{\partial x_k'}(\mathbf{x}, \mathbf{x}')dv(\mathbf{x}') \tag{3.2.28}$$

and the sum to evaluate is

$$\frac{\partial G_{31}}{\partial x_1'} + \frac{\partial G_{32}}{\partial x_2'} + \frac{\partial G_{33}}{\partial x_3'} \tag{3.2.29}$$

while the partial derivatives are

$$\frac{\partial G_{31}}{\partial x'_1} = C\left\{-\frac{x_3 - x'_3}{R_1^3} - \frac{(3-4\nu)(x_3 - x'_3)}{R_2^3} + \frac{6x_3 x'_3(x_3 + x'_3)}{R_2^5} - \frac{4(1-\nu)(1-2\nu)}{R_2(R_2 + x_3 + x'_3)}\right.$$

$$+ (x_1 - x'_1)^2\left[\frac{3(x_3 - x'_3)}{R_1^5} + \frac{3(3-4\nu)(x_3 - x'_3)}{R_2^5} - \frac{30x_3 x'_3(x_3 + x'_3)}{R_2^7}\right.$$

$$\left.\left.+ \frac{4(1-\nu)(1-2\nu)}{R_2^2(R_2 + x_3 + x'_3)^2}\left(\frac{R_2 + x_3 + x'_3}{R_2} + 1\right)\right]\right\}$$

$$(3.2.30)$$

$$\frac{\partial G_{32}}{\partial x'_2} = C\left\{-\frac{x_3 - x'_3}{R_1^3} - \frac{(3-4\nu)(x_3 - x'_3)}{R_2^3} + \frac{6x_3 x'_3(x_3 + x'_3)}{R_2^5} - \frac{4(1-\nu)(1-2\nu)}{R_2(R_2 + x_3 + x'_3)}\right.$$

$$+ (x_2 - x'_2)^2\left[\frac{3(x_3 - x'_3)}{R_1^5} + \frac{3(3-4\nu)(x_3 - x'_3)}{R_2^5} - \frac{30x_3 x'_3(x_3 + x'_3)}{R_2^7}\right.$$

$$\left.\left.+ \frac{4(1-\nu)(1-2\nu)}{R_2^2(R_2 + x_3 + x'_3)^2}\left(\frac{R_2 + x_3 + x'_3}{R_2} + 1\right)\right]\right\}$$

$$(3.2.31)$$

$$\frac{\partial G_{33}}{\partial x'_3} = C\left\{\frac{(3-4\nu)(x_3 - x'_3)}{R_1^3} - \frac{8(1-\nu)^2 - (3-4\nu)}{R_2^3}(x_3 + x'_3) - \frac{2(x_3 - x'_3)}{R_1^3} + \frac{3(x_3 - x'_3)^3}{R_1^5}\right.$$

$$- \frac{3(x_3 + x'_3)}{R_2^5}\left[(3-4\nu)(x_3 + x'_3)^2 - 2x_3 x'_3\right] + \frac{1}{R_2^3}\left[2(3-4\nu)(x_3 + x'_3) - 2x_3\right]$$

$$\left.+ \frac{6x_3(x_3 + x'_3)^2}{R_2^5} + \frac{12x_3 x'_3(x_3 + x'_3)}{R_2^5} - \frac{30x_3 x'_3(x_3 + x'_3)^3}{R_2^7}\right\}$$

$$(3.2.32)$$

Here too, after substituting eqs. 3.2.30, 3.2.31 and 3.2.32 into eq. 3.2.29, we get the following expression for the last sum of partial derivatives:

$$\frac{\partial G_{3k}}{\partial x'_k} = C\left\{\frac{2(1-2\nu)(x_3 - x'_3)}{R_1^3}\right.$$

$$\left.- \frac{2(1-2\nu)(3-4\nu)(x_3 + x'_3)}{R_2^3} - \frac{12(1-2\nu)x_3(x_3 + x'_3)^2}{R_2^5} + \frac{4(1-2\nu)x_3}{R_2^3}\right\}$$

$$(3.2.33)$$

Further details on these calculations can be found in the Appendix (section 6.4).

Here we report the expressions for the three components of the displacement field written in terms of triple integrals of the previous sums on the volume of the inclusion (namely, we integrate along the x'_3 coordinate from $c - \frac{d}{2}$ to $c + \frac{d}{2}$, that is the height of the cylinder; along the x'_2 coordinate from $-\sqrt{a^2 - (x'_1)^2}$ to $\sqrt{a^2 - (x'_1)^2}$, and along the x'_1 coordinate from $-a$ to a, thus accounting for the integration on the horizontal section of the cylinder):

$$u_1^c = 3KCe_0 \int_{-a}^{a} dx'_1 \int_{-\sqrt{a^2-(x'_1)^2}}^{\sqrt{a^2-(x'_1)^2}} dx'_2 \int_{c-\frac{d}{2}}^{c+\frac{d}{2}} dx'_3\ (x_1 - x'_1)\left\{\frac{2(1-2\nu)}{R_1^3}\right.$$

$$\left.+ \frac{2(1-2\nu)(3-4\nu)}{R_2^3} - \frac{12(1-2\nu)x_3(x_3 + x'_3)}{R_2^5}\right\}$$

$$(3.2.34)$$

46

$$u_2^c = 3KCe_0 \int_{-a}^{a} dx_1' \int_{-\sqrt{a^2-(x_1')^2}}^{\sqrt{a^2-(x_1')^2}} dx_2' \int_{c-\frac{d}{2}}^{c+\frac{d}{2}} dx_3' \; (x_2 - x_2') \left\{ \frac{2(1-2\nu)}{R_1^3} \right.$$

$$\left. + \frac{2(1-2\nu)(3-4\nu)}{R_2^3} - \frac{12(1-2\nu)x_3(x_3 + x_3')}{R_2^5} \right\}$$

(3.2.35)

$$u_3^c = 3KCe_0 \int_{-a}^{a} dx_1' \int_{-\sqrt{a^2-(x_2')^2}}^{\sqrt{a^2-(x_2')^2}} dx_2' \int_{c-\frac{d}{2}}^{c+\frac{d}{2}} dx_3' \; \left\{ \frac{2(1-2\nu)(x_3 - x_3')}{R_1^3} \right.$$

$$\left. - \frac{2(1-2\nu)(3-4\nu)(x_3 + x_3')}{R_2^3} - \frac{12(1-2\nu)x_3(x_3 + x_3')^2}{R_2^5} + \frac{4(1-2\nu)x_3}{R_2^3} \right\}$$

(3.2.36)

In order to solve for the three components of the displacement field, it would be useful if we manage to rewrite the integrands in eqs. 3.2.34, 3.2.35 and 3.2.36 as the gradient of a scalar potential, similarly to what has been done in the case of an unlimited space (subsection 3.2.1):

$$\frac{\partial G_{ik}}{\partial x_k'} = \frac{\partial \psi}{\partial x_i}$$

(3.2.37)

so that the displacement field could be expressed as

$$\mathbf{u^c}(\mathbf{x}) = A_0 \nabla \Phi(\mathbf{x})$$

where A_0 is a constant, and

$$\nabla \Phi(\mathbf{x}) = \int_{V_S} \nabla \psi(\mathbf{x}) dv(\mathbf{x}')$$

However, we can demonstrate that this is not possible in our case by calculating the curl of the sums of partial derivatives (eqs. 3.2.21, 3.2.27, 3.2.33).

It is known that if a vector field can be written as the gradient of a scalar potential, then it is irrotational: in three dimensions, this means that its curl must vanish. If we take the curl of the displacement vector $\mathbf{u^c}$ as it is written in eq. 2.4.6, then it is possible to bring the curl (which is taken with respect to the coordinates of the observation point x_i, while the integration is carried out over those of the source point x_i') inside the integral, thus obtaining in indicial notation:

$$(\boldsymbol{\nabla} \times \mathbf{u^c})_i = e_{ijk} \frac{\partial}{\partial x_j} u_k^c = 3Ke_0 \int_{V_S} e_{ijk} \frac{\partial}{\partial x_j} \left(\frac{\partial G_{km}}{\partial x_m'} \right) dv(\mathbf{x}')$$

(3.2.38)

If we develop the curl inside the integral, what we get is

$$e_{ijk} \frac{\partial}{\partial x_j} \left(\frac{\partial G_{km}}{\partial x_m'} \right) = \hat{i} \left(\frac{12(1-2\nu)(3-4\nu)(x_3 + x_3')(x_2 - x_2')}{R_2^5} - \frac{12(1-2\nu)x_3(x_2 - x_2')}{R_2^5} \right)$$

$$- \hat{j} \left(\frac{12(1-2\nu)(3-4\nu)(x_3 + x_3')(x_1 - x_1')}{R_2^5} - \frac{12(1-2\nu)x_3(x_1 - x_1')}{R_2^5} \right) \neq \mathbf{0}$$

(3.2.39)

which in general does not vanish, leading us to the conclusion that the displacement field is not irrotational, and so we cannot find a scalar potential with which we could rewrite the displacement field. The details of this calculation are reported as well in the Appendix (section 6.5).

At this stage, it would seem that the only way we can retrieve the displacement field is through the direct calculation of the triple integrals in eqs. 3.2.34, 3.2.35 and 3.2.36.

However, one thing we can notice in those expressions is that there is a common term depending on $\frac{1}{R_1^3}$. If we were to evaluate the integrals, such a term would diverge within the volume of the inclusion, leading to a singularity wherever the observation point coincides with the source one: $\mathbf{x} = \mathbf{x}' \to R_1 = 0$. For this reason, we will refer to these terms, and to whichever term shows a dependency from a power of $\frac{1}{R_1}$, as the *singular* terms.

The presence of a singular part in the volume integrals would increase considerably the difficulty in finding their analytical solution, but there is one characteristic that comes to our aid. Looking at the singular terms in eqs. 3.2.34, 3.2.35 and 3.2.36, we can see that they are formally identical to the result of the sum of the partial derivatives of the Somigliana tensor in eq. 3.2.1:

$$\frac{2(1-2\nu)(x_i - x_i')}{R_1^3} \sim \frac{(1-2\nu)}{8\pi\mu(1-\nu)}\frac{(x_i - x_i')}{R^3} \tag{3.2.40}$$

where $R_1 = R$, as they are defined in eqs. 3.2.2 and 3.2.20a.

This enables us to employ the same techniques explained in subsection 3.2.1, and to effectively write the singular terms as the gradient of a scalar potential. In fact, we can demonstrate that it is possible to employ exactly the same potential derived for a thin cylinder-shaped inclusion by Lamberti, 2017.

Let us consider the volume integral for the generic displacement component u_i^c in eqs. 3.2.34, 3.2.35, 3.2.36 and isolate the singular term, which is the same among all the three expressions:

$$3KCe_0 \int_{V_S} (x_i - x_i')\frac{2(1-2\nu)}{R_1^3}dv(\mathbf{x}') \tag{3.2.41}$$

Then, let us focus on the constants of the expression in eq. 3.2.41: $6KCe_0(1-2\nu)$, where C is defined in eq. 3.2.20c, e_0 is defined in eq. 2.4.3 and K is the drained isothermal bulk modulus in a homogeneous medium, which can be expressed as $K = \lambda + \frac{2}{3}\mu = \frac{2}{3}\frac{\mu(1+\nu)}{(1-2\nu)}$. If we substitute their respective expressions (leaving aside e_0) into their product, we get

$$6KCe_0(1-2\nu) = \frac{6(1-2\nu)e_0}{16\pi\mu(1-\nu)}\frac{2\mu(1+\nu)}{3(1-2\nu)} = e_0\frac{(1+\nu)}{(1-\nu)} \tag{3.2.42}$$

This, aside for the minus sign which is due to the rewriting of $\frac{\partial G_{ik}}{\partial x_k'}$ as the gradient of the potential, is the same constant as in eq. 3.2.3. Moreover, the whole expression of the singular term is equivalent to that of the sum of the partial derivatives of the Somiglana tensor. Hence, we can deal with the singular terms in the volume integrals for the displacement field in the same approach as in subsection 3.2.1:

$$e_0 \frac{(1+\nu)}{(1-\nu)} \int\limits_{V_S} (x_i - x_i') \frac{1}{R_1^3} dv(\mathbf{x}') = -e_1 \int\limits_{V_S} \frac{\partial}{\partial x_i} \left(\frac{1}{R_1} \right) dv(\mathbf{x}') = -e_1 \nabla \Phi(\mathbf{x}) \quad (3.2.43)$$

where $e_1 = e_0 \frac{(1+\nu)}{(1-\nu)}$ and the scalar potential Φ is defined in the same way as in eq. 3.2.4.

To conclude, we can use the same potential derived for a cylinder-shaped inclusion by Lamberti (2017), and the same solutions for the displacement and stress fields as well (which are reported in the Appendix, section 6.3), to treat the singular part of the volume integrals in eqs. 3.2.34, 3.2.35 and 3.2.36. This ensures the possibility to find an analytical solution at least for a part of our problem.

We can now proceed to the evaluation of the terms depending from powers of $\frac{1}{R_2}$ in our integrals, which we will refer to as the *non-singular* part. It is to say that these terms do not show singularities within the source region, as R_2, defined in eq. 3.2.20b, never vanishes in any point of the half-space $x_3 > 0$.

However, before we can go through this, we have to point out that one of the assumptions made in Lamberti (2017) to find the expression of the scalar potential for a cylindrical inclusion is that its height must be far smaller than its radius (i.e., the cylinder we considered in subsection 3.2.1 was in fact a disk with radius a and infinitesimal thickness db, see section 6.3).

Therefore, when parametrizing our deformation source, we must be careful not to exceed in the choice of its height compared to its horizontal dimensions. In the following, we will refer to the height of the cylinder as d, in accordance with fig. 3.1, and consider a case where the aspect ratio between height and radius $\frac{d}{a}$ is smaller than $\frac{1}{10}$ (in fact, $\frac{d}{a} = 0.08$, as we stated in section 3.1).

Here it is necessary to point out that, in the following of this work, whenever we are referring to a quantity depending on R_1, be it a displacement, strain or stress component, it will have the superscript "s" meaning "singular", while a quantity depending on R_2 will have the superscript "ns" meaning "non-singular". Another important remark is that from now on we will drop the superscript "c" when referring to the displacement, strain and stress fields evaluated in the half-space and within the inclusion through the Eshelby's method (section 2.1), so $\mathbf{u}^c \doteq \mathbf{u}$.

The next section will be devoted to the actual computation of the non-singular terms of the volume integrals for the displacement field in eqs. 3.2.34 to 3.2.36, and the retrieval of the displacement field both inside and outside the TPE region.

3.3   The displacement field

We have previously discussed how to handle the terms depending on the distance R_1 between the source (x_1', x_2', x_3') and the receiving (x_1, x_2, x_3) points in eqs. 3.2.34, 3.2.35 and 3.2.36. These terms can be interpreted as the contribution of the original deformation source to the displacement field in the half-space, while the non-singular terms, depending on R_2 (which is the distance between the receiving and the mirror source point $(x_1', x_2', -x_3')$), correspond to the mixed contribution of a mirror deformation source outside the half-space and to that of the Galerkin vector, both of

which are necessary to remove the tractions on the free surface. This same technique is employed to retrieve the displacement and stress fields for the Mogi source (Mogi, 1958).

Having put the singular terms aside, we can now focus on the non-singular ones. Here we report the expressions of the volume integrals in eqs. 3.2.34, 3.2.35 and 3.2.36, leaving only the terms depending on R_2:

$$
u_1^{ns} = 3KCe_0 \int\limits_{-a}^{a} dx_1' \int\limits_{-\sqrt{a^2-(x_1')^2}}^{\sqrt{a^2-(x_1')^2}} dx_2' \int\limits_{c-\frac{d}{2}}^{c+\frac{d}{2}} dx_3' \ (x_1 - x_1') \left\{ \frac{2(1-2\nu)(3-4\nu)}{R_2^3} \right.
$$
$$
\left. - \frac{12(1-2\nu)x_3(x_3 + x_3')}{R_2^5} \right\}
$$
(3.3.1)

$$
u_2^{ns} = 3KCe_0 \int\limits_{-a}^{a} dx_1' \int\limits_{-\sqrt{a^2-(x_1')^2}}^{\sqrt{a^2-(x_1')^2}} dx_2' \int\limits_{c-\frac{d}{2}}^{c+\frac{d}{2}} dx_3' \ (x_2 - x_2') \left\{ \frac{2(1-2\nu)(3-4\nu)}{R_2^3} \right.
$$
$$
\left. - \frac{12(1-2\nu)x_3(x_3 + x_3')}{R_2^5} \right\}
$$
(3.3.2)

$$
u_3^{ns} = -3KCe_0 \int\limits_{-a}^{a} dx_1' \int\limits_{-\sqrt{a^2-(x_1')^2}}^{\sqrt{a^2-(x_1')^2}} dx_2' \int\limits_{c-\frac{d}{2}}^{c+\frac{d}{2}} dx_3' \ \left\{ \frac{2(1-2\nu)(3-4\nu)(x_3 + x_3')}{R_2^3} \right.
$$
$$
\left. + \frac{12(1-2\nu)x_3(x_3 + x_3')^2}{R_2^5} - \frac{4(1-2\nu)x_3}{R_2^3} \right\}
$$
(3.3.3)

In the following, we will deal with one volume integral at a time, splitting it into its main terms and trying to achieve a fully analytical solution for each of them.

Let us begin with the first integral in eq. 3.3.1, which we rewrite as

$$
u_1^{ns} = 3KCe_0(I_a^1 + I_b^1)
$$
(3.3.4)

where

$$
I_a^1 = \int\limits_{-a}^{a} dx_2' \int\limits_{-\sqrt{a^2-(x_2')^2}}^{\sqrt{a^2-(x_2')^2}} dx_1' \int\limits_{c-\frac{d}{2}}^{c+\frac{d}{2}} dx_3' \ (x_1 - x_1') \frac{2(1-2\nu)(3-4\nu)}{R_2^3}
$$
(3.3.5a)

$$
I_b^1 = -\int\limits_{-a}^{a} dx_2' \int\limits_{-\sqrt{a^2-(x_2')^2}}^{\sqrt{a^2-(x_2')^2}} dx_1' \int\limits_{c-\frac{d}{2}}^{c+\frac{d}{2}} dx_3' \ (x_1 - x_1') \frac{12(1-2\nu)x_3(x_3 + x_3')}{R_2^5}
$$
(3.3.5b)

the superscript 1 meaning "relative to the first component of the displacement".

Availing ourselves of the tables of integrals reported in Gradshteyn and Ryzhik (2014), we can handle the first integral I_a^1 by integrating with respect to dx_1', and

then with respect to dx'_3 (note the change in the extremes of the interval of integration along x'_1 in eqs. 3.3.5a, 3.3.5b: from $-\sqrt{a^2-(x'_2)^2}$ to $\sqrt{a^2-(x'_2)^2}$):

$$I_a^1 = 2(1-2\nu)(3-4\nu)\int_{-a}^{a} dx'_2 \int_{-\sqrt{a^2-(x'_2)^2}}^{\sqrt{a^2-(x'_2)^2}} dx'_1 \int_{c-\frac{d}{2}}^{c+\frac{d}{2}} dx'_3 \, \frac{(x_1-x'_1)}{R_2^3} =$$

$$= 2(1-2\nu)(3-4\nu)\int_{-a}^{a} dx'_2 \int_{c-\frac{d}{2}}^{c+\frac{d}{2}} dx'_3 \left(\frac{1}{R_2^+}-\frac{1}{R_2^-}\right) =$$

$$= 2(1-2\nu)(3-4\nu)\int_{-a}^{a} dx'_2 \left[\ln\left(\frac{R_2|^+_{(c+\frac{d}{2})}+x_3+c+\frac{d}{2}}{R_2|^+_{(c-\frac{d}{2})}+x_3+c-\frac{d}{2}}\right) - \ln\left(\frac{R_2|^-_{(c+\frac{d}{2})}+x_3+c+\frac{d}{2}}{R_2|^-_{(c-\frac{d}{2})}+x_3+c-\frac{d}{2}}\right)\right]$$

$$(3.3.6)$$

where

$$R_2^+ = \sqrt{(x_2-x'_2)^2+(x_3+x'_3)^2+(x_1-\sqrt{a^2-(x'_2)^2})^2} \qquad (3.3.7a)$$

$$R_2^- = \sqrt{(x_2-x'_2)^2+(x_3+x'_3)^2+(x_1+\sqrt{a^2-(x'_2)^2})^2} \qquad (3.3.7b)$$

and $R_2|^\pm_{(c\pm\frac{d}{2})}$ means $R_2^\pm$ evaluated at point $(c\pm\frac{d}{2})$.

At this stage, however, we realize that there is no possibility to proceed further with the calculation, as there are no known analytical solutions to an integral whose form is like that of the last integrand in eq. 3.3.6. Therefore, we will resort to numerical computation to complete the resolution of I_a^1.

Now let us evaluate the second integral I_b^1 (eq. 3.3.7a), this time integrating first with respect to dx'_3, and then to dx'_1:

$$I_b^1 = -12(1-2\nu)\int_{-a}^{a} dx'_2 \int_{-\sqrt{a^2-(x'_2)^2}}^{\sqrt{a^2-(x'_2)^2}} dx'_1 \int_{c-\frac{d}{2}}^{c+\frac{d}{2}} dx'_3 \, (x_1-x'_1)\frac{x_3(x_3+x'_3)}{R_2^5} =$$

$$= 4(1-2\nu)\int_{-a}^{a} dx'_2 \int_{-\sqrt{a^2-(x'_2)^2}}^{\sqrt{a^2-(x'_2)^2}} dx'_1 \, x_3(x_1-x'_1)\left(\frac{1}{R_2|^3_{(c+\frac{d}{2})}}-\frac{1}{R_2|^3_{(c+\frac{d}{2})}}\right) = \quad (3.3.8)$$

$$= 4(1-2\nu)\int_{-a}^{a} dx'_2 \, x_3 \left[\frac{1}{R_2|^+_{(c+\frac{d}{2})}} - \frac{1}{R_2|^-_{(c+\frac{d}{2})}} - \frac{1}{R_2|^+_{(c-\frac{d}{2})}} + \frac{1}{R_2|^-_{(c-\frac{d}{2})}}\right]$$

Also in this case, we found that it is impossible to achieve a full analytical solution for the integral, which will be handled by means of numerical computation.

We now continue with the second non-singular integral (eq. 3.3.2), first rewriting it as

$$u_2^{ns} = 3KCe_0(I_a^2 + I_b^2) \qquad (3.3.9)$$

where

$$I_a^2 = \int\limits_{-a}^{a} dx_1' \int\limits_{-\sqrt{a^2-(x_1')^2}}^{\sqrt{a^2-(x_1')^2}} dx_2' \int\limits_{c-\frac{d}{2}}^{c+\frac{d}{2}} dx_3' \ (x_2 - x_2')\frac{2(1-2\nu)(3-4\nu)}{R_2^3} \tag{3.3.10a}$$

$$I_b^2 = -\int\limits_{-a}^{a} dx_1' \int\limits_{-\sqrt{a^2-(x_1')^2}}^{\sqrt{a^2-(x_1')^2}} dx_2' \int\limits_{c-\frac{d}{2}}^{c+\frac{d}{2}} dx_3' \ (x_2 - x_2')\frac{12(1-2\nu)x_3(x_3 + x_3')}{R_2^5} \tag{3.3.10b}$$

The procedure is equivalent to that of the previous case, except that this time we integrate with respect to dx_2' from $-\sqrt{a^2 - (x_1')^2}$ to $\sqrt{a^2 - (x_1')^2}$:

$$I_a^2 = 2(1-2\nu)(3-4\nu) \int\limits_{-a}^{a} dx_1' \int\limits_{-\sqrt{a^2-(x_1')^2}}^{\sqrt{a^2-(x_1')^2}} dx_2' \int\limits_{c-\frac{d}{2}}^{c+\frac{d}{2}} dx_3' \ \frac{(x_2 - x_2')}{R_2^3} =$$

$$= 2(1-2\nu)(3-4\nu) \int\limits_{-a}^{a} dx_1' \int\limits_{c-\frac{d}{2}}^{c+\frac{d}{2}} dx_3' \ \left(\frac{1}{R_2^+} - \frac{1}{R_2^-} \right) =$$

$$= 2(1-2\nu)(3-4\nu) \int\limits_{-a}^{a} dx_1' \ \left[\ln \left(\frac{R_2^+|_{(c+\frac{d}{2})} + x_3 + c + \frac{d}{2}}{R_2^+|_{(c-\frac{d}{2})} + x_3 + c - \frac{d}{2}} \right) - \ln \left(\frac{R_2^-|_{(c+\frac{d}{2})} + x_3 + c + \frac{d}{2}}{R_2^-|_{(c-\frac{d}{2})} + x_3 + c - \frac{d}{2}} \right) \right]$$

$$\tag{3.3.11}$$

$$I_b^2 = -12(1-2\nu) \int\limits_{-a}^{a} dx_1' \int\limits_{-\sqrt{a^2-(x_1')^2}}^{\sqrt{a^2-(x_1')^2}} dx_2' \int\limits_{c-\frac{d}{2}}^{c+\frac{d}{2}} dx_3' \ (x_2 - x_2')\frac{x_3(x_3 + x_3')}{R_2^5} =$$

$$= 4(1-2\nu) \int\limits_{-a}^{a} dx_1' \int\limits_{-\sqrt{a^2-(x_1')^2}}^{\sqrt{a^2-(x_1')^2}} dx_2' \ x_3(x_2 - x_2') \left(\frac{1}{R_2^3(c + \frac{d}{2})} - \frac{1}{R_2^3(c - \frac{d}{2})} \right) =$$

$$= 4(1-2\nu) \int\limits_{-a}^{a} dx_1' \ x_3 \left[\frac{1}{R_2^+|_{(c+\frac{d}{2})}} - \frac{1}{R_2^-|_{(c+\frac{d}{2})}} - \frac{1}{R_2^+|_{(c-\frac{d}{2})}} + \frac{1}{R_2^-|_{(c-\frac{d}{2})}} \right]$$

$$\tag{3.3.12}$$

where the functions R_2^+ and R_2^- are defined in the same way as, respectively, in eqs. 3.3.7a and 3.3.7b, provided that the dependencies from (x_1, x_1') and (x_2, x_2') are swapped.

Both the final integrands in eqs. 3.3.11 and 3.3.12 are of the same forms as those in eqs. 3.3.6 and 3.3.8, so it is not possible to find complete analytical solutions in this case as well.

Finally, we evaluate the third non-singular integral (eq. 3.3.3), rewriting it as

$$u_3^{ns} = -3KCe_0(I_a^3 + I_b^3) \tag{3.3.13}$$

where

$$I_a^3 = \int\limits_{-a}^{a} dx_1' \int\limits_{-\sqrt{a^2-(x_1')^2}}^{\sqrt{a^2-(x_1')^2}} dx_2' \int\limits_{c-\frac{d}{2}}^{c+\frac{d}{2}} dx_3' \; (x_3 + x_3')\frac{2(1-2\nu)(3-4\nu)}{R_2^3} \tag{3.3.14a}$$

$$I_b^3 = \int\limits_{-a}^{a} dx_1' \int\limits_{-\sqrt{a^2-(x_1')^2}}^{\sqrt{a^2-(x_1')^2}} dx_2' \int\limits_{c-\frac{d}{2}}^{c+\frac{d}{2}} dx_3' \left[\frac{12(1-2\nu)x_3(x_3+x_3')^2}{R_2^5} - \frac{4(1-2\nu)x_3}{R_2^3}\right] \tag{3.3.14b}$$

As usual, let us evaluate the integrals one by one:

$$I_a^3 = 2(1-2\nu)(3-4\nu)\int\limits_{-a}^{a} dx_2' \int\limits_{-\sqrt{a^2-(x_2')^2}}^{\sqrt{a^2-(x_2')^2}} dx_1' \int\limits_{c-\frac{d}{2}}^{c+\frac{d}{2}} dx_3' \; \frac{(x_3+x_3')}{R_2^3} =$$

$$= -2(1-2\nu)(3-4\nu)\int\limits_{-a}^{a} dx_2' \int\limits_{-\sqrt{a^2-(x_2')^2}}^{\sqrt{a^2-(x_2')^2}} dx_1' \left(\frac{1}{R_2|_{(c+\frac{d}{2})}} - \frac{1}{R_2|_{(c-\frac{d}{2})}}\right) = \tag{3.3.15}$$

$$= -2(1-2\nu)(3-4\nu)\int\limits_{-a}^{a} \left[\ln\left(\frac{R_2^+|_{(c+\frac{d}{2})} - x_1 + \sqrt{a^2-(x_2')^2}}{R_2^-|_{(c+\frac{d}{2})} - x_1 - \sqrt{a^2-(x_2')^2}}\right)\right.$$

$$\left. - \ln\left(\frac{R_2^+|_{(c-\frac{d}{2})} - x_1 + \sqrt{a^2-(x_2')^2}}{R_2^-|_{(c-\frac{d}{2})} - x_1 - \sqrt{a^2-(x_2')^2}}\right)\right]$$

$$I_b^3 = 4(1-2\nu)\int\limits_{-a}^{a} dx_2' \int\limits_{-\sqrt{a^2-(x_2')^2}}^{\sqrt{a^2-(x_2')^2}} dx_1' \int\limits_{c-\frac{d}{2}}^{c+\frac{d}{2}} dx_3' \left[\frac{3x_3(x_3+x_3')^2}{R_2^5} - \frac{x_3}{R_2^3}\right] =$$

$$= -4(1-2\nu)\int\limits_{-a}^{a} dx_2' dx_2' \int\limits_{-\sqrt{a^2-(x_2')^2}}^{\sqrt{a^2-(x_2')^2}} x_3 dx_1' \left(\frac{(x_3+c+\frac{d}{2})}{R_2^3|_{(c+\frac{d}{2})}} - \frac{(x_3+c-\frac{d}{2})}{R_2^3|_{(c-\frac{d}{2})}}\right) =$$

$$= 4(1-2\nu)\int\limits_{-a}^{a} dx_2' \; x_3 \left\{\left(x_3+c+\frac{d}{2}\right)\left[\frac{(x_1-\sqrt{a^2-(x_2')^2})}{R_2^+|_{(c+\frac{d}{2})}\left[(x_2-x_2')^2+(x_3+c+\frac{d}{2})^2\right]}\right.\right.$$

$$\left.- \frac{(x_1+\sqrt{a^2-(x_2')^2})}{R_2^-|_{(c+\frac{d}{2})}\left[(x_2-x_2')^2+(x_3+c+\frac{d}{2})^2\right]}\right] - \left(x_3+c-\frac{d}{2}\right)$$

$$\left[\frac{(x_1-\sqrt{a^2-(x_2')^2})}{R_2^+|_{(c-\frac{d}{2})}\left[(x_2-x_2')^2+(x_3+c-\frac{d}{2})^2\right]} - \frac{(x_1+\sqrt{a^2-(x_2')^2})}{R_2^-|_{(c-\frac{d}{2})}\left[(x_2-x_2')^2+(x_3+c-\frac{d}{2})^2\right]}\right]\right\}$$

$$\tag{3.3.16}$$

The functions $R_2^\pm$ are defined in the same way as in eqs. 3.3.7a and 3.3.7b.

Even in this last case, there is no possibility to provide a full analytical solution to the two integrals developed above, and we have to resort to numerical solutions too.

Now that we have at least semi-analytical expressions for the non-singular part of the volume integrals in the original equations (3.2.34, 3.2.35, 3.2.36), we can retrieve the complete solutions for the displacement field due to our TPE inclusion both in the external matrix and within the source region itself:

$$\mathbf{u} = \mathbf{u}^s + \mathbf{u}^{ns} \tag{3.3.17}$$

where $\mathbf{u}^s$ and $\mathbf{u}^{ns}$ are respectively the contribution due to the singular part and to the non-singular one. The three components of the latter vector $(u_1^{ns}, u_2^{ns}, u_3^{ns})$ are given by the expressions in eqs. 3.3.4, 3.3.9 and 3.3.13, together with the integrals we have just evaluated. The three components of the former vector (u_1^s, u_2^s, u_3^s) are taken directly from the expressions 3.2.11a, 3.2.11b for the internal domain, and 3.2.12a, 3.2.12b for the external domain, provided that they are previously converted to cartesian coordinates [1].
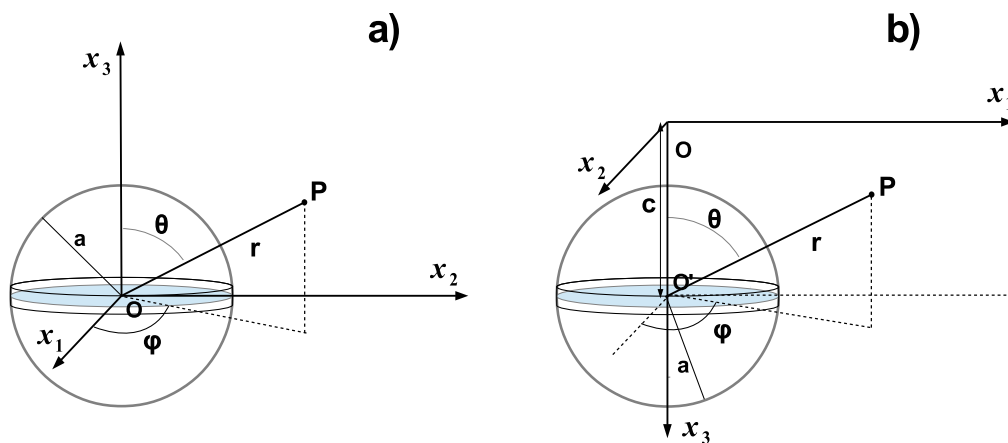
Figure 3.2: a): reference system adopted in the work of Lamberti (2017), where the median plane of the thin cylinder (highlighted in blue) embedded in an infinite space lies on the plane $x_3 = 0$, its origin coinciding with that of the system O. The internal domain $r \leq a$ coincides with the sphere of radius a surrounding the cylinder, while the rest of the space represents the external domain $r \geq a$. In this case, the radial distance r of a point P from the origin coincides with the distance from the center of the median plane of the cylinder. This is also reported in fig. 6.2. b): reference system adopted in our case, where the center O' of the median plane of the cylinder is located at $(0, 0, c)$, and it is chosen as the origin of the spherical reference system. The distance of a point P from O' is represented by the radial coordinate r, according to which we differentiate between the internal ($r \leq a$) and the external ($r \geq a$) domain. The other two spherical coordinates (θ, ϕ) employed in eqs. 3.3.18a, 3.3.18b, 3.3.18c are also shown.

Before we go any further, it is necessary to dwell on the definition of internal and external domains necessary to express the singular terms (see the Appendix, section 6.3), as it has to be updated to a new reference system we are employing in our case of study. With reference to fig. 3.2, we can see how, in the case of an infinitesimally thin cylinder of radius a in a complete space (Lamberti, 2017), the

---

[1]Before employing the scalar potential and the subsequent solutions derived in section 6.3, it is necessary to substitute d (the height of our cylinder) to db (the infinitesimal thickness of the disk considered by Lamberti, 2017) in the definition of the constant A (eq. 6.3.8).

origin of the reference system coincides with the center of the median plane of the cylinder, so the radial distance r from it is what discriminates between the internal $r \leq a$ and the external $r \geq a$ domain.

On the contrary, in the case of a cylinder embedded in a half-space, the origin no longer coincides with the center of its median plane. What we will do is to first evaluate the singular solutions for the displacement (i.e. those provided by Lamberti, 2017) in spherical coordinates, taking as the origin of the reference system the center of the cylinder itself, then converting them into cartesian coordinates, and eventually computing the non-singular solutions in the new cartesian frame, where the center of the median plane is at depth c below the origin.

Now we are ready to display the complete solution for the displacement field $\mathbf{u}$ by developing the terms of eq. 3.3.17:

$$u_1^s(x_1, x_2, x_3) = \sin\theta\cos\phi u_r^s + \cos\theta\cos\phi u_t^s \qquad (3.3.18a)$$

$$u_2^s(x_1, x_2, x_3) = \sin\theta\sin\phi u_r^s + \cos\theta\sin\phi u_t^s \qquad (3.3.18b)$$

$$u_3^s(x_1, x_2, x_3) = -\cos\theta u_r^s + \sin\theta u_t^s \qquad (3.3.18c)$$

are the cartesian components of the singular part of the displacement $\mathbf{u}^s$, where $u_r^s(r, \theta, \phi), u_t^s(r, \theta, \phi)$ are given respectively by eqs. 3.2.11a, 3.2.11b in the internal domain, and eqs. 3.2.12a, 3.2.12b in the external domain. It is important to bear in mind that the positive vertical axis of our reference system points downward, so the formulae for the conversion from spherical to cartesian coordinates employed in eqs. 3.3.18a, 3.3.18b and 3.3.18c must be changed accordingly (a more detailed discussion on this topic can be found in the Appendix (section 6.6); see also fig. 3.2).

The total displacement field is thus given by

$$u_1(x_1, x_2, x_3) = u_1^s(x_1, x_2, x_3) + 3KCe_0(I_a^1 + I_b^1) \qquad (3.3.19a)$$

$$u_2(x_1, x_2, x_3) = u_2^s(x_1, x_2, x_3) + 3KCe_0(I_a^2 + I_b^2) \qquad (3.3.19b)$$

$$u_3(x_1, x_2, x_3) = u_3^s(x_1, x_2, x_3) + 3KCe_0(I_a^3 + I_b^3) \qquad (3.3.19c)$$

The numerical computation of the integrals $I_{a,b}^i$ has been done using MatLab software. We choose to display the components of the displacement field on the median plane ($x_3 = c$) of the cylindrical inclusion along the x_1-axis on a $2D$ plot ($x_2 = 0$), symmetrically with respect to the origin, as it can be seen in fig. 3.3 and fig. 3.4, where the boundaries of the cylinder and the region within it are also shown.

The horizontal components u_1 and u_2 are represented in fig. 3.3. It is to say that, as we are plotting along the x_1-axis at $x_2 = 0$, the first component u_1 would correspond to the radial one (u_ρ) in cylindrical coordinates (and thus it shows a symmetric pattern around the origin), while the second component u_2 would correspond to the azimuthal one (u_ϕ), and in fact it is zero, as the problem is axi-symmetric.

The vertical uplift (corresponding to $-u_3$, as the positive vertical axis points downward in our reference system) is represented in fig. 3.4, together with the uplift due exclusively to the singular vertical component of the displacement field u_3^s. Since the latter corresponds to the case of an infinite space, the vertical displacement on the median plane is expected to be zero, given the symmetry of the problem. The

non-singular contribution adds a non-vanishing vertical displacement that accounts for the symmetric pattern of the total uplift.

Later on in the following of this work (section 3.5) we will discuss the displacement and the stresses at the free surface as well.
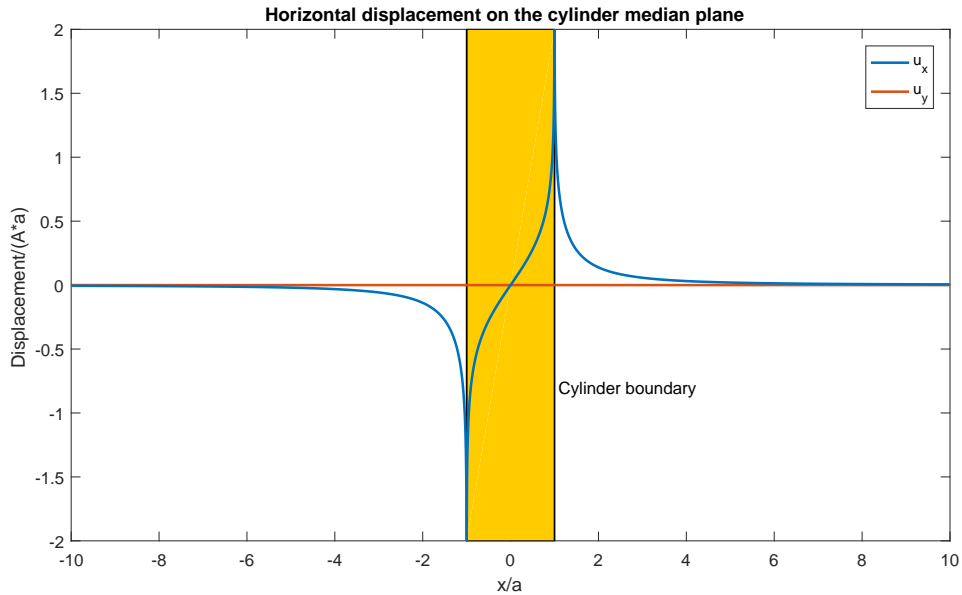
Figure 3.3: Horizontal components of displacement u_1 (blue line) and u_2 (red line) on the median plane of the cylinder ($x_3 = c$) plotted along the x_1-axis. The x-axis, spanning from $-5000m$ to $+5000m$, is normalized to the radius $a = 500m$ of the cylinder, while the y-axis is normalized to the product Aa, where A is the constant defined in eq. 6.3.8. The two black lines mark the edges of the cylinder, and the orange-highlighted area corresponds to the source region.
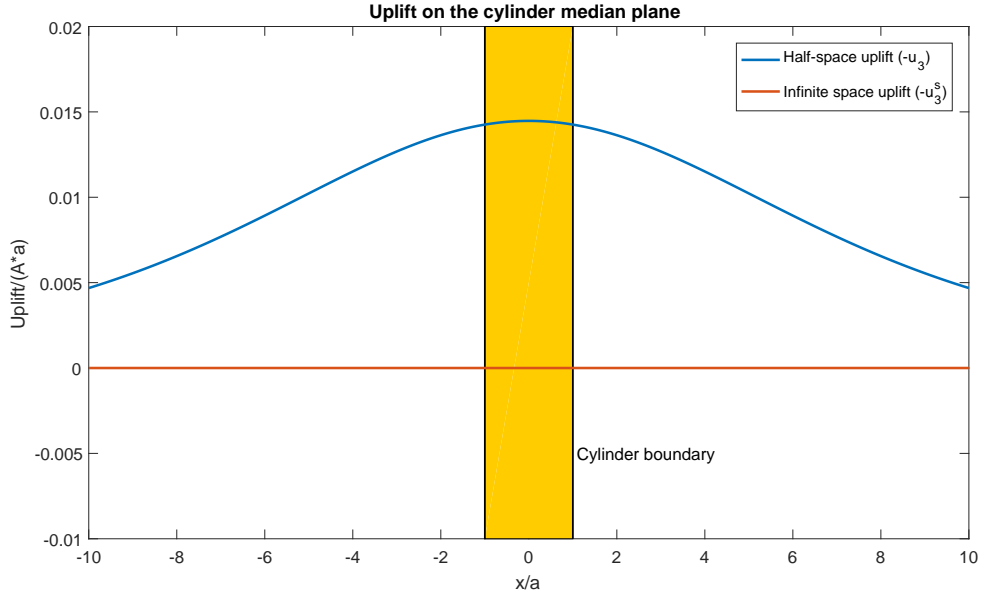
Figure 3.4: Vertical uplift on the median plane of the cylinder $-u_3$ (blue line) on the median plane of the cylinder ($x_3 = c$), together with the vertical uplift due only to the singular component $-u_3^s$ (red line), which is what we would observe in an infinite space, both plotted along the x_1-axis. The x-axis, spanning from $-5000m$ to $+5000m$, is normalized to the radius $a = 500m$ of the cylinder, while the y-axis is normalized to the product Aa, where A is the constant defined in eq. 6.3.8. The two black lines mark the edges of the cylinder, and the orange-highlighted area corresponds to the source region.

Now that we have completed the discussion about the displacement field, we can move on to the retrieval of the stress field both within and outside the TPE source region.

3.4 Stress tensor inside and outside the source region

The approach we will follow to evaluate the components of the stress tensor inside the inclusion and within the rest of the half-space is the same as that employed in the last section for the components of the displacement field: namely, starting from the expressions in eqs. 3.2.34, 3.2.35 and 3.2.36, we will use the results of Lamberti (2017) to solve for the singular terms, then deriving the rest to get the strain components e_{ij}, and from those, applying the elastic[2] constitutive relation, the stress components.

Before that, it is useful to take a step back to section 2.1 and recall how the stress tensor was defined both inside (eq. 2.1.3) and outside (eq. 2.1.2) the inclusion. Here we rewrite for completeness those expressions for the stress inside ("in") and outside ("out") the inclusion as

$$\tau_{ij}^c = \lambda e_{kk}^c \delta_{ij} + 2\mu e_{ij}^c$$
$$\tau_{ij}^{out} = \tau_{ij}^c$$
$$\tau_{ij}^{in} = \tau_{ij}^c + \tau_{ij}^*$$

where $\tau_{ij}^* = -3Ke_0\delta_{ij}$ (eq. 2.4.5). From now on, the superscript "c" will be dropped for the strain and stress components as well (so $\tau_{ij}^c \doteq \tau_{ij}$). We have to keep in mind that τ_{ij} is due to both the singular and non-singular terms, as it depends on $\mathbf{u}$: $\tau_{ij}^c = \tau_{ij}^s + \tau_{ij}^{ns}$.

The expressions for the singular strain tensor components e_{ij}^s have already been shown in eqs. 3.2.20a to 3.2.14h, and they will be used to account for the contribution of the singular terms to the whole stress field.

Therefore, by analogy with the evaluation of the displacement, we will focus on the retrieval of the non-singular contribution τ_{ij}^{ns}:

$$\tau_{ij}^{ns} = \lambda \frac{\partial u_k^{ns}}{\partial x_k}\delta_{ij} + 2\mu e_{ij}^{ns} \tag{3.4.2a}$$

$$e_{ij}^{ns} = \frac{1}{2}\left(\frac{\partial u_i^{ns}}{\partial x_j} + \frac{\partial u_j^{ns}}{\partial x_i}\right) \tag{3.4.2b}$$

In order to compute the strain and stress components, we need to write the partial derivatives of the components of the displacement, according to eq. 3.4.2a. In the following, we will limit ourselves to report the diagonal components of the stress tensor, namely τ_{11}^{ns}, τ_{22}^{ns} and τ_{33}^{ns}. This is due to the fact that the shear stress components τ_{12}^{ns}, τ_{13}^{ns}, τ_{23}^{ns} all vanish both within and outside the TPE inclusion, as it is explained in the Appendix (section 6.7). Given that also the shear components of the singular stress tensor vanish within the source region (as it is shown in the Appendix as well, section 6.3), the stress tensor diagonal elements represent the principal stress eigenvalues, thus giving direct information on the stress regime inside the inclusion.

---

[2]The elastic constitutive relation $\tau_{ij} = \lambda e_{kk}\delta_{ij} + 2\mu e_{ij}$ can be applied to the poro-elastic matrix provided that isothermal and drained parameters λ, μ are employed, see section 2.4.

The partial derivatives we need are thus:

$$\frac{\partial u_1^{ns}}{\partial x_1}, \frac{\partial u_2^{ns}}{\partial x_2}, \frac{\partial u_3^{ns}}{\partial x_3}$$

It is to say that all of the following results represent the most complete analytical solutions we have managed to find. In most cases, as for the displacement components, we reduce the volume integrals to single ones, which are to be computed numerically.

Let us begin with the first partial derivative, $\frac{\partial u_1^{ns}}{\partial x_1}$. With reference to eq. 3.3.1, we can write

$$\frac{\partial u_1^{ns}}{\partial x_1} = 3KCe_0 \int\limits_{-a}^{a} dx_2 \int\limits_{-\sqrt{a^2-(x_2')^2}}^{\sqrt{a^2-(x_2')^2}} dx_1' \int\limits_{c-\frac{d}{2}}^{c+\frac{d}{2}} dx_3' \frac{\partial}{\partial x_1} \left\{ (x_1 - x_1') \left[\frac{2(1-2\nu)(3-4\nu)}{R_2^3} \right. \right.$$
$$\left. \left. - \frac{12(1-2\nu)x_3(x_3 + x_3')}{R_2^5} \right] \right\}$$

(3.4.3)

Here it is worth pointing out that, as the partial derivative is taken with respect to x_1 whereas the second integration is over dx_1', we have put the former inside the integral. Furthermore, it is easy to demonstrate that

$$\frac{\partial u_1^{ns}}{\partial x_1} = -\frac{\partial u_1^{ns}}{\partial x_1'}$$

(3.4.4)

so we can rewrite the integral employing this relation, thus simplifying its resolution, in that it enables us to avoid calculating the whole derivative:

$$\frac{\partial u_1^{ns}}{\partial x_1} = -3KCe_0 \int\limits_{-a}^{a} dx_2 \int\limits_{-\sqrt{a^2-(x_2')^2}}^{\sqrt{a^2-(x_2')^2}} dx_1' \int\limits_{c-\frac{d}{2}}^{c+\frac{d}{2}} dx_3' \frac{\partial}{\partial x_1'} \left\{ (x_1 - x_1') \left[\frac{2(1-2\nu)(3-4\nu)}{R_2^3} \right. \right.$$
$$\left. \left. - \frac{12(1-2\nu)x_3(x_3 + x_3')}{R_2^5} \right] \right\} = -3KCe_0 \frac{\partial}{\partial x_1'} (I_a^1 + I_b^1)$$

(3.4.5)

where the integrals I_a^1 and I_b^1 are defined in eqs. 3.3.5a and 3.3.5b. Let us handle the two separately:

$$\frac{\partial}{\partial x_1'} I_a^1 = 2(1-2\nu)(3-4\nu) \int\limits_{-a}^{a} dx_2' \left\{ (x_1 - f(x_2')) \left[\frac{x_3 + c + \frac{d}{2}}{[(x_2 - x_2')^2 + (x_1 - f(x_2'))R_2^+|_{(c+\frac{d}{2})}} \right. \right.$$
$$\left. - \frac{x_3 + c - \frac{d}{2}}{[(x_2 - x_2')^2 + (x_1 - f(x_2'))]R_2^+|_{(c-\frac{d}{2})}} \right] - (x_1 + f(x_2'))$$
$$\left[\frac{x_3 + c + \frac{d}{2}}{[(x_2 - x_2')^2 + (x_1 + f(x_2'))]R_2^-|_{(c+\frac{d}{2})}} - \frac{x_3 + c - \frac{d}{2}}{[(x_2 - x_2')^2 + (x_1 + f(x_2'))]R_2^-|_{(c-\frac{d}{2})}} \right] \right\}$$

(3.4.6)

where $f(x_2') \doteq \sqrt{a^2 - (x_2')^2}$ to lighten the formulae (this notation will be used throughout the rest of the section).

$$\frac{\partial}{\partial x_1'} I_b^1 = 4(1 - 2\nu)x_3 \int\limits_{-a}^{a} dx_2' \left[\frac{(x_1 - f(x_2'))}{R_2^+|_{(c+\frac{d}{2})}^3} - \frac{(x_1 - f(x_2'))}{R_2^+|_{(c-\frac{d}{2})}^3} - \frac{(x_1 + f(x_2'))}{R_2^-|_{(c+\frac{d}{2})}^3} + \frac{(x_1 + f(x_2'))}{R_2^-|_{(c-\frac{d}{2})}^3} \right]$$
(3.4.7)

where R_2^+, R_2^- are defined in eqs. 3.3.7a, 3.3.7b, and the details of the calculations have been omitted.

Proceeding with the second partial derivative, from eq. 3.3.2 we get

$$\frac{\partial u_2^{ns}}{\partial x_2} = -3KCe_0 \int\limits_{-a}^{a} dx_1' \int\limits_{-\sqrt{a^2-x'1^2}}^{\sqrt{a^2-x'1^2}} dx_2' \int\limits_{c-\frac{d}{2}}^{c+\frac{d}{2}} dx_3' \frac{\partial}{\partial x_2'} \left\{ (x_2 - x_2') \left[\frac{2(1-2\nu)(3-4\nu)}{R_2^3} \right. \right.$$
$$\left. \left. - \frac{12(1-2\nu)x_3(x_3 + x_3')}{R_2^5} \right] \right\} = -3KCe_0 \frac{\partial}{\partial x_2'}(I_a^2 + I_b^2)$$
(3.4.8)

where the integrals I_a^2 and I_b^2 are defined in eqs. 3.3.10a and 3.3.10b, and we have already used the property stated in eq. 3.4.4, which holds true also for $\frac{\partial u_2^{ns}}{\partial x_2}$. The integration of the two terms gives us:

$$\frac{\partial}{\partial x_2'} I_a^2 = 2(1-2\nu)(3-4\nu) \int\limits_{-a}^{a} dx_1' \left\{ (x_2 - f(x_1')) \left[\frac{x_3 + c + \frac{d}{2}}{[(x_1 - x_1')^2 + (x_2 - f(x_1'))]R_2^+|_{(c+\frac{d}{2})}} \right. \right.$$
$$\left. - \frac{x_3 + c - \frac{d}{2}}{[(x_1 - x_1')^2 + (x_2 - f(x_1'))]R_2^+|_{(c-\frac{d}{2})}} \right] - (x_2 + f(x_1')) \left[\frac{x_3 + c + \frac{d}{2}}{[(x_1 - x_1')^2 + (x_2 + f(x_1'))]R_2^-|_{(c+\frac{d}{2})}} \right.$$
$$\left. \left. - \frac{x_3 + c - \frac{d}{2}}{[(x_1 - x_1')^2 + (x_2 + f(x_1'))]R_2^-|_{(c-\frac{d}{2})}} \right] \right\}$$
(3.4.9)

$$\frac{\partial}{\partial x_2'} I_b^2 = 4(1 - 2\nu)x_3 \int\limits_{-a}^{a} dx_1' \left[\frac{(x_2 - f(x_1'))}{R_2^+|_{(c+\frac{d}{2})}^3} - \frac{(x_2 - f(x_1'))}{R_2^+|_{(c-\frac{d}{2})}^3} - \frac{(x_2 + f(x_1'))}{R_2^-|_{(c+\frac{d}{2})}^3} + \frac{(x_2 + f(x_1'))}{R_2^-|_{(c-\frac{d}{2})}^3} \right]$$
(3.4.10)

Notice that this time the integration is carried out first with respect to dx_3' and then to dx_2', and the definition of R_2^+, R_2^- changes accordingly (cfr. eq. 3.3.12), while $f(x_1') \doteq \sqrt{a^2 - (x_1')^2}$.

Finally, we calculate the third partial derivative. From eq. 3.3.3 we can write

$$\frac{\partial u_3^{ns}}{\partial x_3} = -3KCe_0 \int\limits_{-a}^{a} dx_2' \int\limits_{-\sqrt{a^2-(x_2')^2}}^{\sqrt{a^2-(x_2')^2}} dx_1' \int\limits_{c-\frac{d}{2}}^{c+\frac{d}{2}} dx_3' \; \frac{\partial}{\partial x_3} \left[\frac{2(1-2\nu)(3-4\nu)(x_3+x_3')}{R_2^3} \right.$$

$$\left. + \frac{12(1-2\nu)x_3(x_3+x_3')^2}{R_2^5} - \frac{4(1-2\nu)x_3}{R_2^3} \right] = -3KCe_0 \frac{\partial}{\partial x_3}(I_a^3 + I_b^3)$$

$$(3.4.11)$$

where the integrals I_a^3 and I_b^3 are defined in eqs. 3.3.14a and 3.3.14b. This time, however, it is not possible to employ a relation similar to that in eq. 3.4.4, so we have to explicitly carry out the partial derivative of I_a^3 and I_b^3:

$$\frac{\partial}{\partial x_3}I_a^3 = -2(1-2\nu)(3-4\nu) \int\limits_{-a}^{a} dx_2' \int\limits_{-\sqrt{a^2-(x_2')^2}}^{\sqrt{a^2-(x_2')^2}} dx_1' \; \frac{\partial}{\partial x_3} \left(\frac{1}{R_2|_{(c+\frac{d}{2})}} - \frac{1}{R_2|_{(c-\frac{d}{2})}} \right)$$

$$= -2(1-2\nu)(3-4\nu) \int\limits_{-a}^{a} dx_2' \left\{ -(x_3+c+\frac{d}{2}) \left[-\frac{x_1-f(x_2')}{[(x_2-x_2')^2+(x_3+c+\frac{d}{2})^2]R_2^+|_{(c+\frac{d}{2})}} \right. \right.$$

$$\left. + \frac{x_1+f(x_2')}{[(x_2-x_2')^2+(x_3+c+\frac{d}{2})^2]R_2^-|_{(c+\frac{d}{2})}} \right] - (x_3+c-\frac{d}{2})$$

$$\left. \left[\frac{x_1-f(x_2')}{[(x_2-x_2')^2+(x_3+c-\frac{d}{2})^2]R_2^+|_{(c-\frac{d}{2})}} - \frac{x_1+f(x_2')}{[(x_2-x_2')^2+(x_3+c-\frac{d}{2})^2]R_2^-|_{(c-\frac{d}{2})}} \right] \right\}$$

$$(3.4.12)$$

$$\frac{\partial}{\partial x_3}I_b^3 = -4(1-2\nu)\frac{\partial}{\partial x_3} \int\limits_{-a}^{a} dx_2' \int\limits_{-\sqrt{a^2-(x_2')^2}}^{\sqrt{a^2-(x_2')^2}} dx_1' \; x_3 \left(\frac{(x_3+c+\frac{d}{2})}{R_2^3|_{(c+\frac{d}{2})}} - \frac{(x_3+c-\frac{d}{2})}{R_2^3|_{(c-\frac{d}{2})}} \right)$$

$$= -4(1-2\nu) \int\limits_{-a}^{a} dx_2' \int\limits_{-\sqrt{a^2-(x_2')^2}}^{\sqrt{a^2-(x_2')^2}} dx_1' \; \left\{ \left(\frac{(x_3+c+\frac{d}{2})}{R_2^3|_{(c+\frac{d}{2})}} - \frac{(x_3+c-\frac{d}{2})}{R_2^3|_{(c-\frac{d}{2})}} \right) + \frac{x_3}{R_2^3|_{(c+\frac{d}{2})}} \right.$$

$$\left. - \frac{x_3}{R_2^3|_{(c-\frac{d}{2})}} - \frac{3x_3(x_3+c+\frac{d}{2})^2}{R_2^5|_{(c+\frac{d}{2})}} + \frac{3x_3(x_3+c-\frac{d}{2})^2}{R_2^5|_{(c-\frac{d}{2})}} \right\}$$

$$(3.4.13)$$

where $f(x_2')$ and $R_2^\pm$ are defined as usual.

Here it is important noticing that in the expression for $\frac{\partial}{\partial x_3}I_b^3$ we stopped the calculations once we got a double integral. As a matter of fact, we have found that it is theoretically possible to proceed with the analytical computation and reduce the double integral to a single one, but we have found it difficult to apply numerical computation to that solution: therefore, we choose to omit that last step and display the result which we effectively used to compute $\frac{\partial u_3^{ns}}{\partial x_3}$.

The non-singular strain components are given by

$$e_{11}^{ns} = \frac{\partial u_1}{\partial x_1} \tag{3.4.14a}$$

$$e_{22}^{ns} = \frac{\partial u_2}{\partial x_2} \tag{3.4.14b}$$

$$e_{33}^{ns} = \frac{\partial u_3}{\partial x_3} \tag{3.4.14c}$$

At this point we are able to obtain the total stress field τ_{ij} by developing the expression $\tau_{ij} = \tau_{ij}^s + \tau_{ij}^{ns}$. The diagonal components of τ_{ij}^{ns} are found by converting the singular strain components in eqs. from 3.2.20a to 3.2.14h from spherical to cartesian coordinates:

$$e_{11}^s = e_{rr} \sin^2\theta \cos^2\phi + 2e_{r\theta} \sin\theta \cos\theta \cos^2\phi + e_{\theta\theta} \cos^2\theta \cos^2\phi + e_{\phi\phi} \sin^2\phi \tag{3.4.15a}$$

$$e_{22}^s = e_{rr} \sin^2\phi \sin^2\theta + 2e_{r\theta} \cos\theta \sin\theta \sin^2\phi + e_{\theta\theta} \cos^2\theta \sin^2\phi + e_{\phi\phi} \cos^2\phi \tag{3.4.15b}$$

$$e_{33}^s = e_{rr} \cos^2\theta - 2e_{r\theta} \sin\theta \cos\theta + e_{\theta\theta} \sin^2\theta \tag{3.4.15c}$$

The formulae to convert a second rank tensor from a spherical to a cartesian set of coordinates are illustrated in the Appendix (section 6.6).

The singular stress components are thus retrieved by applying the elastic constitutive relation, bearing in mind that the stress tensor reported in the Appendix, eqs. 6.3.9a to 6.3.9d, is purely deviatoric outside the TPE inclusion:

$$\tau_{ij}^{s,out} = 2\mu e_{ij}^s \tag{3.4.16a}$$

$$\tau_{ij}^{s,in} = \frac{1}{3}\tau_{kk}^s + 2\mu e_{ij}^{s,d} \tag{3.4.16b}$$

where $e_{ij}^{s,d} = e_{ij}^s - \frac{1}{3}e_1\delta_{ij}$ is the deviatoric strain tensor, and $\frac{1}{3}\tau_{kk}^s = -\frac{4}{3}\mu e_1$ is the isotropic component of the stress tensor, which is non-vanishing only within the source region (as it is demonstrated in Lamberti, 2017).

The total stress components are thus given by

$$\tau_{ij}^{out} = 2\mu e_{ij}^s + \tau_{ij}^{ns} \tag{3.4.17a}$$

$$\tau_{ij}^{in} = \frac{1}{3}\tau_{kk}^s + 2\mu e_{ij}^{s,d} + \tau_{ij}^{ns} \tag{3.4.17b}$$

while the deviatoric stress components are as follows:

$$\tau_{ij}^{d,out} = 2\mu \left(e_{ij}^s + e_{ij}^{ns} - \frac{1}{3}e_{kk}^{ns}\delta_{ij} \right) \tag{3.4.18a}$$

$$\tau_{ij}^{d,in} = 2\mu \left(2\mu e_{ij}^s - \frac{1}{3}e_1\delta_{ij} + e_{ij}^{ns} - \frac{1}{3}e_{kk}^{ns}\delta_{ij} \right) \tag{3.4.18b}$$

In the following we report a series of plots representing the stress tensor components along the x_1-axis on the median plane of the cylindrical inclusion, both inside and outside of it.
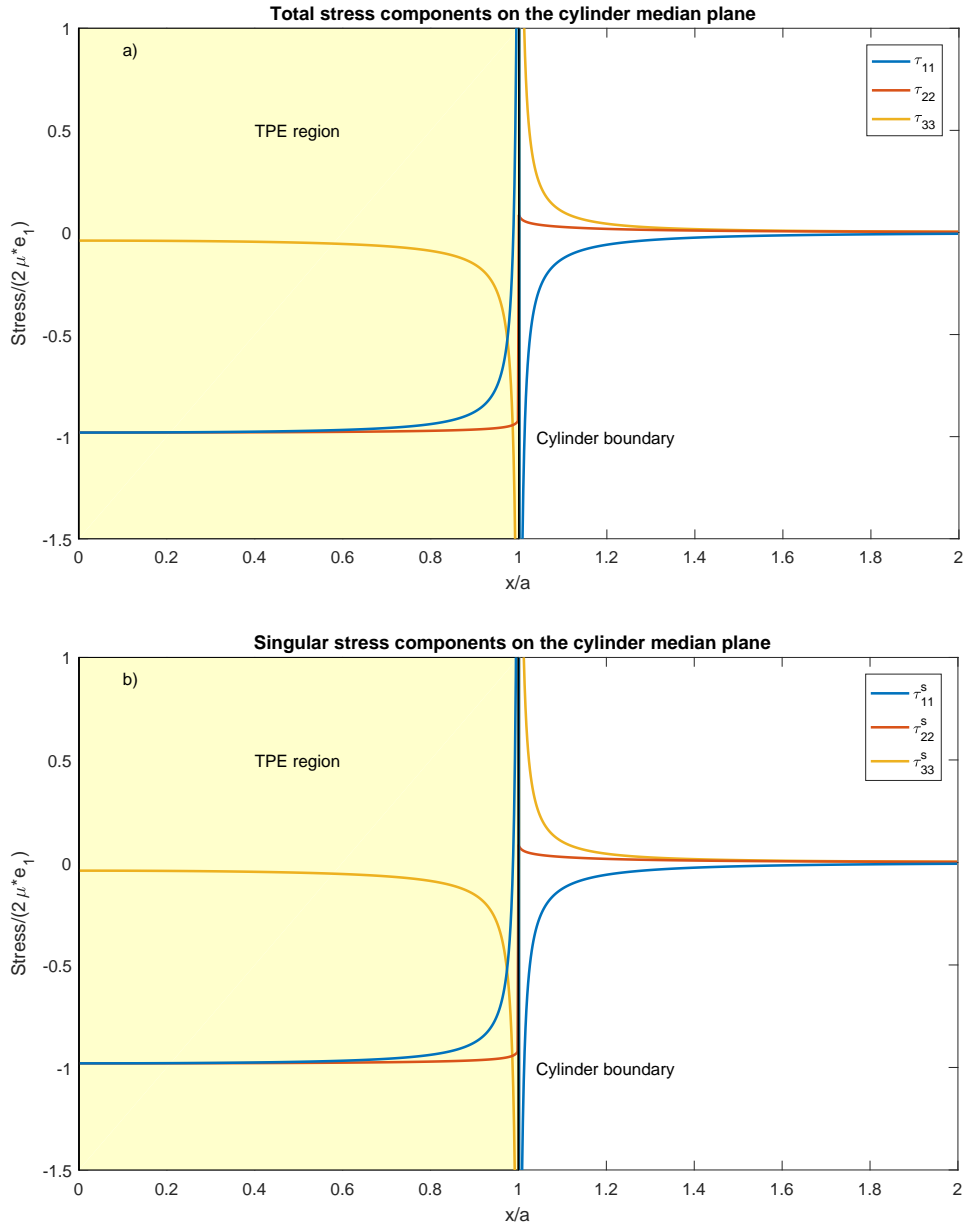
Figure 3.5: Fig. a): diagonal components of the stress tensor τ_{ij} on the median plane of the cylindrical inclusion, plotted along the x_1-axis. Fig. b): diagonal components of the singular stress tensor τ_{ij}^s on the median plane of the cylindrical inclusion. In both figures, the x-axis spans from $0m$ to $1000m$, and it is normalized to the radius $a = 500m$ of the cylinder. The stresses on the y-axis are normalized to $2\mu e_1$, where e_1 is defined in eq. 3.2.8. The interior of the TPE region is highlighted in pale yellow.

The stress tensor components represented in fig. 3.5 a) are compared to the components due only to the singular part of the problem in fig. 3.5 b), which correspond to the case where the source depth is big enough to neglect the free surface and approximate the half-space as an infinite one (these were also the results of the work of Lamberti, 2017). In our case we set the source depth $c = 3000m$ and its radius $a = 500m$, so the horizontal dimensions of the cylinder are considerably smaller than the depth of its median plane, and in fact, comparing the two plots,

the stress components are hardly distinguishable, if not at all.

The same can be told about the plots of the deviatoric stress components, total (fig. 3.6 a)) and singular (fig. 3.6 b)).
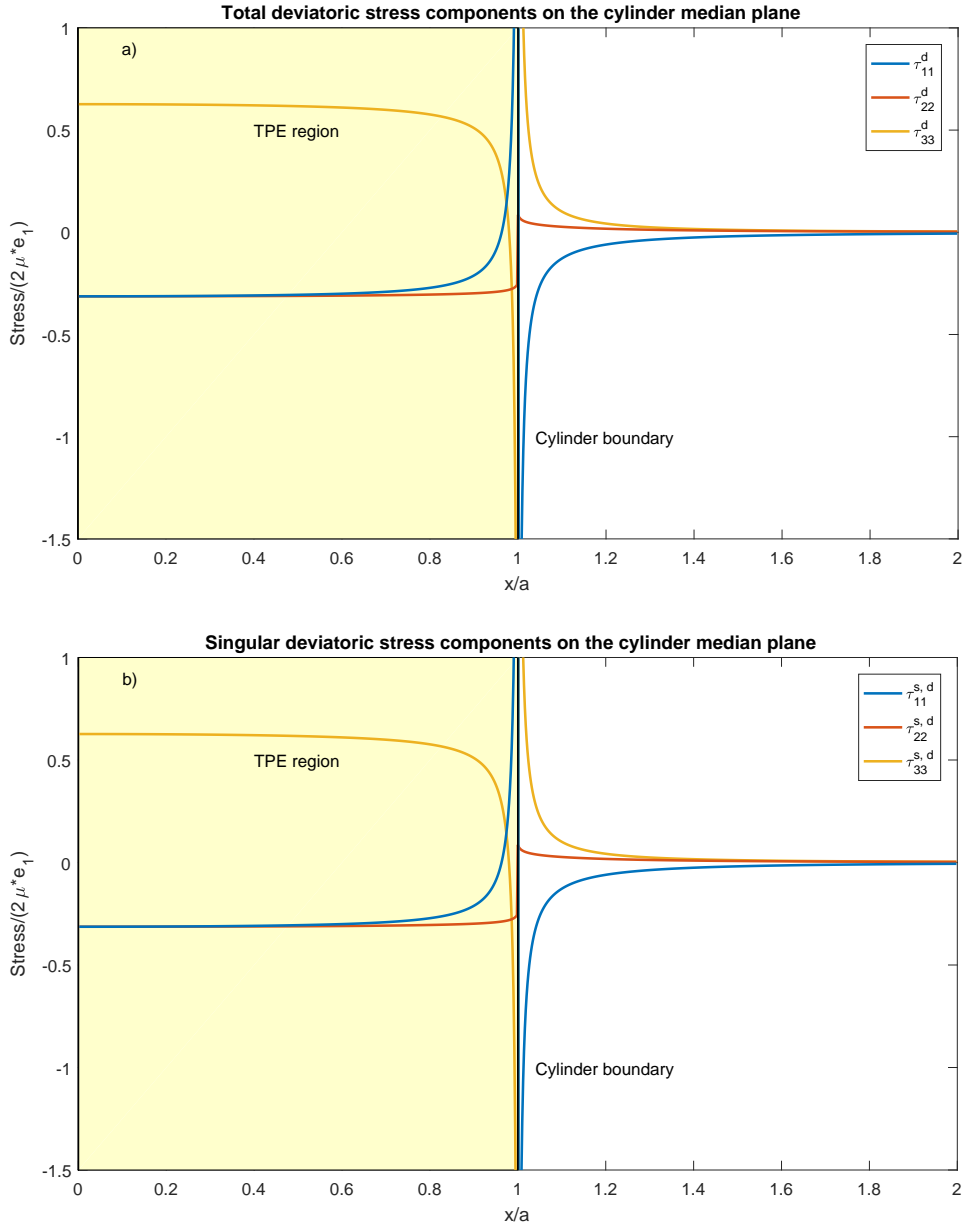
Figure 3.6: Fig. a): diagonal components of the deviatoric stress tensor τ_{ij}^d on the median plane of the cylindrical inclusion, plotted along the x_1-axis. Fig. b): diagonal components of the singular deviatoric stress tensor $\tau_{ij}^{s,d}$ on the median plane of the cylindrical inclusion. In both figures, the x-axis spans from $0m$ to $1000m$, and it is normalized to the radius $a = 500m$ of the cylinder. The stresses on the y-axis are normalized to $2\mu e_1$, where e_1 is defined in eq. 3.2.8. The black line at $x = 1$ marks the edge of the cylinder, and the interior of the TPE region is highlighted in pale yellow.

The deviatoric stress components in fig. 3.6 a) can give us information on the stress regime inside and outside the TPE region on its median plane. As we have already explained, the stress tensor is diagonal within the source region, so the diagonal components of its deviatoric counterpart τ_{11}^d, τ_{22}^d, τ_{33}^d coincide with the principal deviatoric stresses σ_1', σ_2', σ_3', where $\sigma_1' \leq \sigma_2' \leq \sigma_3'$, meaning that σ_1' is the most compressive (negative) deviatoric stress, and σ_3' is the most tensile (positive).

From the plot it is straightforward to see that

$$\tau_{33}^d = \sigma_3', \quad \tau_{11}^d = \sigma_2', \quad \tau_{22}^d = \sigma_1' \qquad (3.4.19)$$

Hence, looking at fig. 3.6 a), we have a tensile deviatoric stress τ_{33}^d along the vertical axis, a compressive one τ_{22}^d along the x_2-axis, which in this case (being $x_2 = 0$) corresponds to the transverse axis, while the intermediate deviatoric stress τ_{11}^d is along the x_1-axis, which corresponds to the radial axis.

This configuration holds from $x_1 = 0$ to approximately $x_1 = 0.974$, where τ_{11}^d becomes greater than τ_{33}^d and the order of principal stresses changes, and it suggests the presence of a compressive environment within most of the source region (let us point out that the situation would be the same if we plotted on the negative x_1-axis, given the symmetry of the inclusion), thus favouring thrust faulting mechanisms. Moreover, the kinds of faults which are more likely to develop are radial ones, as the intermediate deviatoric stress axis coincides with the x_1 (radial) axis.

The change in the order of principal deviatoric stresses near the boundary of the cylinder would indicate a different stress regime, where the intermediate stress axis would coincide with the vertical one, and the most tensile stress would act along the x_1-axis, favouring the development of ring faults. However, it is to say that the series employed to express the singular displacement, strain and stress components (starting from the potential defined in the Appendix, eqs. 6.3.5a and 6.3.5b) may attain large values in the proximity of $r = x_1 = a$, as indeed it can be seen around the border of the cylinder in the plots.

Looking at the outside region ($x_1 \geq a$), we notice that the tectonic enviroment is compressive again, given that the most tensile stress is again along the vertical axis, even if this time the most compressive stress is along the x_1-axis. The values of the stresses, however, are so small with respect to those within the source region that the seismicity they could account for in the medium surrounding the inclusion would be negligible (at least at depth c, on the median plane of the source).

3.5 Stress and displacement fields on the free surface

This section is devoted to the study and discussion of the displacement and stress components as they are on the free surface of the half-space ($x_3 = 0$). The displacement components are especially interesting, as they represent the only physical quantity we can actually observe and compare to geodetic data.

Let us start with the displacement. The horizontal components u_1 and u_2 are represented in fig. 3.7, while the vertical uplift (which is given by $-u_3$) is shown in fig. 3.8.
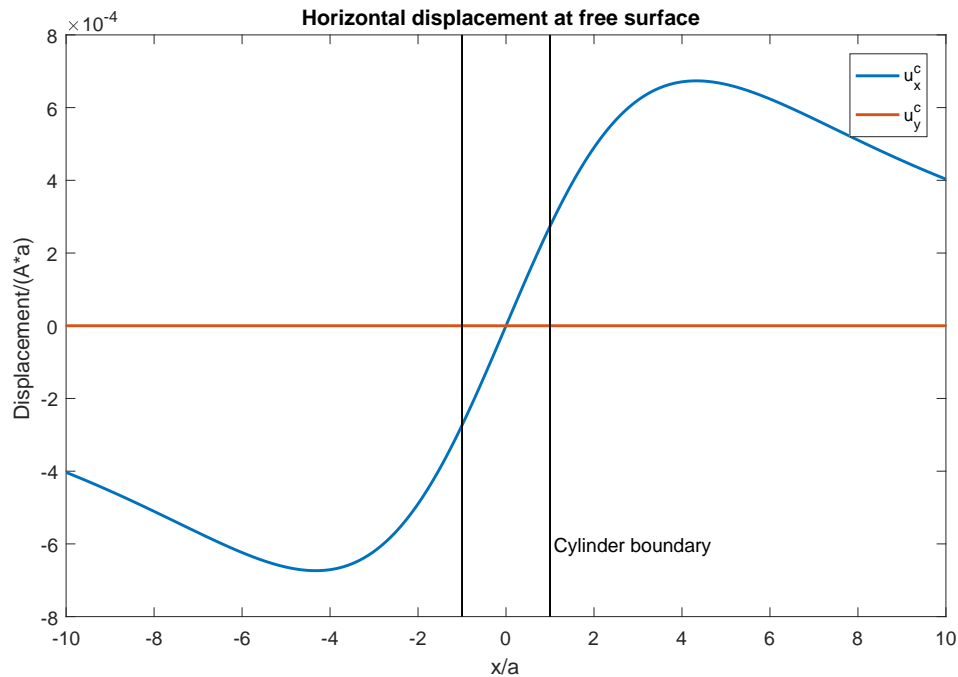
Figure 3.7: Horizontal components of displacement u_1 (blue line) and u_2 (red line) on the free surface $x_3 = 0$ plotted along the x_1-axis. The x-axis, spanning from $-5000m$ to $+5000m$, is normalized to the radius $a = 500m$ of the cylinder, while the y-axis is normalized to the product Aa, where A is the constant defined in eq. 6.3.8. The two black lines mark the projections of the edges of the cylinder on the surface.

Looking at the plot of the uplift in fig. 3.8, we can notice that it follows a symmetric, bell-shaped pattern centered around the origin (which corresponds to the center of the TPE region at depth c). This gives us a first consistency with what we would expect from a deformation source model describing the surface deformation pattern in a hydrothermal region such as Campi Flegrei, where a similar pattern was observed for the vertical ground displacement during the 1982-84 unrest episode, as we have seen in section 1.2 (see also fig. 1.2).
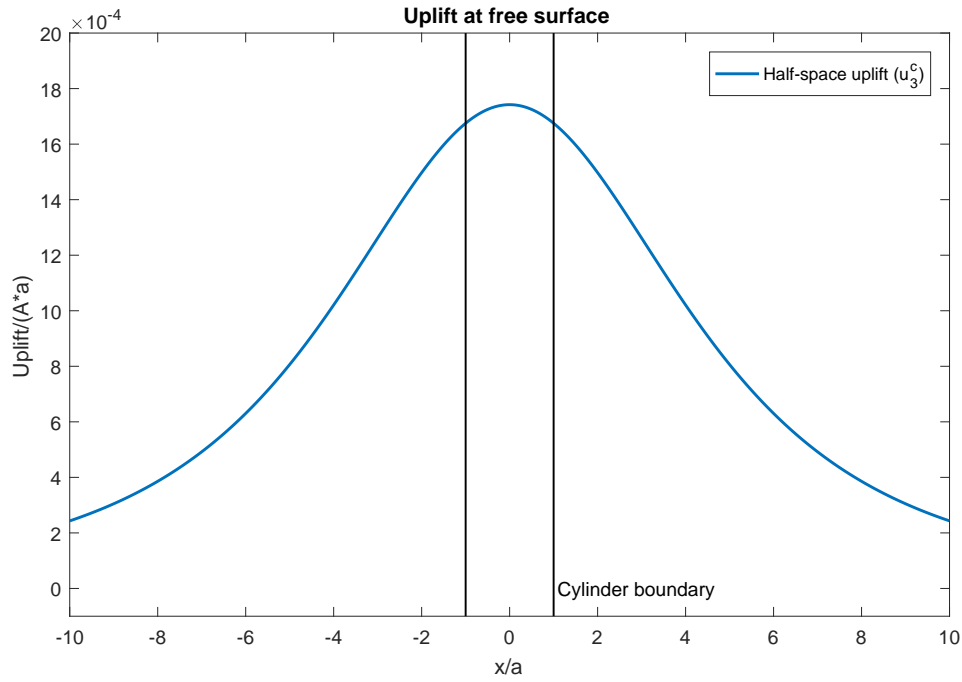
Figure 3.8: Vertical uplift on the median plane of the cylinder $-u_3$ (blue line) on the free surface $x_3 = 0$ plotted along the x_1-axis. The x-axis, spanning from $-5000m$ to $+5000m$, is normalized to the radius $a = 500m$ of the cylinder, while the y-axis is normalized to the product Aa, where A is the constant defined in eq. 6.3.8. The two black lines mark the projections of the edges of the cylinder on the surface.

Proceeding with the stresses, the total and deviatoric components are represented in the following figures.
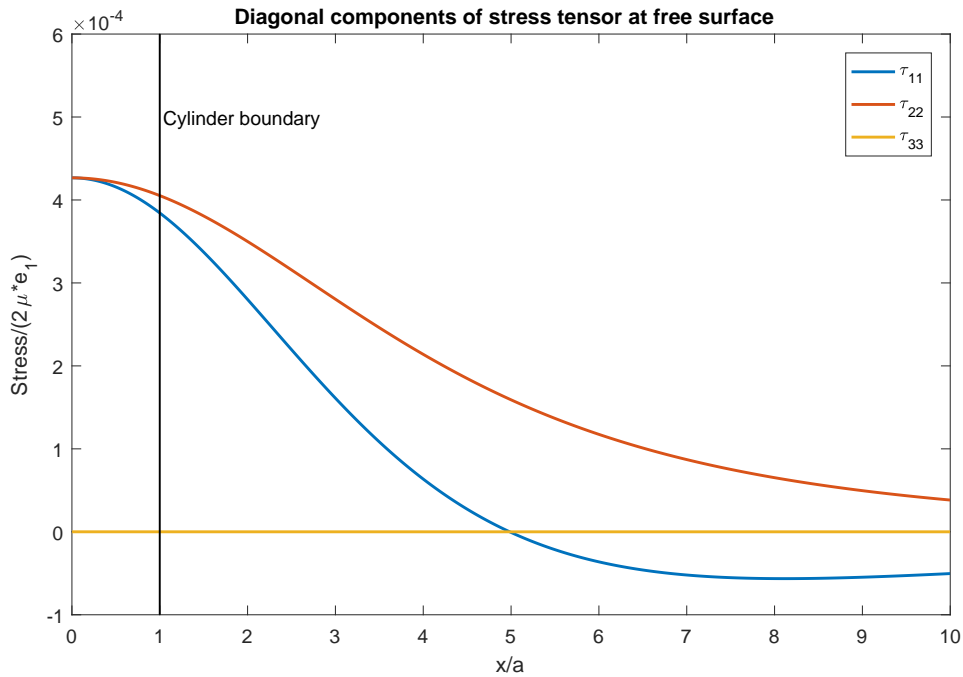
Figure 3.9: Diagonal components of the stress tensor τ_{ij} on the free surface $x_3 = 0$, plotted along the x_1-axis. The x-axis spans from $0m$ to $5000m$, and it is normalized to the radius $a = 500m$ of the cylinder. The stresses on the y-axis are normalized to $2\mu e_1$, where e_1 is defined in eq. 3.2.8. The black line marks the projection of the edge of the cylinder on the surface.

The diagonal components of the stress tensor are shown in fig. 3.9. Here it is worth noticing that the stress component τ_{33} is zero everywhere on the free surface, as we would expect by definition.

The diagonal deviatoric components are illustrated in fig. 3.10. It can be seen that the compressive (negative) deviatoric stress is τ_{33}^d from the origin to around $x = 5$, while the other two deviatoric stresses are both tensile (positive), τ_{22}^d (acting along the transverse axis) being the biggest. This suggests a distensive tectonic environment in the region of the half-space immediately above the deformation source, extending also at its sides. This region would likely see the formation of normal faults. After $x = 5$, τ_{33}^d becomes the intermediate deviatoric stress, suggesting a strike-slip stress regime.
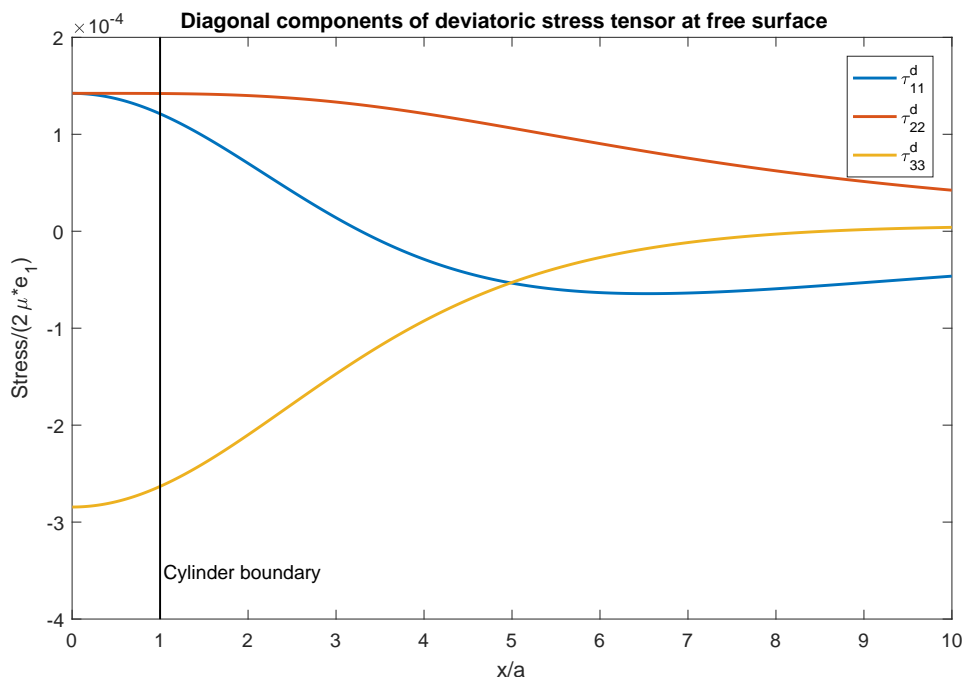
Figure 3.10: Diagonal components of the deviatoric stress tensor τ_{ij}^d on the free surface $x_3 = 0$, plotted along the x_1-axis. The x-axis spans from $0m$ to $5000m$, and it is normalized to the radius $a = 500m$ of the cylinder. The stresses on the y-axis are normalized to $2\mu e_1$, where e_1 is defined in eq. 3.2.8. The black line marks the projection of the edge of the cylinder on the surface.

3.6 Comparison with results from a fully numerical approach

The last section of this chapter is devoted to the comparison of the results we have presented so far with those of the same model we considered, although handled through a completely numerical method not developed in this thesis, which employs a surface distribution of orthogonal forces on the surface of the cylindrical inclusion to account for the traction discontinuity on it (see section 2.4 and eq. 2.4.6).

It should be noted that the geometric and poro-elastic parameters of the TPE source and the surrounding medium are the same as those we employed (section 3.1), and that the components of the Green's function used in the resolution are the same we retrieved for the Mindlin's tensor in section 2.5 (reported in the Appendix, section 6.2).

The comparison between the total and deviatoric stress results on the median plane of the cylinder are shown in fig. 3.11. As it can be noticed, the results are in very good agreement, except for the immediate surroundings of the edge of the cylinder ($x = 1$ in both plots), where both the two methods have issues in dealing with the singularities at $R_1 = a$ (see the Appendix, section 6.3). The comparison between the components of displacement on the median plane is reported instead in fig. 3.12, and the agreement between the results is good, except for a slight difference between the vertical components.
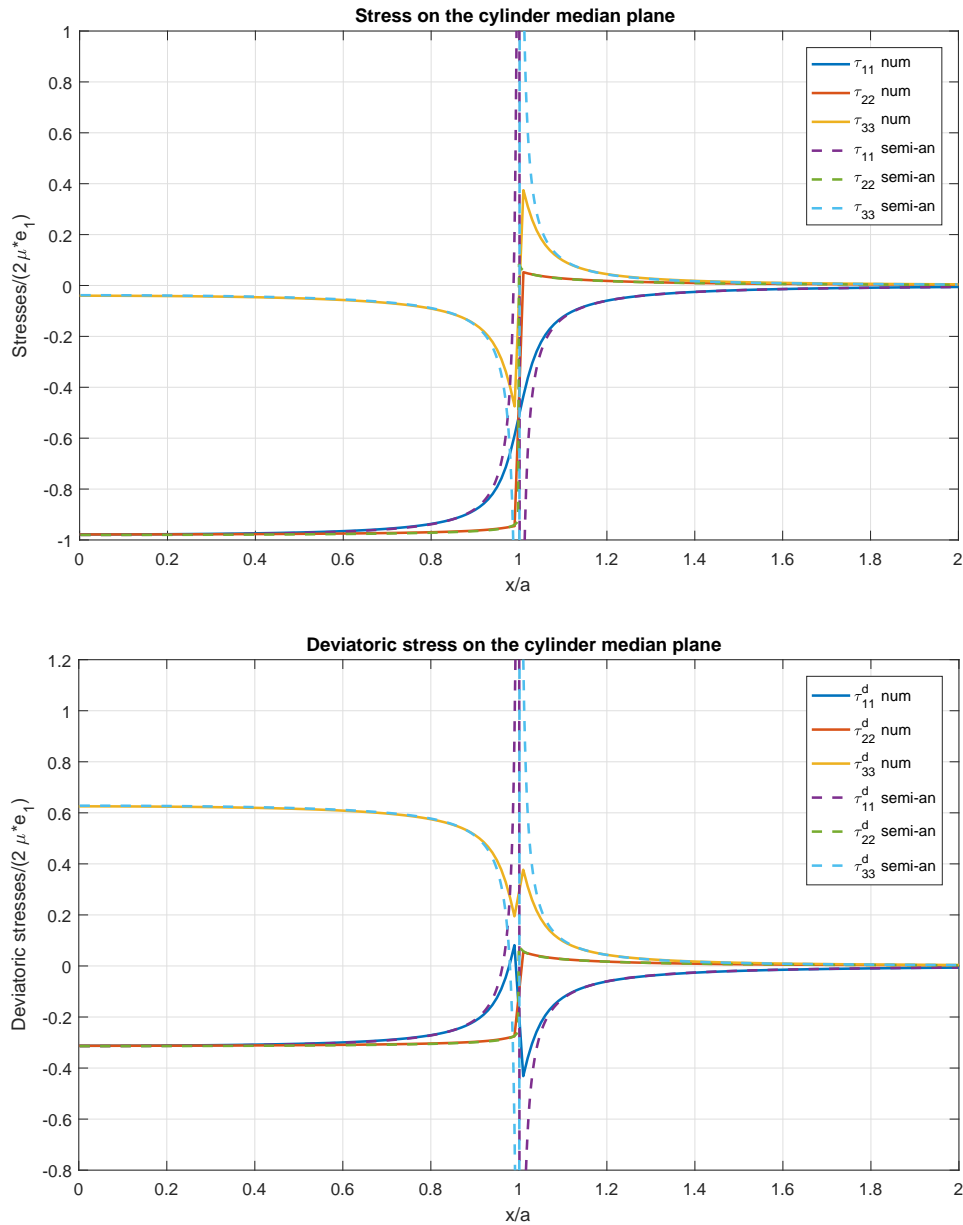
Figure 3.11: Top figure: comparison between the diagonal components of the stress tensor τ_{ij} "num", meaning fully numerical (solid lines), and those obtained through our method τ_{ij} "semi-an", meaning "semi-analytical" (dashed lines), on the median plane of the cylindrical inclusion, plotted along the x_1-axis. Bottom figure: comparison between the diagonal components of the deviatoric stress tensor τ_{ij}^d "num", meaning fully numerical (solid lines), and those obtained through our method τ_{ij}^d "semi-an" (dashed lines), meaning "semi-analytical", on the median plane of the cylindrical inclusion, plotted along the x_1-axis. In both figures, the x-axis is normalized to the radius $a = 500m$ of the cylinder. The stresses on the y-axis are normalized to $2\mu e_1$, where e_1 is defined in eq. 3.2.8.

Figure 3.12: Comparison between the displacement components u_1, u_2, u_3 "num", meaning fully numerical (solid lines), and those obtained through our method u_1, u_2, u_3 "semi-an", meaning "semi-analytical" (dashed lines), on the median plane of the cylindrical inclusion, plotted along the x_1-axis. The x-axis is normalized to the radius $a = 500m$ of the cylinder, while the y-axis is normalized to the product Aa, where A is the constant defined in eq. 6.3.8.

Similarly, the comparison between the total and deviatoric stress results on the free surface are shown in fig. 3.13. As it can be noticed, the results are in very good agreement everywhere. This holds true for the comparison between the components of displacement on the free surface as well, as it can be noticed in fig. 3.14.
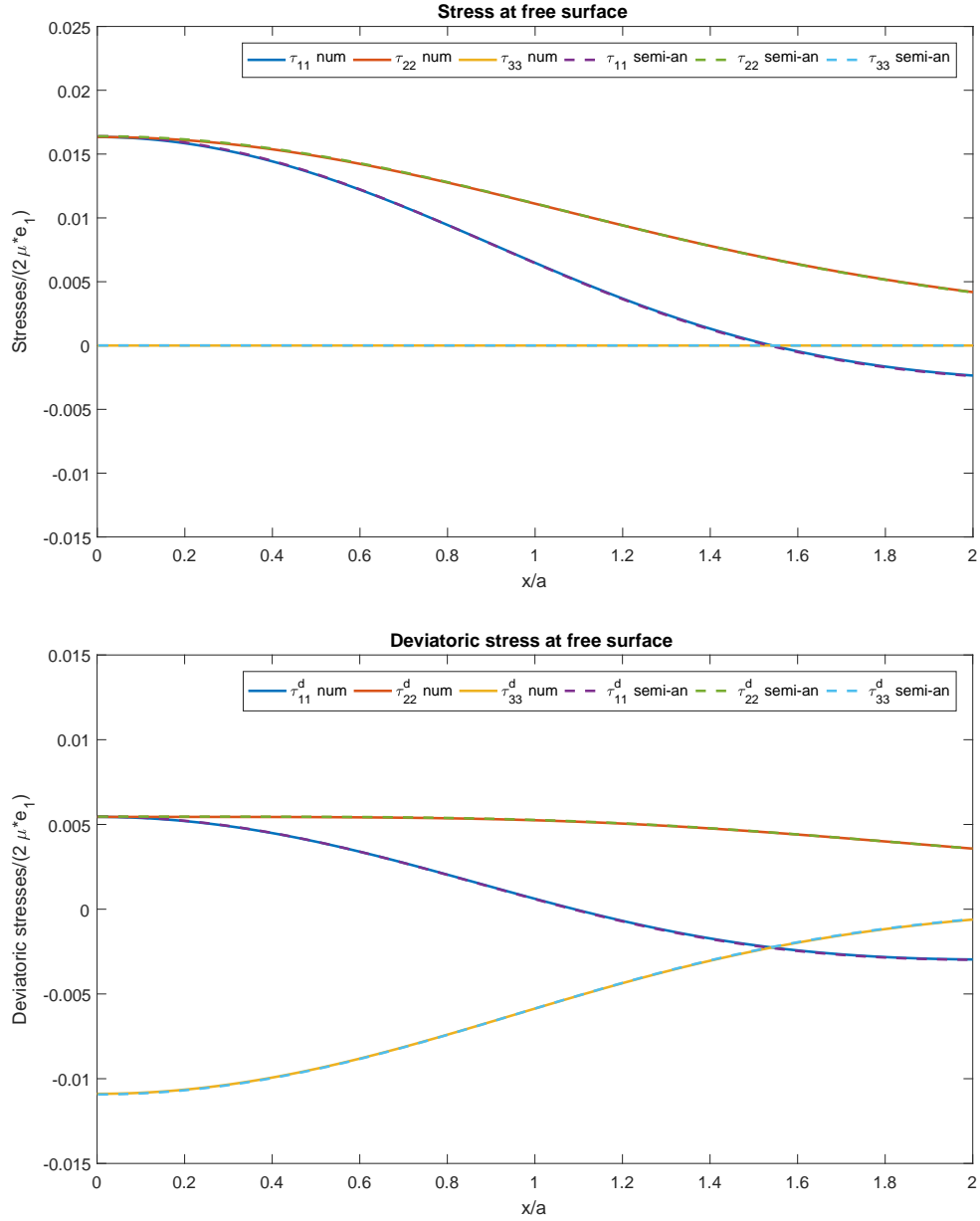
Figure 3.13: Top figure: comparison between the diagonal components of the stress tensor τ_{ij} "num", meaning fully numerical (solid lines), and those obtained through our method τ_{ij} "semi-an", meaning "semi-analytical" (dashed lines), on the free surface, plotted along the x_1-axis. Bottom figure: comparison between the diagonal components of the deviatoric stress tensor τ_{ij}^d "num", meaning fully numerical (solid lines), and those obtained through our method τ_{ij}^d "semi-an" (dashed lines), meaning "semi-analytical", on the median plane of the cylindrical inclusion, plotted along the x_1-axis. In both figures, the x-axis is normalized to the radius $a = 500m$ of the cylinder. The stresses on the y-axis are normalized to $2\mu e_1$, where e_1 is defined in eq. 3.2.8.

Figure 3.14: Comparison between the displacement components u_1, u_2, u_3 "num", meaning fully numerical (solid lines), and those obtained through our method u_1, u_2, u_3 "semi-an", meaning "semi-analytical" (dashed lines), on the free surface, plotted along the x_1-axis. The x-axis is normalized to the radius $a = 500m$ of the cylinder, while the y-axis is normalized to the product Aa, where A is the constant defined in eq. 6.3.8.

The generally good agreement between the two sets constitutes an important validation of our results, as the fully numerical approach works in a completely independent way from the methods we have employed to handle the Mindlin's tensor partial derivatives, from section 3.2 on.

In the next chapter we will compare the displacements and stresses displayed so far to other deformation source models which have been applied to model the ground surface deformation in hydrothermal regions, and especially at Campi Flegrei.

Chapter 4

Discussion

This chapter is devoted to the discussion of the results of our work.

We will draw a comparison between the displacement and stress fields we retrieved at the free surface of the half-space and those produced by some of the most common types of deformation sources employed to model surface ground deformation episodes (see section 1.3.1).

Eventually, we will provide a theoretical validation to the plausibility of our model, on the basis of other works on hydrothermal processes and the considerations made by many authors on the 1982-84 unrest at Campi Flegrei caldera.

4.1 Comparison with other deformation source models

In this section we will consider three different deformation source models, all of which belong to the cathegory of pressurized cavities. They are representative of most of the trials that have been made over time to model the ground displacement pattern in the Campi Flegrei area during the 1982-84 unrest and to propose an originating mechanism for it (e.g. Trasatti et al., 2011, Troise et al., 2018). We will start with the already mentioned Mogi source (subsection 1.3.1), then proceeding with a penny-shaped crack, and ending with an ellipsoid.

The results for the displacement components at the free surface presented here have been obtained through the LibHalfSpace C++ library, created by Ferrari et al. (2016).

Mogi source

The Mogi source (Mogi, 1958) approximates a pressurized spherical cavity embedded in a homogeneous elastic half-space (see fig. 1.4). As reported in section 1.4, this simple source model has been applied to fit the ground uplift at Campi Flegrei by some authors (Berrino et al., 1984, Bonafede et al., 1986), and it manages to reproduce the shape of its pattern (see fig. 1.2).
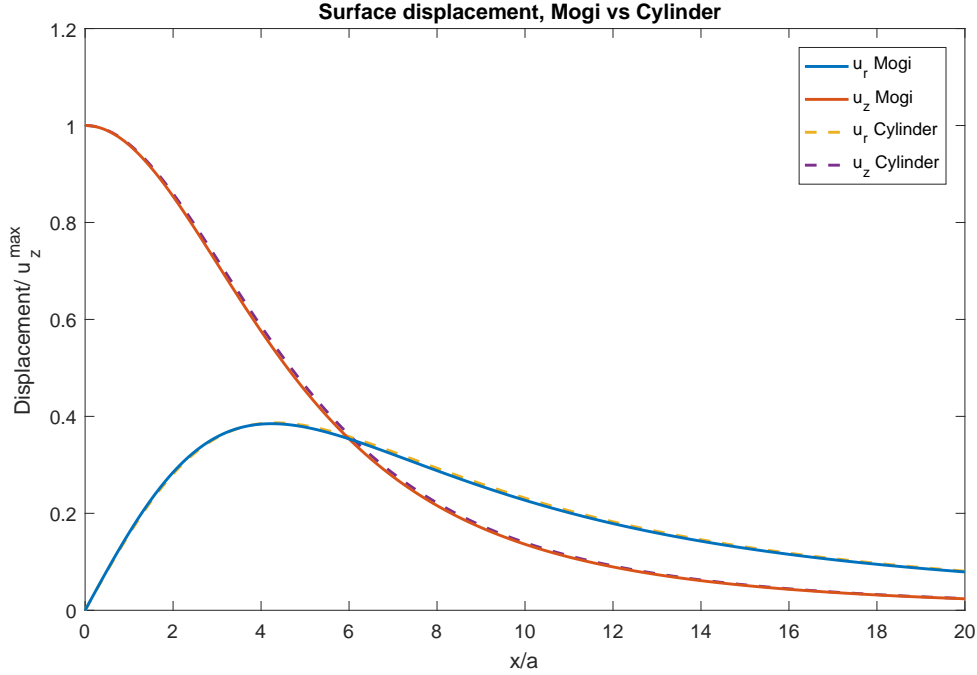
Figure 4.1: Radial displacement (u_r) and vertical uplift ($-u_z$) at free surface for a Mogi source (solid lines) and a cylinder-shaped TPE inclusion (dashed lines), both of which share the same radius $a = 500m$ and depth $c = 3000m$. It is to point out that the radial component is equivalent to the u_1 component we plotted for our source in fig. 3.7, and the uplift $-u_z$ is the same as $-u_3$ in fig. 3.8. The x-axis is normalized to the radius of the sources, while the y-axis is normalized separately to the two maximum values of the vertical uplift for the respective models.

To compare the two models, we choose the same geometric parameters for both the sources: namely, the same radius $a = 500m$ for the cylinder and the sphere, the same depth $c = 3000m$ of the source center.

As we can notice in fig. 4.1, both the radial and the vertical displacement components are practically indistinguishable at the free surface, and both the models succeed in reproducing the bell-shaped, symmetric pattern of the recorded ground uplift between 1982 and 1984. As the Mogi source already managed to fit in good approximation the geodetic data at Campi Flegrei (Bonafede and Ferrari, 2009), the similarity between these results means that the model we considered cannot be ruled out in the first place in the interpretation of the causes of the uplift.

In the case of the Mogi source alone, we also provide comparisons between the diagonal deviatoric stress components of one source and the other. The deviatoric stress field τ_{ij}^d for the Mogi source was not obtained through the LibHalfSpace software, but instead it was derived from the expressions of the displacement components in cylindrical coordinates (r,ϕ,z) provided by Bonafede and Ferrari (2009):

$$u_r = \frac{\Delta P a^3}{4\mu} \left[\frac{r}{R_1^3} + f(r,z) \right] \tag{4.1.1a}$$

$$u_z = \frac{\Delta P a^3}{4\mu} \left[\frac{z-c}{R_1^3} + g(r,z) \right] \tag{4.1.1b}$$

where ΔP is the overpressure of the sphere, a is the radius, c the depth of its center, $z = x_3$ is the vertical coordinate, $r = \sqrt{x_1^2 + x_2^2}$ is the radial one and $R_1 =$

$\sqrt{r^2 + (z-c)^2}$ is the distance of the observation point from the source center itself. Moreover, the functions $f(r,z)$ and $g(r,z)$ are defined as

$$u_r = \left[\left(\frac{3K+7\mu}{3K+\mu} \right) \frac{r}{R_2^3} - \frac{6zr(z+c)}{R_2^5} \right] \tag{4.1.2a}$$

$$u_z = \left[-\left(\frac{3K+7\mu}{3K+\mu} \right) \frac{z+c}{R_2^3} + \frac{2z}{R_2^3} - \frac{6z(z+c)^2}{R_2^5} \right] \tag{4.1.2b}$$

where K is the bulk modulus and $R_2 = \sqrt{r^2 + (z+c)^2}$ is the distance between the observing point and the center of the mirror source (details can be found in the original paper, Mogi, 1958). These expressions hold true in the point-source approximation ($a << c$).

The stress field is purely deviatoric around the spherical cavity, and it can be obtained through the elastic constitutive relation $\tau_{ij}^d = 2\mu e_{ij}^d$, where $e_{ij}^d = e_{ij}$ is defined in eq. 2.1.1.
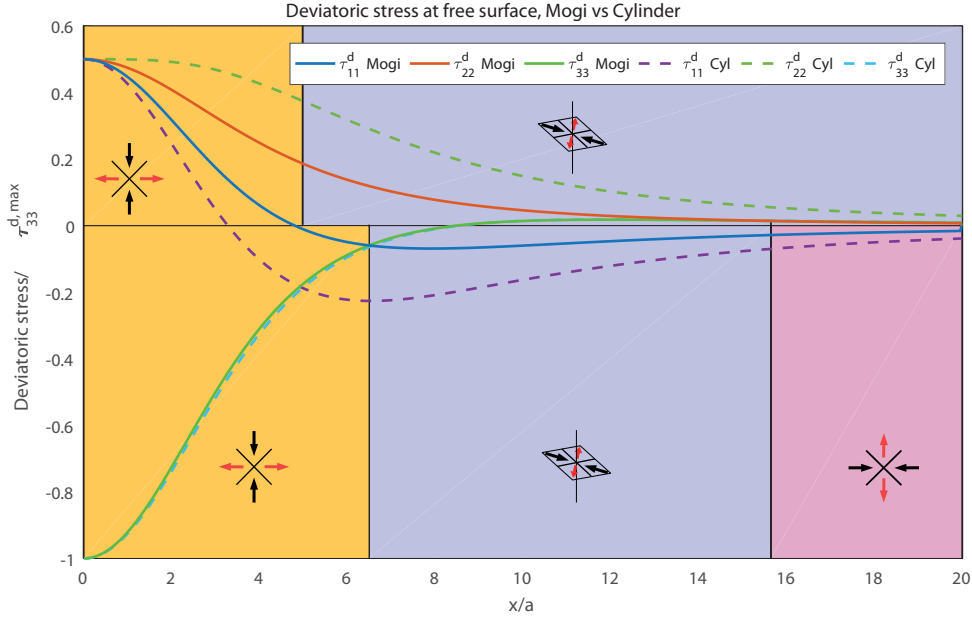
Figure 4.2: Diagonal components of deviatoric stress tensor at free surface ($x_3 = 0m$) for the Mogi source (solid lines) and the TPE source (dashed lines). The x-axis is normalized to the radius of the sources, while the y-axis is normalized separately to the two maximum values of τ_{33}^d for the respective models. The coloured domains in the upper half of the plot mark the different stress environments of the TPE source, while those in the lower half mark those of the Mogi source. The orange domain corresponds to a distensive environment, the blue domain corresponds to a strike-slip environment, and the violet domain represents a compressive environment. Each colour is associated to a symbol, marking the same stress regime.

The diagonal components of the deviatoric stress tensor for both sources on the free surface are reported in fig. 4.2. It can be noticed that their trends are similar, and τ_{33}^d is practically identical for both the sources, even if the amplitudes of τ_{11}^d and τ_{22}^d for the Mogi source are smaller than those of the TPE source.

Interesting information is provided by the analysis of the stress environments. From the origin to around five times the radius of the sources, there is a distensive environment for both the sphere and the cylinder (orange domain in the plot), in that

the most compressive stress is τ_{33}^d, the most tensile one is τ_{22}^d and the intermediate one is τ_{11}^d. However, the point where the most compressive and the intermediate stress invert their order is closer to the origin for the TPE source than for the Mogi source. This means that the extensive regime prolongs further away from the origin in the second case, and after that, both the sources are associated with a strike-slip environment (blue domain), where τ_{11}^d is the most compressive stress and τ_{33}^d is the intermediate one.

Another difference comes from the fact that for the Mogi source there is a further inversion in the order of stresses, where τ_{33}^d becomes the most tensile one, leading to a compressive environment, even if the transition is barely noticeable in the plot (violet domain).
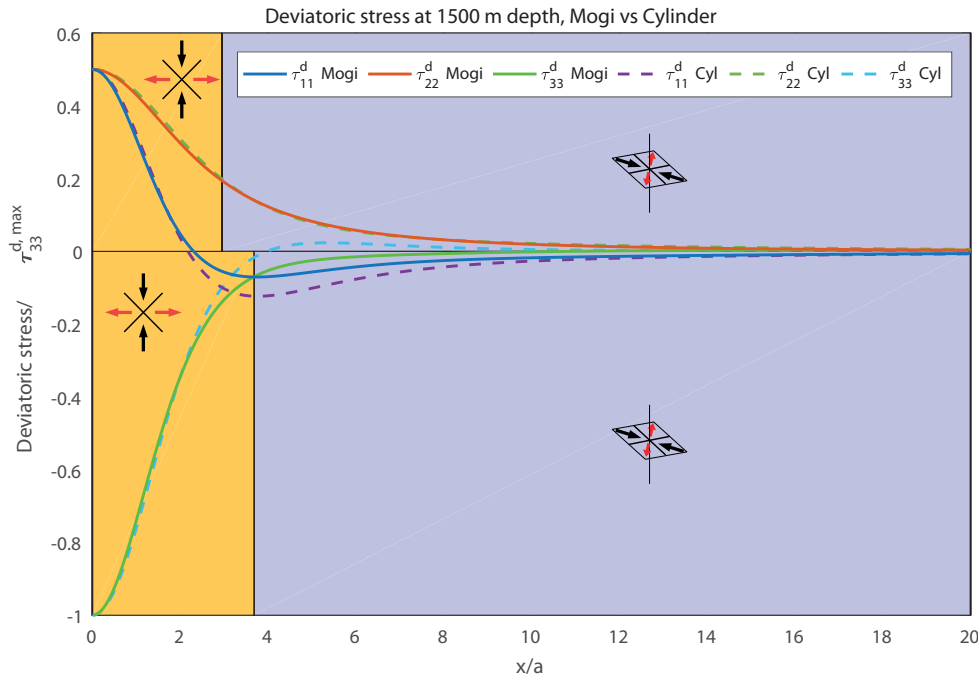
Figure 4.3: Diagonal components of deviatoric stress tensor at $x_3 = 1500m$ for the Mogi source (solid lines) and the TPE source (dashed lines). The x-axis is normalized to the radius of the sources, while the y-axis is normalized separately to the two maximum values of τ_{33}^d for the respective models. The coloured domains in the upper half of the plot mark the different stress environments of the TPE source, while those in the lower half mark those of the Mogi source. The orange domain corresponds to a distensive environment, the blue domain corresponds to a strike-slip environment, and the violet domain represents a compressive environment. Each colour is associated to to a symbol, marking the same stress regime.

The plot in fig. 4.3 compares the deviatoric stress components for both sources at 1500 m depth, which is halfway the depth of their centers. This time the trends are even closer, and the differences in the amplitudes of τ_{11}^d and τ_{22}^d are less pronounced. More importantly, the distensive environment (orange domain) associated to the Mogi source extends less beyond that of the TPE source, and both domains end within four times the radius of the sources from the origin. After that, both models are associated with a common strike-slip environment (blue domain).
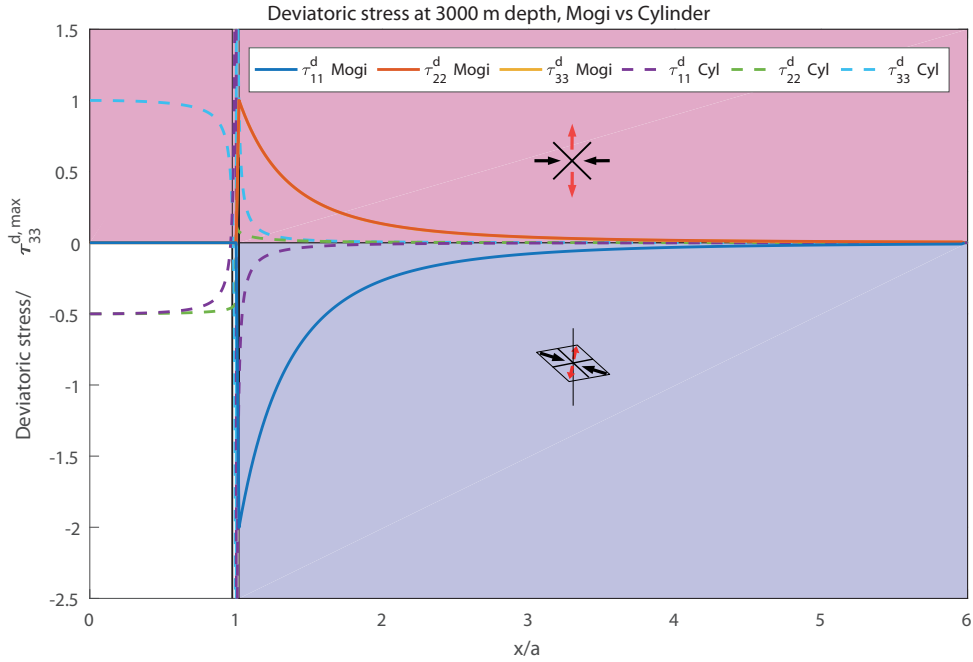
Figure 4.4: Diagonal components of deviatoric stress tensor at $x_3 = 3000m$ for the Mogi source (solid lines) and the TPE source (dashed lines). This depth coincides with that of the median plane of our source. The x-axis is normalized to the radius of the sources, while the y-axis is normalized separately to the two maximum values of τ_{33}^d for the respective models. The coloured domains in the upper half of the plot mark the different stress environments of the TPE source, while those in the lower half mark those of the Mogi source. The violet domain represents a compressive environment, while the blue domain corresponds to a strike-slip environment. Each colour corresponds to a symbol, marking the same stress regime. As the deviatoric stresses vanish within the Mogi source, there is no colour associated to that portion of the plot.

Finally, the plot in fig. 4.4 compares the deviatoric stress components for both sources at 3000 m depth, right on their median planes. Here we can observe some major differences. The deviatoric stresses vanish within the Mogi source region, as it represents a chamber filled with magma. The stress regime within the TPE source, instead, is compressive (violet domain), as we already pointed out in section 3.4 (cfr. fig. 3.6 a). Outside the sources, the stress environment is still compressive in our case, even if τ_{22}^d and τ_{11}^d switch places as, respectively, the most compressive stress and the intermediate one. The Mogi source, on the contrary, is associated with a strike-slip environment (blue domain), τ_{33}^d being the intermediate stress, although it is barely distinguishable from the most tensile one, τ_{22}^d.

In conclusion, both the Mogi and the TPE source show very similar trends of the displacement components at the free surface, and generally comparable trends of the deviatoric stress components at different depths. Moreover, they both give rise to a distensive stress environment centered around their symmetry axis (namely, the vertical axis x_3). The lateral extension of this domain reduces progressively with depth, suggesting that it may extend over a truncated cone in the 3D half-space. The main difference, however, is the presence of a compressive environment, which could account for reverse fault mechanisms even beneath the center of the area of maximum uplift, in the case of the TPE source, while the Mogi source is incompatible with such a regime, at least in its surroundings. For this reason, our model is more suitable than the other to describe a heterogeneous distibution of focal mechanisms like that retrieved from the seismic data sets of the 1982-84 unrest at

Campi Flegrei (subsection 1.3.2, fig. 1.6).

Another advantage of our model with respect to the Mogi source is that in the latter we would need an overpressure ΔP of about 1 GPa to account for vertical surface displacements of the same order of magnitude of those recorded at Campi Flegrei ($\approx 1m$), while in our model a pore pressure increase Δp of only 10 MPa is sufficient. The overpressure needed in the Mogi model (a value of 690 MPa was estimated by Bonafede and Ferrari (2009) for the 1982-84 uplift case) would be unacceptable if the medium surrounding the source is to remain in the elastic regime, as the tensile strength of crustal rocks is less than a few tens of MPa (Brace and Kohlstedt, 1980), while the pore pressure increase we chose in our case is of a more reasonable magnitude.

Fialko source

The source model proposed by Fialko et al. (2001) consists of a horizontal circular crack in a semi-infinite elastic solid, and it is used to describe the displacement field at the free surface due to sill-like magma intrusions. This kind of deformation source includes the penny-shaped crack advocated by some authors (Battaglia et al., 2006, Amoruso et al., 2008, Trasatti et al., 2011) to account for the 1982-84 uplift.
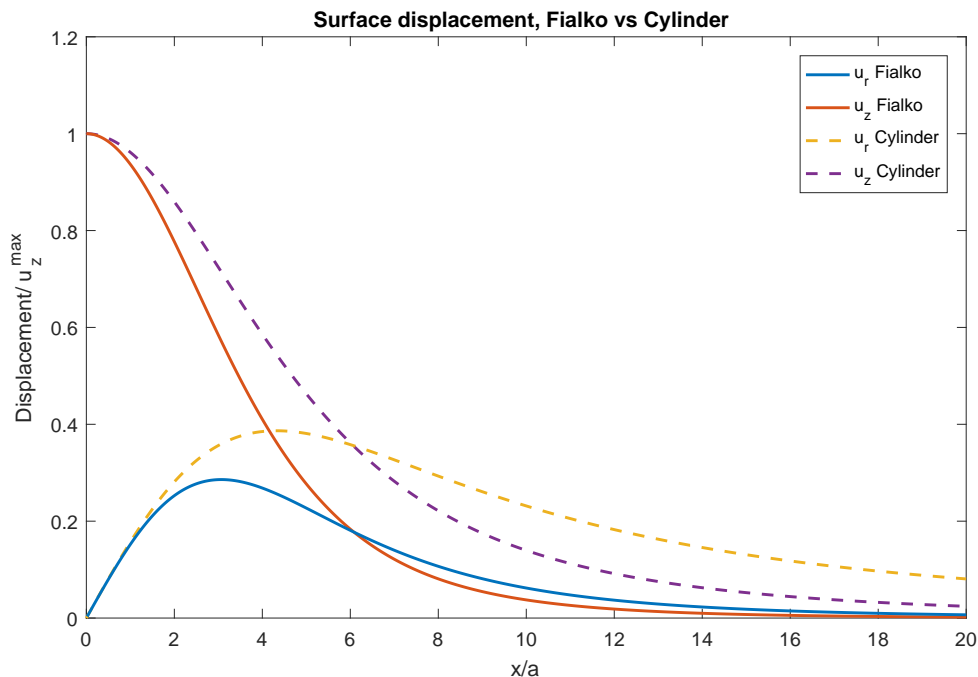
Figure 4.5: Radial displacement(u_r) and vertical uplift ($-u_z$) at free surface for a Fialko source (solid lines) and a cylinder-shaped TPE inclusion (dashed lines), both of which share the same radius $a = 500m$ and depth $c = 3000m$. It is to point out that the radial component is equivalent to the u_1 component we plotted for our source in fig. 3.7, and the uplift $-u_z$ is the same as $-u_3$ in fig. 3.8. The x-axis is normalized to the radius of the sources, while the y-axis is normalized separately to the two maximum values of the vertical uplift for the respective models.

The radial component of displacement and the vertical uplift obtained through our model are compared to the respective components obtained by assuming a Fialko source at the same depth ($c = 3000m$) in fig. 4.5. The radius of the Fialko crack is the same as that of the TPE source: $a = 500m$. As we can see in the plot, the displacement components show similar trends, but the maximum horizontal

78

displacement in the case of the TPE source occurs farther from the origin than in the case of the Fialko source. Furthermore, the amplitudes of both the components for our source decrease more slowly away from the origin with respect to those for the Fialko source, this meaning that the TPE model may be better suited to describe situations where the horizontal deformation is not negligible even at considerable distances from the center of the area of maximum uplift.

Yang source

Finally we consider one last model, which is the Yang source (Yang et al., 1988). It consists of a dipping prolate spheroid, with axes a, b, c' (the last is not to be confused with the depth $c = 3000m$, common to both models). LibHalfSpace allows the user to set the length of the first two ($a > b$) together with the angles of their orientation ϕ and θ, while the length of the third axis is evaluated as $c' = \sqrt{a^2 - b^2}$. In our simulation we choose $a = 600m$ and $b = 300m$ to make them comparable to the radius $a = 500m$ of the TPE source, while the angles were set to zero to make the spheroid lie on a horizontal plane at depth c.
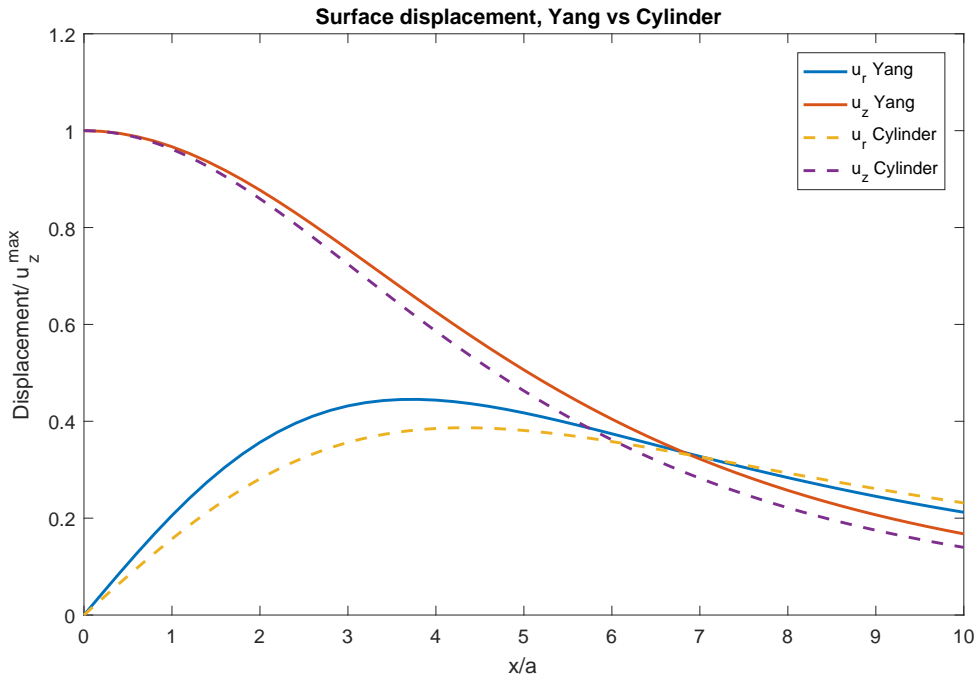
Figure 4.6: Radial displacement(u_r) and vertical uplift ($-u_z$) at free surface for a Yang source (solid lines) and a cylinder-shaped TPE inclusion (dashed lines), both of which share the same depth $c = 3000m$, while the length of the axis of the Yang source ($a = 600m$, $b = 300m$, $c = \sqrt{a^2 - b^2}$) are chosen to be comparable to the radius of the TPE source ($a = 500m$). It is to point out that the radial component is equivalent to the u_1 component we plotted for our source in fig. 3.7, and the uplift $-u_z$ is the same as $-u_3$ in fig. 3.8. The x-axis is normalized to the radius of the sources, while the y-axis is normalized separately to the two maximum values of the vertical uplift for the respective models.

The comparison between the radial and vertical components of displacement at the free surface for the two models is displayed in fig. 4.6. Also in this case they show similar trends, the differences in amplitude being less pronounced than in the Fialko source case. It is possible to notice that even here, the maximum horizontal displacement in the case of the TPE source occurs slightly farther from the origin

than in the case of the Yang source.

The conclusion we can draw from the comparisons we made so far is that the results of our model at the free surface do not differ radically from those provided by other models involving pressurized cavities with the same dimensions and in the same context, although the stress field at the depth of the source shows considerable difference with respect to the Mogi sphere. Thereby, we cannot rule out its applicability in practical situations where even simple models like the Mogi source are able to reproduce some of the features of the phenomenon we are studying, as in the case of the Campi Flegrei 1982-84 bradyseism.

4.2   Possible applications of our model

The aim of this section will be to discuss how the model we first introduced in section 1.4 may fit into the description of the features and dynamics involving hydrothermal regions such as Campi Flegrei.

First, let us recall the characteristics of our deformation source model (fig. 3.1): a cylindrical thermo-poro-elastic region affected by a sudden increase in temperature ΔT and pore pressure Δp, embedded in a poro-elastic material which extends over a space bounded by a free surface. The horizontal dimensions of the source are wider than its height but smaller than the depth of its median plane.
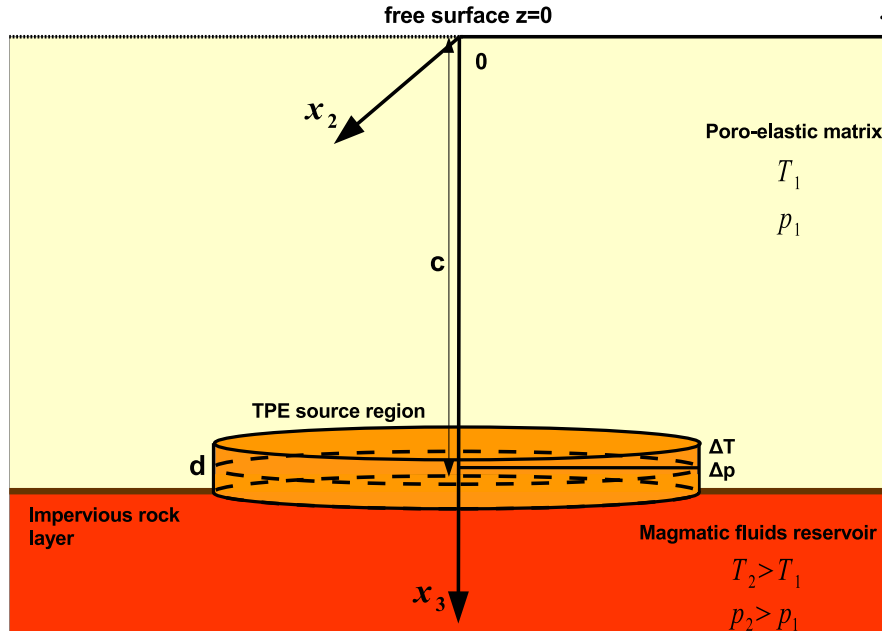
Figure 4.7: Interpretation of the TPE inclusion as a thin cylindrical layer of thermo-poro-elastic material in direct contact with an underlying reservoir of magmatic fluids at temperature T_2, highlighted in dark orange, and embedded in an overlying layer of poro-elastic material at temperature $T_1 < T_2$ (which represents the medium outside the TPE inclusion in our model), highlighted in pale yellow. The two domains are separated by a boundary of low-permeability rocks; fluids in the reservoir are pressurized at lithostatic values (p_2), while the pore pressure in the upper layer is hydrostatic (p_1). A breach in the impervious layer beneath the inclusion makes it possible for the magmatic fluids to be injected into it, causing a sudden increase in temperature ΔT and pore pressure Δp within it, and inducing deformation and stresses both inside and in the surrounding medium.

We remind that as we imposed drained conditions on the poro-elastic half-space (section 2.4), the pore pressure change outside the inclusion is expected to be zero immediately after the TPE source has undergone the changes in p and T. The pore pressure changes in a poro-elastic medium are independent of the deviatoric strain tensor (section 2.3), and we have seen that e_{ij} is purely deviatoric outside the inclusion (sections 3.2.1 and 3.4), therefore the stress field induced there does not lead to any change in p, and Δp remains non-vanishing only within the TPE source. However, given the fact that both the material inside the inclusion and the surrounding medium are permeable, and that we did not introduce any impervious layer around the surface of the inclusion which could isolate it from the outside, there is no obvious reason why the thermal and pressure increases should not diffuse over

the rest of the half-space. As a consequence, we need to verify on which timescales this assumption holds true.

Here we propose a new interpretation of the TPE source as a thin layer of thermo-poro-elastic material in contact with an underlying reservoir of hot and pressurized magmatic fluids, as it is shown in fig. 4.7.

At first, the TPE region is part of the shallow poro-elastic layer, sharing its same values of T and p. If failures in the impervious boundary allow the underlying fluids to migrate into the inclusion, then the consequence is a sudden increase in temperature and pore pressure: $\Delta T \approx T_2 - T_1$ and $\Delta p \approx p_2 - p_1$, which at first can be assumed to be confined to the immediate surroundings of the breach points (which are represented by the inclusion itself). These changes are sufficient to trigger deformation and stress fields both within the volume of the inclusion and the rest of the shallow poro-elastic layer (pale yellow domain in fig. 4.7), as we have explained in the previous chapters.

In time, it is reasonable to expect the changes in temperature and pore pressure to gradually diffuse upward and affect the whole poro-elastic matrix. The question to answer, therefore, is under which conditions we can effectively neglect their diffusion, and consider them homogeneous and confined in a small region of the half-space. In order to understand this, we need to confront ourselves with a model that has been developed by Zencher et al. (2006) to describe the migration of lithostatically-pressured magmatic fluids into shallow hydrostatic reservoirs, as illustrated in fig. 4.8.
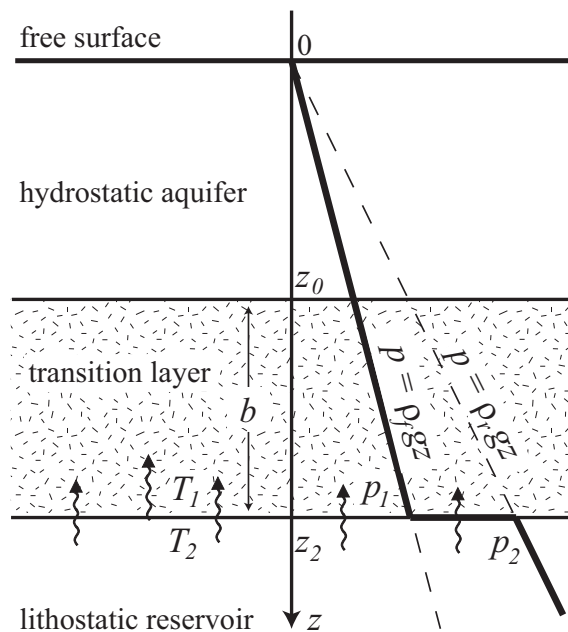
Figure 4.8: Schematic diagram of the model employed by Zencher et al. (2006): the layer $z_0 < z < z_2$ is a fluid-saturated porous medium. In $z = z_0$ a meteoric aquifer is present at $T = T_1$ and at the hydrostatic pressure $p_1 = \rho_f g z_0$; in $z = z_2$ the layer is in contact with a hot fluid reservoir at lithostatic pressure $p_2 = \rho_r g z_2$ and at temperature T_2. ρ_f and ρ_r are respectively the densities of fluids and rocks (after Zencher et al., 2006).

In this model, a transition layer is assumed to separate the shallow hydrostatic reservoir from the deep lithostatic one. An impervious boundary further separates the bottom of the transition layer from the underlying lithostatic reservoir, and it breaks down at a certain instant. As a consequence, hot and overpressurized fluids start to migrate into the shallow aquifer, and the rate at which the induced changes in T and p diffuse over it depends on the permeability k of its rocks (see the Appendix, section 6.1). In this frame, our TPE source region would be located at the bottom of the transition layer. However, it is to say that the model by Zencher et al. (2006) assumes stationary volume flow rates of fluids at the bottom of the transition layer.

Figure 4.9: A more detailed diagram of the two-reservoir model with a transition layer ($d_2 < z < d_1$). On the x-axis, the nondimensional quantity $p^* = \frac{p'}{\Delta p'}$ is the ratio between the pore pressure p' in excess with respect to the hydrostatic gradient and the difference $\Delta p'$ between lithostatic and hydrostatic pressure at a given depth. In the right side of the picture, different pressure gradients with respect to depth z are reported together with the hydrostatic gradient (along the z-axis) and the near-lithostatic one (the area shaded in gray). They depend on the volume flow rate of fluids through the material Q_0^* normalized to the equilibrium flow rate in the steady-state regime, and they refer to the final stationary configuration. The boundary conditions require p^* to vanish at the top of the transition layer. $\Delta\sigma^*$ is the deviatoric stress in the region normalized to $\Delta p'$ (Stefansson et al., 2011).

The permeability of the rocks can change according to pressure increase, which can lead to failures in the elastic matrix, thus creating more fractures and allowing for an increase in the flux of fluids through the pore network. This is actually what happens at the beginning, when the injection of lithostatically-pressured fluids through a breach in the impervious boundary causes a sudden increase in the local permeability, thus allowing the pore pressure change to diffuse so rapidly within the surroundings of the breach point that the situation can be approximated to a

sudden jump in p over a small region immediately above $z = z_2$ (see fig. 4.8). An equally sudden jump in T can be assumed as well, as the layer in which fluids are first injected is so thin that the heat transfer through advection happens on very short timescales.

Moreover, the viscosity η of the hot fluids from the lithostatic reservoir is expected to be smaller than that of the fluids in the hydrostatic one. According to the Darcy's law (see the Appendix, section 6.1, for a brief explanation), small viscosities allow for high volume flow rates of fluid even if the pressure gradients involved are not too big, and the permeability of the material is low. This would make the transition to the configuration where Δp and ΔT are non-vanishing and homogeneous within a small region at the bottom of the transition layer even more rapid, providing a further motivation to the sudden temperature and pore pressure jump.

A detailed plot of the pressure as a function of depth within the transition layer is shown in fig. 4.9, which is drawn from a work by Stefansson et al. (2011) where an equivalent model was considered. The pressure profiles reported there depend on the normalized volume flow rate Q_0^* of the fluids injected from the lithostatic reservoir. It can be noticed that, for high values of Q_0^*, the pressure through the lower part of the layer tends to the lithostatic profile. We assume our source region to coincide with a thin layer at the bottom of the transition one, where, if Q_0^* is big enough, the depth dependence of the pore pressure excess with respect to the hydrostatic value could be approximated by a step function, corresponding to the Δp localization within the TPE source.
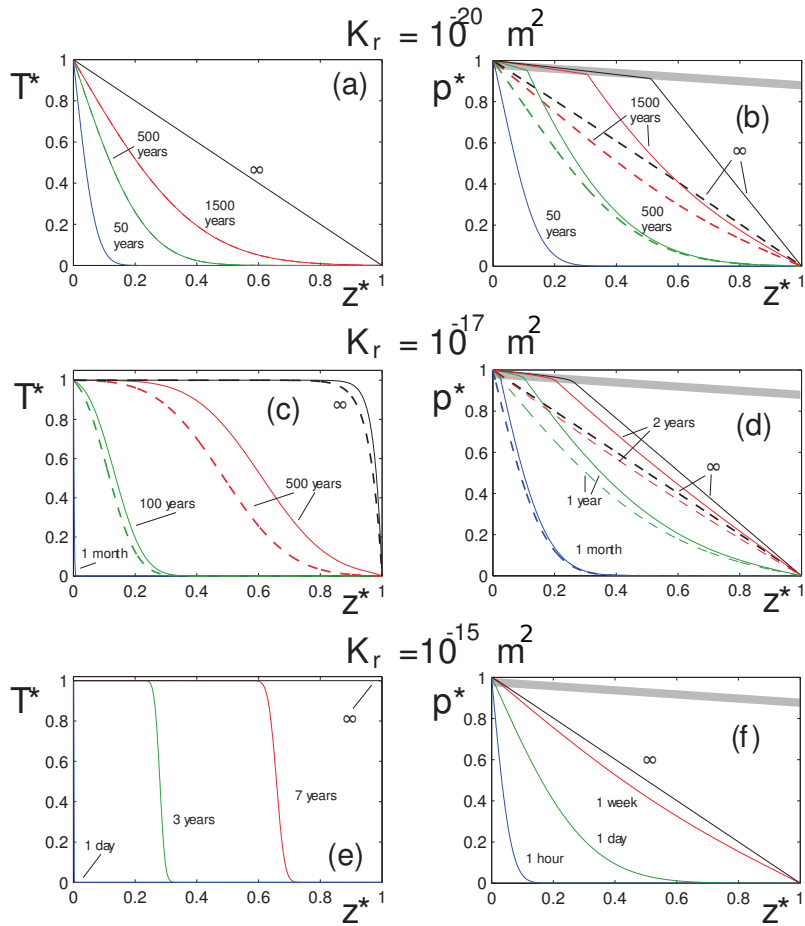
Figure 4.10: Solutions for temperature and pressure migration from the lithostatic reservoir through a 1-km thick transition layer with a constant initial temperature and hydrostatic pressure, assuming a stationary flux of fluids injected from the lithostatic reservoir. The x-axis represents the normalized vertical axis $z^* = \frac{z-z_2}{b}$, where b is the thickness of the transition layer, and $z^* = 0$ marks its bottom. p^* is defined as in fig. 4.9, while $T^* = \frac{T-T_1}{T_2-T_1}$ (see fig. 4.8). Different profiles correspond to different times from the first injection. The value of the intrinsic permeability (K_r in the plots) of the rocks is $k = 10^{-20}m^2$ in fig. a) and b); $k = 10^{-17}m^2$ in fig. c) and d) and $k = 10^{-15}m^2$ in fig. e) and f). Dashed lines show the solutions if the permeability is not pressure-dependent, and the near-lithostatic domain in the plots relative to the pore pressure is shaded in gray (after Zencher et al., 2006).

The assumption that ΔT remains confined within the source region is supported by the timescales of temperature migration, which can be seen in fig. 4.10. If the permeability is low (fig. 4.10 a), most of the heat transfer through the transition layer is ascribed to conductive processes, and it takes decades for the temperature change to diffuse over its lower part. If the permeability is higher (fig. 4.10 c, e), then the advection starts contributing as well, and temperature changes migrate on shorter timescales. In these cases, the temperature profile near the bottom of the transition layer (where our source region is supposed to be) approximates a step function for very short timescales (1 month if $k = 10^{-17}m^2$), and so we can assume a sudden jump in T within the TPE source immediately after the injection of fluids. We can also expect this change in T to take several months to diffuse over the rest of the layer even if high permeability values ($k = 10^{-15}m^2$) are considered (fig. 4.10 e).

While it is safe to assume Δp to be non-vanishing only within the TPE source immediately after the fluids injection, we cannot make the same assumption later in

time. Nevertheless, we can assume that the pore pressure change outside the TPE region are negligible only for short timescales (less than a month if $k = 10^{-17}m^2$, fig. 4.10 d).

Going back to the Campi Flegrei caldera, the estimated values of permeability as a function of depth are reported in the work of Troise et al. (2018). In fig. 4.11 we can see that at 3 km depth, where we placed the TPE inclusion, $k \approx 10^{-15}m^2$, and this would suggest a pore pressure migration timescale similar to that in fig. 4.10 f). If that is the case, the assumption of Δp being confined within the inclusion for more than few days would be unrealistic. If we set the source depth to 8 km, then we could assume $k \approx 10^{-17}m^2$, and the situation would be similar to that in fig. 4.10 d), with longer timescales needed for the migration of p.
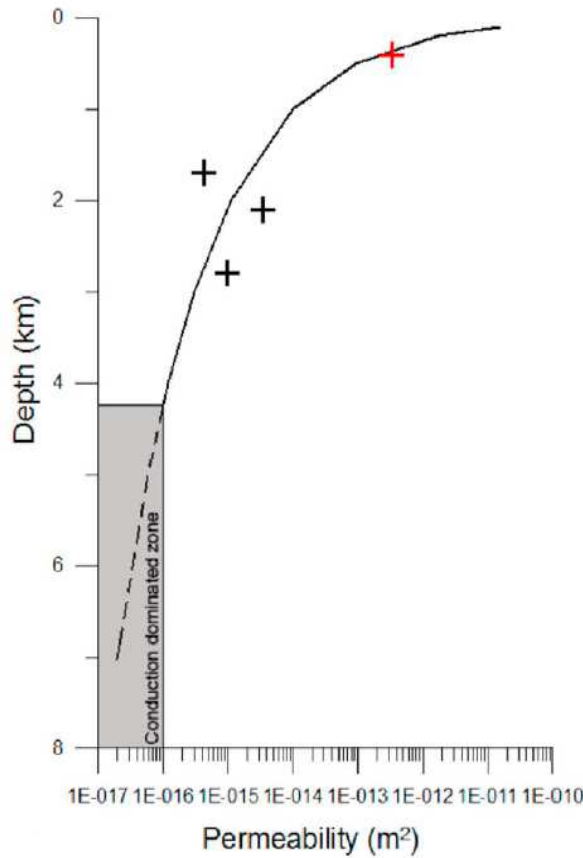
Figure 4.11: Plot of the theoretical permeability as a function of depth in the Campi Flegrei area. The best curve has been obtained by interpolating permeability data (shown by crosses) at different depths. Permeability values that can be inferred at 3 km depth, where we have located the median plane of the TPE inclusion, are $k \approx 10^{-15}m^2$ (after Troise et al., 2018).

4.2.1 Applicability to the Campi Flegrei region

The case study we chose to compare our results to is that of the Campi Flegrei caldera. The main points we have highlighted in chapter 1 about the characteristics and dynamics of the region are here summarized:

- The caldera has undergone several cycles of inflation and deflation which have hardly ever preceeded a magmatic eruption, at least since the last major eruptive phase which ended around 3800 years BP. This can be interpreted as

the fact that hydrothermal processes may play an important role as well as magmatism, as suggested by D'Auria et al. (2015) and Chiodini et al. (2017).

- The spatial pattern of deformation, which shows an approximate bell-shaped symmetry in the vertical component (fig. 1.2), has remained remarkably unchanged during the last five decades (Troise et al., 2018), and the hypocenters of the earthquakes recorded during the 1982-84 episode are localized in two main clusters around the town of Pozzuoli, and at a depth generally above 5 km (D'Auria et al., 2014).

- Two-reservoir hydrothermal models have been proposed to account for the cycles of inflation and deflation, on the bases of the periodic injection of lithostatically-pressurized fluids of magmatic origin into a shallow hydrostatic aquifer (Lima et al., 2009).

- Focal mechanisms retrieved from seismic data sets are very heterogeneously distributed among normal, compressive and strike-slip types, even if the local tectonic environment is dominated by a regional distensive component (D'Auria et al., 2014).

According to these points, a further consideration can be made about our model. With reference to fig. 4.7, the deep reservoir can be seen as a degassing magma chamber, with the TPE inclusion lying above it: if that is the case, then the boundary conditions would require vanishing shear stresses on the bottom base of the cylindrical source, and they are in fact verified by our model, as τ_{ij}, $i \neq j$ vanish on both the bases of the cylinder (see sections 3.4 and 6.3). However, as we reported at the end of section 1.2, large magma bodies are supposed to exist beneath the Campi Flegrei region only at depths of about 8 km, so we would need to change the depth of our source.

Alternatively, the deep lithostatic reservoir can be interpreted as a deep permeable region where fluids of magmatic origin (e. g. supercritical water and CO_2) are stored and separated from the upper region by a low-permeability boundary. This is similar to the two-reservoir model proposed in the work of Lima et al. (2009), mentioned in subsection 1.3.2, where the estimated depth for the impervious boundary dividing the two reservoirs was 3 km.

We conclude with a final remark on the TPE inclusion itself. According to the work of Trasatti et al. (2011) (see also section 1.3.1), the most likely deformation source model for the Campi Flegrei 1982-84 unrest is a mixed mode (shear and tensile) dislocation at 5.5 km depth, through which a magma dike could have ascended. The results of the stress field of our model reported in section 3.4 suggest a compressive stress regime within the source region (see fig. 3.6), which would be compatible with the propagation of a magma dike accompanied by reverse-shear slip. The overall displacement field is caused by both a magmatic source and a hydrothermal source; however, our model would account only for the ground displacement due to the latter one.

Chapter 5

Conclusive remarks

In this work, we considered a cylinder-shaped thermo-poro-elastic inclusion of radius $a = 500m$ embedded in a poro-elastic semi-infinite solid bounded by a free surface, the depth of the inclusion being $c = 3000m$, and we evaluated the displacement and stress fields both within the half-space and the inclusion itself. The values of the elastic parameters we chose for the medium of the solid and the inclusion are summarized in section 3.1.

In order to achieve this aim, we availed ourselves of the Eshelby's method, a technique which applies to cases where a limited region of a homogeneous space undergoes a transformation that would result in changes of volume and shape, but instead, as this region is constrained by the surrounding medium, gives rise to displacement and stress fields both inside and outside of it (section 2.1). We also made use of the elastic Green's function for a half-space, here referred to as the Mindlin's tensor, which was derived by the work of Mindlin (1936) (subsection 2.5, see also the Appendix 6.2).

The components u_i of the displacement field in cartesian coordinates x_1, x_2, x_3 were computed in a semi-analytical way in chapter 3 and compared with results obtained for the same source located within an homogeneous and unlimited elastic medium by Lamberti (2017). The reference frame used throughout the work is explained in fig. 3.2 b).

The expressions for the displacement components are reported in eqs. 3.3.19a - 3.3.19c. The results for the displacement field on the median plane of the cylindrical inclusion ($x_3 = c$) are illustrated in fig. 3.3 and fig. 3.4, whereas those at the free surface ($x_3 = 0$) are displayed in fig. 3.7 and fig. 3.8.

The expressions for the total and deviatoric stress tensor components, both within and outside the source region, were also obtained. They are reported in eqs. 3.4.17a - 3.4.18b. The results for the stress field on the median plane of the source region are shown in fig. 3.5 and fig. 3.6, while those at the free surface are reported in fig. 3.9 and fig. 3.10.

The model we developed was intended to be applied to the description of surface ground deformation in hydrothermal regions, and the case study we focused our attention on is the 1982-84 unrest episode at Campi Flegrei caldera. The first chapter (1) of this work contains the introduction of this well-known and studied volcanic area, eventually reviewing the deformation source models that have been employed to reproduce the geodetic data over the years (subsection 1.3.1).

The fact that we consider a sudden and homogeneous change in temperature and pore pressure within the whole TPE inclusion is justified by the results of Zencher et al. (2006) (section 4.2). However, the same work shows that the pore pressure change diffuses over the rest of the half-space in a matter of months if the values of permeability are bigger than $k = 10^{-17} m^2$ (see fig. 4.10), making the assumption of Δp being confined to the inclusion within one month realistic for permeability values of the same order as those estimated for the 3-8 km depth range at Campi Flegrei (see fig. 4.11). The same assumption holds true for ΔT as well, as the timescales necessary to its migration are in the order of years even for high values of k (fig. 4.10 e).

The results we obtained at the free surface (section 3.5) are generally in agreement with those of other models that have been employed in similar situations (section 4.1). The displacements at free surface are in good agreement with those of a Mogi source (fig. 4.1), while there are some differences with respect to the other two source models we considered (fig. 4.5 and fig. 4.6), in that, in our case, the amplitudes of the displacement components decrease more slowly with the distance from the point of maximum uplift.

The stress field retrieved for a Mogi source near the surface (fig. 4.2 and fig. 4.4) shows some differences with respect to that obtained through our model, even if they both suggest a distensive environment in the region above the deformation source, and a strike-slip environment outside. The two stress fields differ considerably at the depth of the sources, in that our model predicts a compressive environment, while the Mogi model does not. Besides, the main advantage over the Mogi model is that the pore pressure change Δp needed to reproduce ground displacements of ≈ 1 m is smaller by at least one order of magnitude than the overpressure ΔP needed in the case of a pressurized sphere.

With regards to the 1982-84 bradyseism at Campi Flegrei, the fact that the stress field we retrieved within the TPE inclusion (fig. 3.5 and fig. 3.6) suggests a compressive environment could account for the inverse focal mechanisms that have been observed, among others, in the area affected by the unrest. The stress regime inside the inclusion is also compatible with the source model proposed by Trasatti et al. (2011), consisting of a tensile dislocation with a reverse-slip component hosting a magmatic intrusion. This suggests that the 1982-84 unrest could be ascribed to the combined effects of both the emplacement of a magma body (the dike) at shallow depths and hydrothermal processes (the TPE inclusion), even if our model describes only the effects of the latters.

Further developments of this model could also take into account the heterogeneity of the poro-elastic half-space, attempting at simulating the observed stratigraphy at Campi Flegrei or in other volcanic areas. To this aim, the representation of the displacement field through eq. 2.2.4 can be made through a numerical approach assuming a distribution of single forces normal to the surface of the inclusion and the Green functions in a layered elastic half-space. The present thesis has allowed this implementation to be tested in the case of an homogenous half space (section 3.6), showing generally good agreement with our results. Moreover, in order to reproduce the temporal dependence of an unrest process, it might be necessary to model the progressive migration of the initial changes in temperature and pore pressure that could affect a wider region, starting from the small inclusion considered here.

We then conclude remarking that such analytical or semi-analytical models as those we considered, even if their nature and the assumptions from which they start are simple, are still of fundamental importance when it comes to calibrate and assess the validity of other, more complex, numerical models.

Acknowledgments

Chapter 6

Appendix

6.1 Darcy's law

In this section we briefly explain the Darcy's law we mentioned in section 2.3. This law, which applies to poro-elastic media filled with fluids, describes the volume flow rate Q of a fluid with viscosity η through a unit surface of a medium with permeability k as

$$Q = -\frac{k}{\eta}\nabla p'$$ (6.1.1)

where $\nabla p'$ is the gradient of p', that is the pressure in excess with respect to the hydrostatic gradient. It is to say that this form of Darcy's law holds true for an incompressible fluid.

The dimensions of the permeability k are m^2, and its values extend over a wide range of orders of magnitude, spanning from $k = 10^{-7} m^2$ for permeable rocks such as sand and coarse sediments, to $k = 10^{-20} m^2$ for magmatic rocks such as basalt.

6.2 Mindlin's tensor components

Here we report the nine components of the Mindlin's tensor in cartesian coordinates, as derived in section 2.5:

$$G_{11} = C\left\{\frac{(3-4\nu)}{R_1} + \frac{1}{R_2} + \frac{(x_1-x_1')^2}{R_1^3} + \frac{(3-4\nu)(x_1-x_1')^2}{R_2^3} + \frac{2x_3x_3'}{R_2^3}\left[1 - \frac{3(x_1-x_1')^2}{R_2^2}\right]\right.$$
$$\left. + \frac{4(1-\nu)(1-2\nu)}{R_2+x_3+x_3'}\left[1 - \frac{(x_1-x_1')^2}{R_2(R_2+x_3+x_3')}\right]\right\}$$

$$G_{21} = C(x_1-x_1')(x_2-x_2')\left[\frac{1}{R_1^3} + \frac{(3-4\nu)}{R_2^3} - \frac{6x_3x_3'}{R_2^5} - \frac{4(1-\nu)(1-2\nu)}{R_2(R_2+x_3+x_3')^2}\right]$$

$$G_{31} = C(x_1-x_1')\left[\frac{x_3-x_3'}{R_1^3} + \frac{(3-4\nu)(x_3-x_3')}{R_2^3} - \frac{6x_3x_3'(x_3+x_3')}{R_2^5} + \frac{4(1-\nu)(1-2\nu)}{R_2(R_2+x_3+x_3')}\right]$$

$$G_{12} = C(x_1-x_1')(x_2-x_2')\left[\frac{1}{R_1^3} + \frac{(3-4\nu)}{R_2^3} - \frac{6x_3x_3'}{R_2^5} - \frac{4(1-\nu)(1-2\nu)}{R_2(R_2+x_3+x_3')^2}\right]$$

$$G_{22} = C\left\{\frac{(3-4\nu)}{R_1} + \frac{1}{R_2} + \frac{(x_2-x_2')^2}{R_1^3} + \frac{(3-4\nu)(x_2-x_2')^2}{R_2^3} + \frac{2x_3x_3'}{R_2^3}\left[1 - \frac{3(x_2-x_2')^2}{R_2^2}\right]\right.$$
$$\left. + \frac{4(1-\nu)(1-2\nu)}{R_2+x_3+x_3'}\left[1 - \frac{(x_2-x_2')^2}{R_2(R_2+x_3+x_3')}\right]\right\}$$

$$G_{32} = C(x_2-x_2')\left[\frac{x_3-x_3'}{R_1^3} + \frac{(3-4\nu)(x_3-x_3')}{R_2^3} - \frac{6x_3x_3'(x_3+x_3')}{R_2^5} + \frac{4(1-\nu)(1-2\nu)}{R_2(R_2+x_3+x_3')}\right]$$

$$G_{13} = C(x_1-x_1')\left[\frac{x_3-x_3'}{R_1^3} + \frac{(3-4\nu)(x_3-x_3')}{R_2^3} + \frac{6x_3x_3'(x_3-x_3')}{R_2^5} - \frac{4(1-\nu)(1-2\nu)}{R_2(R_2+x_3+x_3')}\right]$$

$$G_{23} = C(x_2-x_2')\left[\frac{x_3-x_3'}{R_1^3} + \frac{(3-4\nu)(x_3-x_3')}{R_2^3} + \frac{6x_3x_3'(x_3+x_3')}{R_2^5} - \frac{4(1-\nu)(1-2\nu)}{R_2(R_2+x_3+x_3')}\right]$$

$$G_{33} = C\left[\frac{(3-4\nu)}{R_1} + \frac{8(1-\nu)^2-(3-4\nu)}{R_2} + \frac{(x_3-x_3')^2}{R_1^3} + \frac{(3-4\nu)(x_3+x_3')^2-2x_3x_3'}{R_2^3}\right.$$
$$\left. + \frac{6x_3x_3'(x_3+x_3')^2}{R_2^5}\right]$$

where $\mathbf{x} = (x_1, x_2, x_3)$ is the observation or receiving point; $\mathbf{x}' = (x_1', x_2', x_3')$ is the source point, and

$$R_1 = \sqrt{(x_1-x_1')^2 + (x_2-x_2')^2 + (x_3-x_3')^2}$$
$$R_2 = \sqrt{(x_1-x_1')^2 + (x_2-x_2')^2 + (x_3+x_3')^2}$$
$$C = \frac{1}{16\pi\mu(1-\nu)}$$

6.3 Displacement, strain and stress fields in the infinite space case

Here we explain how the expressions for the displacement $u_r(r,\theta)$, $u_\theta(r,\theta)$ and strain components $e_{ij}(r,\theta)$, reported in subsection 3.2.1, were obtained in the work of Lamberti (2017).
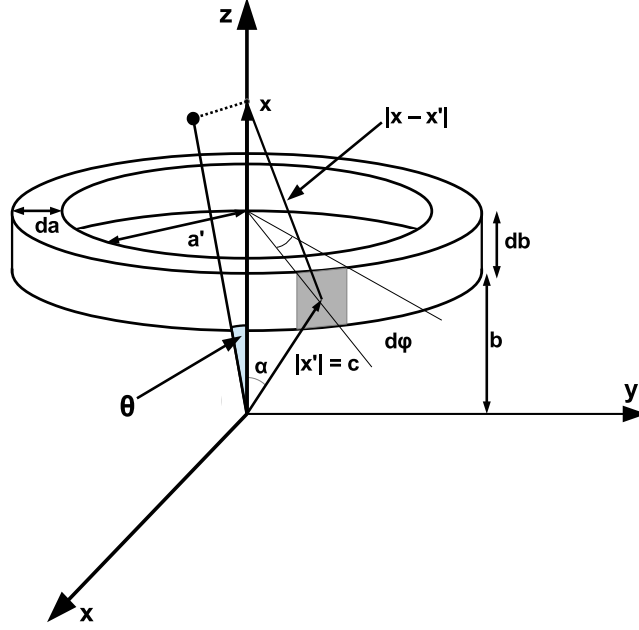
Figure 6.1: Cylinder-shaped source with infinitesimal height db and radius a decomposed into infinite anular rings with width da and radius a'. The point at $\mathbf{x}$ lying on the symmetry axis is where we evaluate the potential Φ, while the point $\mathbf{x}'$ marks an infinitesimal volume element on one infinitesimal ring. The generalisation of point $\mathbf{x}$ to a point off the azimuthal axis is also shown, together with the polar angle θ between the new $\mathbf{x}$ and the z-axis.

Let us start with the assumption of a cylindrical inclusion with radius a and infinitesimal thickness db. If we exploit its azimuthal symmetry, we can first decompose the source into an infinite number of infinitesimal anular rings with radius a', width da and thickness db (as illustrated in fig. 6.1), and then we are able to compute the "infinitesimal" potential field at a point $\mathbf{x}$ on the symmetry axis due to source points $\mathbf{x}'$ on a single ring, employing spherical coordinates (r, θ, ϕ):

$$d\Phi(r) = \frac{dv}{(r^2 + c^2 - 2cr cos\alpha)^{1/2}} \tag{6.3.1}$$

where $r = |\mathbf{x}|$, $c = |\mathbf{x}'|$, $dv = 2\pi a' dadb$ is the infinitesimal ring volume, $c = \sqrt{a'^2 + b^2}$ and $cos\alpha = \frac{b}{c}$, as shown in fig. 6.1.

The potential in eq. 6.3.1 can be rewritten in terms of a Legendre polynomial series by employing the expansion of the inverse of the distance between two generic points $\mathbf{y}$ and $\mathbf{y}'$ (see Jackson, 1999):

$$\frac{1}{|\mathbf{y} - \mathbf{y}'|} = \frac{1}{r_>} \sum_{l=0}^{\infty} \left(\frac{r_<}{r_>}\right)^l P_l(cos\gamma) \tag{6.3.2}$$

where $P_l(cos\gamma)$ is the Legendre polynomial of order l evaluated at $cos\gamma = \frac{\mathbf{y}}{|\mathbf{y}|} \cdot \frac{\mathbf{y}'}{|\mathbf{y}'|}$, $r_<$ and $r_>$ being respectively the smaller and the larger between $|\mathbf{y}|$ and $|\mathbf{y}'|$. Moreover, it is possible (Jackson, 1999) to generalize the expansion of the potential to a point off the symmetry axis, with generic coordinates (r, θ, ϕ), by simply multiplying the expression in eq. 6.3.1 by $P_l(cos\theta)$.

94

The potential can thus be expressed as

$$d\Phi(r,\theta) = \frac{dv}{c}\sum_{l=0}^{\infty}\left(\frac{r}{c}\right)^l P_l(cos\alpha)P_l(cos\theta) \qquad \text{if } r < c \qquad (6.3.3a)$$

$$d\Phi(r,\theta) = \frac{dv}{r}\sum_{l=0}^{\infty}\left(\frac{c}{r}\right)^l P_l(cos\alpha)P_l(cos\theta) \qquad \text{if } r > c \qquad (6.3.3b)$$

The next step is to exploit the recurrence formula

$$(l+1)P_{l+1} - (2l-1)xP_l + lP_{l-1} = 0, \ l \geq 1 \qquad (6.3.4)$$

where x is the argument of the Legendre polynomials, to express the coefficients $P_l(cos\alpha)$ in eqs. 6.3.3a, 6.3.3b.

With reference to fig. 6.1, if we put $b = 0$, then $c = a'$ and $cos\alpha = 0$. After substituting $x = 0$ in eq. 6.3.4 and obtaining a recurrence relation for the coefficients $c_l = P_l(0)$ (according to which the polynomials of odd order vanish, so we will use the notation $2m$ instead of l for the indices of summation), we get a final expression for the potential due to the whole cylinder, by integrating the potential $d\Phi$ with respect to the radius a' from 0 to the source radius a:

$$\Phi(r,\theta) = 2\pi adb\sum_{m=0}^{\infty}c_{2m}P_{2m}(cos\theta)\left[\left(\frac{1}{2m+2}+\frac{1}{2m-1}\right)\frac{r}{a}-\frac{1}{2m-1}\left(\frac{r}{a}\right)^{2m}\right]$$
$$(6.3.5a)$$

if $r \leq a$, internal domain

$$\Phi(r,\theta) = 2\pi adb\sum_{m=0}^{\infty}c_{2m}P_{2m}(cos\theta)\frac{1}{2m+2}\left(\frac{a}{r}\right)^{2m+1} \qquad (6.3.5b)$$

if $r \geq a$, external domain

where "internal" and "external" domains are not to be confused with the inclusion and the surrounding matrix (see fig. 6.2). It can be demonstrated that both the series in eqs. 6.3.5a and 6.3.5b are absolutely convergent at any (r,θ) in $[0,a]\times[0,\pi]$ and $[a,+\infty)\times[0,\pi]$ respectively.

Having computed the scalar potential for an infinitesimally thin cylindrical source in an unlimited space, we are now able to derive the expressions for the displacement field both in the internal and in the external domain by employing eq. 3.2.3. Here, leaving aside the necessary calculations, we confine ourselves to the already reported (eqs. 3.2.11a to 3.2.12b) equations for the displacement components in spherical coordinates (details can be found in the original work, Lamberti, 2017):

$$u_r(r,\theta) = Aa\left[|cos\,\theta| + \sum_{m=1}^{\infty}c_{2m}P_{2m}(cos\,\theta)\frac{2m}{2m-1}\left(\frac{r}{a}\right)^{2m-1}\right] \qquad (6.3.6a)$$

$$u_\theta(r,\theta) = -Aa\left[\text{sgn}(cos\,\theta)\sin\theta - \sum_{m=1}^{\infty}c_{2m}\frac{dP_{2m}}{d\theta}(cos\,\theta)\frac{1}{2m-1}\left(\frac{r}{a}\right)^{2m-1}\right] \qquad (6.3.6b)$$
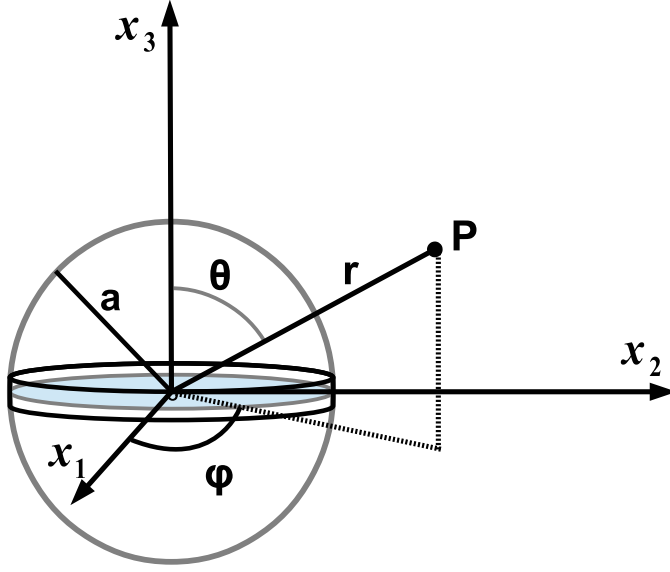
Figure 6.2: Reference system adopted in the work of Lamberti (2017), where the median plane of the thin cylinder (highlighted in blue) embedded in an infinite space lies on the plane $x_3 = 0$, its origin coinciding with that of the system O. The internal domain $r \leq a$ coincides with the sphere of radius a surrounding the cylinder, while the rest of the space represents the external domain $r \geq a$. In this case, the radial distance r of a point P from the origin coincides with the distance from the center of the median plane of the cylinder.

in the internal domain, and

$$u_r(r,\theta) = Aa \sum_{m=0}^{\infty} c_{2m} P_{2m}(\cos\theta) \frac{2m+1}{2m+2} \left(\frac{a}{r}\right)^{2m+2} \tag{6.3.7a}$$

$$u_\theta(r,\theta) = -Aa \sum_{m=1}^{\infty} c_{2m} \frac{dP_{2m}}{d\theta}(\cos\theta) \frac{1}{2m+2} \left(\frac{a}{r}\right)^{2m+2} \tag{6.3.7b}$$

in the external domain, where

$$A = e_1 \frac{db}{2a} \tag{6.3.8}$$

Also in this case, it is possible to show that the series in the expressions 3.2.11a to 3.2.12b are convergent both for $r > a$ and $r < a$, even if they diverge logarithmically when $r \simeq a$ (Lamberti, 2017).

The components of the strain tensor are derived in spherical coordinates for the space outside the inclusion, according to eq. 2.1.1, and they have been reported in eqs. 3.2.20a to 3.2.14h. It is worth noticing that $e_{r\theta}$ is the only non-vanishing shear component, although it vanishes too within the source region (if $\theta = \frac{\pi}{2}$, then $\frac{dP_{2m}(\cos\theta)}{d\theta} = 0$).

After turning them to cylindrical coordinates (ρ, ϕ, z), the strain components are also computed for the region inside the inclusion, taking into account the continu-

ity of displacement and traction across the inclusion surface, as requested by the Eshelby's method.

Finally, the stress tensor components are derived in cylindrical coordinates, both for the isotropic and the deviatoric part, inside and outside the inclusion, by using eqs. 2.1.2 and 2.1.3. Here we report the expressions of the total (isotropic and deviatoric) components according to Lamberti (2017):

$$\tau_{\rho\rho}^{in} = \tau_{\rho\rho}^{out} = 2\mu \left[A \sum_{m=1}^{\infty} c_{2m}^2 2m \left(\frac{r}{a} \right)^{2m-2} - e_1 \right] \tag{6.3.9a}$$

$$\tau_{\phi\phi}^{in} = \tau_{\phi\phi}^{out} = 2\mu \left[A \sum_{m=1}^{\infty} c_{2m}^2 \frac{2m}{2m-1} \left(\frac{r}{a} \right)^{2m-2} - e_1 \right] \tag{6.3.9b}$$

$$\tau_{zz}^{in} = -2\mu A \sum_{m=1}^{\infty} c_{2m}^2 \frac{4m^2}{2m-1} \left(\frac{r}{a} \right)^{2m-2} \tag{6.3.9c}$$

$$\tau_{zz}^{out} = -2\mu \left[A \sum_{m=1}^{\infty} c_{2m}^2 \frac{4m^2}{2m-1} \left(\frac{r}{a} \right)^{2m-2} + e_1 \right] \tag{6.3.9d}$$

together with the expressions of the deviatoric components:

$$\tau_{\rho\rho}^{d,in} = \tau_{\rho\rho}^{d,out} = 2\mu \left[A \sum_{m=1}^{\infty} c_{2m}^2 2m \left(\frac{r}{a} \right)^{2m-2} - \frac{1}{3}e_1 \right] \tag{6.3.10a}$$

$$\tau_{\phi\phi}^{d,in} = \tau_{\phi\phi}^{d,out} = 2\mu \left[A \sum_{m=1}^{\infty} c_{2m}^2 \frac{2m}{2m-1} \left(\frac{r}{a} \right)^{2m-2} - \frac{1}{3}e_1 \right] \tag{6.3.10b}$$

$$\tau_{zz}^{d,in} = -2\mu \left[A \sum_{m=1}^{\infty} c_{2m}^2 \frac{4m^2}{2m-1} \left(\frac{r}{a} \right)^{2m-2} + \frac{1}{3}e_1 \right] \tag{6.3.10c}$$

$$\tau_{zz}^{d,out} = 2\mu \left[\frac{2}{3}e_1 - A \sum_{m=1}^{\infty} c_{2m}^2 \frac{4m^2}{2m-1} \left(\frac{r}{a} \right)^{2m-2} \right] \tag{6.3.10d}$$

where "in" and "out" stand for, respectively, inside and outside the source region. It is to say that, as the shear strain component $e_{r\theta}$ vanishes on the cylinder median plane, also $e_{\rho z} = -e_{r\theta}$ and consequently the stress shear component $\tau_{\rho z}$ vanish on the median plane and, by continuity, within the whole source region $|z| < \frac{db}{2}$ (as the continuity of $\tau_{\rho z}$ and τ_{zz} is required by the Eshelby's method). Thus the stress tensor is diagonal within the source region, and its diagonal elements are the principal stresses.

6.4 Sum of Mindlin's tensor partial derivatives

Here we report the calculation steps necessary to evaluate the sums of the Mindlin's tensor partial derivatives as they are presented in eqs. eqs. 3.2.21, 3.2.27, 3.2.33.

The first sum to be evaluated, relative to the first component of the displacement field, is

$$\frac{\partial G_{11}}{\partial x_1'} + \frac{\partial G_{12}}{\partial x_2'} + \frac{\partial G_{13}}{\partial x_3'}$$

Starting from the summation of the expressions in eqs. 3.2.17, 3.2.18 and 3.2.19 and simplifying the various terms, we get

$$\frac{\partial G_{1k}}{\partial x'_k} = C(x_1 - x'_1)\left\{-\frac{1+4\nu}{R_1^3} + \frac{3}{R_1^3} - \frac{30x_3x'_3}{R_2^5} + \frac{30x_3x'_3}{R_2^5}\right.$$

$$+\frac{3(3-4\nu)(R_2^2 - (x_3 + x'_3)^2 - (x_3 + x'_3)(x_3 - x'_3)}{R_2^5} + \frac{6x_3(x_3 + x'_3)}{R_2^5}$$

$$\left.+\frac{8(1-\nu)(1-2\nu)}{R_2^3} + \frac{1 - 4(3-4\nu)}{R_2^3}\right\}$$

which can be further simplified into

$$\frac{\partial G_{1k}}{\partial x'_k} = C(x_1 - x'_1)\left\{\frac{2(1-2\nu)}{R_1^3} + \frac{2(1-2\nu)(3-4\nu)}{R_2^3} - \frac{12(1-2\nu)x_3(x_3 + x'_3)}{R_2^5}\right\}$$

Continuing with the second displacement component, the sum to be evaluated is

$$\frac{\partial G_{21}}{\partial x'_1} + \frac{\partial G_{22}}{\partial x'_2} + \frac{\partial G_{23}}{\partial x'_3}$$

If we sum the expressions in eqs. 3.2.24, 3.2.25 and 3.2.26, we obtain

$$\frac{\partial G_{2k}}{\partial x'_k} = C(x_2 - x'_2)\left\{-\frac{1+4\nu}{R_1^3} + \frac{3}{R_1^3} - \frac{30x_3x'_3}{R_2^5} + \frac{30x_3x'_3}{R_2^5}\right.$$

$$+\frac{3(3-4\nu)(R_2^2 - (x_3 + x'_3)^2 - (x_3 + x'_3)(x_3 - x'_3)}{R_2^5} + \frac{6x_3(x_3 + x'_3)}{R_2^5}$$

$$\left.+\frac{8(1-\nu)(1-2\nu)}{R_2^3} + \frac{1 - 4(3-4\nu)}{R_2^3}\right\}$$

which, in turns, can be simplified into

$$\frac{\partial G_{2k}}{\partial x'_k} = C(x_2 - x'_2)\left\{\frac{2(1-2\nu)}{R_1^3} + \frac{2(1-2\nu)(3-4\nu)}{R_2^3} - \frac{12(1-2\nu)x_3(x_3 + x'_3)}{R_2^5}\right\}$$

Finally, for the third component, we have to evaluate te sum

$$\frac{\partial G_{31}}{\partial x'_1} + \frac{\partial G_{32}}{\partial x'_2} + \frac{\partial G_{33}}{\partial x'_3}$$

Summing the expressions in eqs. 3.2.30, 3.2.31 and 3.2.32, we get

$$\frac{\partial G_{3k}}{\partial x'_k} = C\left\{-\frac{(1+4\nu)(x_3 - x'_3)}{R_1^3} + \frac{3(x_3 - x'_3)}{R_1^3} - \frac{30x_3x'_3(x_3 + x'_3)}{R_2^5}\right.$$

$$+\frac{30x_3x'_3(x_3 + x'_3)}{R_2^5} + \frac{3(3-4\nu)(R_2^2 - (x_3 + x'_3)^2)(x_3 - x'_3)}{R_2^5} - \frac{3(3-4\nu)(x_3 + x'_3)^3}{R_2^5}$$

$$\left.+\frac{6x_3(x_3 + x'_3)^2}{R_2^5} - \frac{4(1-\nu)(1-2\nu)(x_3 + x'_3)}{R_2^3} + \frac{2(3-4\nu)(2x_3 + x'_3) - 2x_3}{R_2^3}\right\}$$

which can be simplified into

$$\frac{\partial G_{3k}}{\partial x_k'} = C\left\{\frac{2(1-2\nu)(x_3-x_3')}{R_1^3} - \frac{2(1-2\nu)(3-4\nu)(x_3+x_3')}{R_2^3} - \frac{12(1-2\nu)x_3(x_3+x_3')^2}{R_2^5}\right.$$
$$\left.+\frac{4(1-2\nu)x_3}{R_2^3}\right\}$$

To conclude, we resume the final expressions for the three sums of partial derivatives of the Mindlin's tensor:

$$\frac{\partial G_{1k}}{\partial x_k'} = C(x_1-x_1')\left\{\frac{2(1-2\nu)}{R_1^3} + \frac{2(1-2\nu)(3-4\nu)}{R_2^3} - \frac{12(1-2\nu)x_3(x_3+x_3')}{R_2^5}\right\}$$

$$(6.4.1)$$

$$\frac{\partial G_{2k}}{\partial x_k'} = C(x_2-x_2')\left\{\frac{2(1-2\nu)}{R_1^3} + \frac{2(1-2\nu)(3-4\nu)}{R_2^3} - \frac{12(1-2\nu)x_3(x_3+x_3')}{R_2^5}\right\}$$

$$(6.4.2)$$

$$\frac{\partial G_{3k}}{\partial x_k'} = C\left\{\frac{2(1-2\nu)(x_3-x_3')}{R_1^3} - \frac{2(1-2\nu)(3-4\nu)(x_3+x_3')}{R_2^3} - \frac{12(1-2\nu)x_3(x_3+x_3')^2}{R_2^5}\right.$$

$$(6.4.3)$$

$$\left.+\frac{4(1-2\nu)x_3}{R_2^3}\right\}$$

6.5 Curl of the displacement field

Here we explain the calculation we carried out to evaluate the curl of the displacement field.

By definition, the curl inside the volume integral in eq. 3.2.38 is given by

$$e_{ijk}\frac{\partial}{\partial x_j}\left(\frac{\partial G_{km}}{\partial x_m'}\right) = \hat{i}\left(\frac{\partial}{\partial x_2}\frac{\partial G_{3m}}{\partial x_m'} - \frac{\partial}{\partial x_3}\frac{\partial G_{2m}}{\partial x_m'}\right)$$
$$-\hat{j}\left(\frac{\partial}{\partial x_1}\frac{\partial G_{3m}}{\partial x_m'} - \frac{\partial}{\partial x_3}\frac{\partial G_{1m}}{\partial x_m'}\right) + \hat{k}\left(\frac{\partial}{\partial x_1}\frac{\partial G_{2m}}{\partial x_m'} - \frac{\partial}{\partial x_2}\frac{\partial G_{1m}}{\partial x_m'}\right)$$

Substituting the expressions in eqs. 6.4.1, 6.4.2 and 6.4.3 into the previous equation, we can write

$$e_{ijk}\frac{\partial}{\partial x_j}\left(\frac{\partial G_{km}}{\partial x'_m}\right) = \hat{i}\left(-\frac{6(1-2\nu)(x_3-x'_3)(x_2-x'_2)}{R_1^5} + \frac{6(1-2\nu)(3-4\nu)(x_3+x'_3)(x_2-x'_2)}{R_2^5}\right.$$
$$+\frac{60(1-2\nu)x_3(x_3+x'_3)^2(x_2-x'_2)}{R_2^7} - \frac{12(1-2\nu)x_3(x_2-x'_2)}{R_2^5} + \frac{6(1-2\nu)(x_3-x'_3)(x_2-x'_2)}{R_1^5}$$
$$\left.+\frac{6(1-2\nu)(3-4\nu)(x_3+x'_3)(x_2-x'_2)}{R_2^5} - \frac{60(1-2\nu)x_3(x_3+x'_3)^2(x_2-x'_2)}{R_2^7}\right)$$
$$-\hat{j}\left(-\frac{6(1-2\nu)(x_3-x'_3)(x_1-x'_1)}{R_1^5} + \frac{6(1-2\nu)(3-4\nu)(x_3+x'_3)(x_1-x'_1)}{R_2^5}\right.$$
$$+\frac{60(1-2\nu)x_3(x_3+x'_3)^2(x_1-x'_1)}{R_2^7} - \frac{12(1-2\nu)x_3(x_1-x'_1)}{R_2^5} + \frac{6(1-2\nu)(x_3-x'_3)(x_1-x'_1)}{R_1^5}$$
$$\left.+\frac{6(1-2\nu)(3-4\nu)(x_3+x'_3)(x_1-x'_1)}{R_2^5} - \frac{60(1-2\nu)x_3(x_3+x'_3)^2(x_1-x'_1)}{R_2^7}\right)$$
$$+\hat{k}\left(-\frac{6(1-2\nu)(x_1-x'_1)(x_2-x'_2)}{R_1^5} - \frac{6(1-2\nu)(3-4\nu)(x_1+x'_1)(x_2-x'_2)}{R_2^5}\right.$$
$$\left.+\frac{60(1-2\nu)x_3(x_3+x'_3)(x_1-x'_1)(x_2-x'_2)}{R_2^7} - \frac{60(1-2\nu)x_3(x_3+x'_3)(x_1-x'_1)(x_2-x'_2)}{R_2^7}\right)$$

Taking out the vanishing terms and simplifying, we obtain the same expression as in eq. 3.2.39, showing that the displacement field has a non-vanishing curl.

6.6 Converting vectors and tensors between spherical and cartesian coordinates

Here we report the formula necessary to convert a vector $\mathbf{u} = u_r\hat{e}_r + u_\theta\hat{e}_\theta + u_\phi\hat{e}_\phi$ from a spherical basis (r, θ, ϕ) to a cartesian basis (x, y, z):

$$\begin{bmatrix} u_x \\ u_y \\ u_z \end{bmatrix} = \begin{bmatrix} \sin\theta\cos\phi & \cos\theta\cos\phi & -\sin\phi \\ \sin\theta\sin\phi & \cos\theta\sin\phi & \cos\phi \\ \cos\theta & -\sin\theta & 0 \end{bmatrix}\begin{bmatrix} u_r \\ u_\theta \\ u_\phi \end{bmatrix}$$

This transformation would provide the correct expression for $\mathbf{u}$ if the cartesian reference frame is right-handed and the z-axis points upward, as in fig. 6.3 a).

In our case, as we have seen in section 3.3, we have chosen a right-handed reference frame (x_1, x_2, x_3) in which the x_3-axis (vertical) points downward. To obtain such a reference frame starting from the one in fig. 6.3 a), we need to make a rotation of $\frac{\pi}{2}$ about the z-axis, and then a rotation of π about the new y-axis. These are described respectively through the rotation matrices $R^1(\frac{\pi}{2})$ and $R^2(\pi)$:

$$\begin{bmatrix} R^1 \end{bmatrix} = \begin{bmatrix} \cos\alpha & -\sin\alpha & 0 \\ \sin\alpha & \cos\alpha & 0 \\ 0 & 0 & 1 \end{bmatrix} = \begin{bmatrix} 0 & -1 & 0 \\ 1 & 0 & 0 \\ 0 & 0 & 1 \end{bmatrix} =$$

where $\alpha = \frac{\pi}{2}$, and

$$\begin{bmatrix} R^2 \end{bmatrix} = \begin{bmatrix} \cos\beta & 0 & \sin\beta \\ 0 & 1 & 0 \\ -\sin\beta & 0 & \cos\beta \end{bmatrix} = \begin{bmatrix} 0 & -1 & 0 \\ 1 & 0 & 0 \\ 0 & 0 & 1 \end{bmatrix} =$$

where $\beta = \pi$.
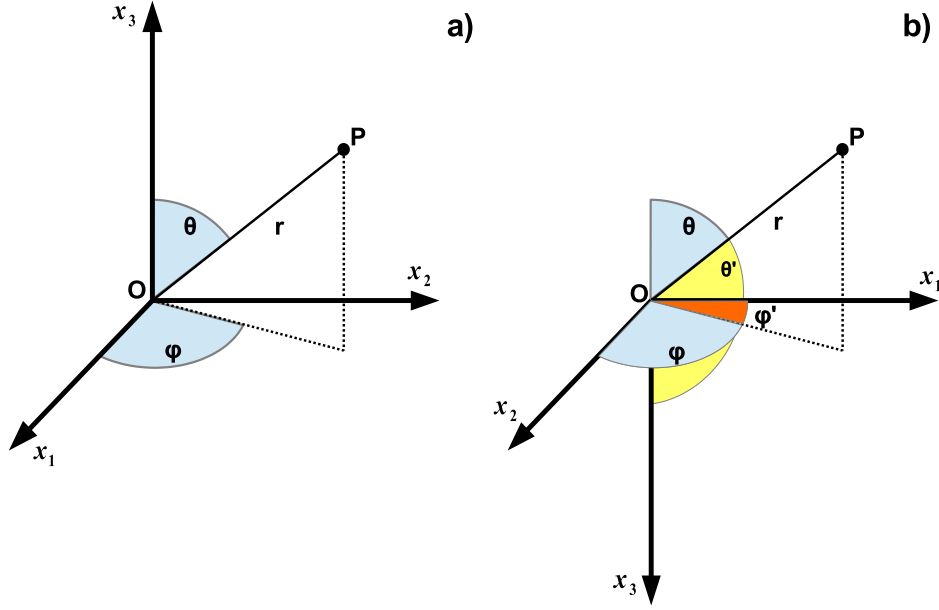
Figure 6.3: a): right-handed cartesian reference frame with the vertical (x_3) axis pointing upward. r, θ, ϕ are a set of spherical coordinates defined according to the following convention: r is the radial distance between the point P and the origin O, θ is the polar angle between the zenith (vertical) direction and the segment OP, and ϕ is the azimuthal angle, measured from the x_1-axis to the projection of OP on the plane $x_1 - x_2$ anticlockwise about the zenith axis. b): the same reference frame after a rotation of $\frac{\pi}{2}$ about the x_3-axis and another rotation of π about the new x_2-axis. The definition of r remains unchanged, while the old angles θ and ϕ are shown together the new ones θ' and ϕ', defined according to the same convention as before.

If we go back to the singular displacement field in subsection 3.2.1, in order to obtain its expression in our cartesian frame, we need first to apply the transformation to get $\mathbf{u}(x, y, z)$, and then apply $R^1(\frac{\pi}{2})$ and $R^2(\pi)$ in this sequence, thus deriving the expressions in eqs. 3.3.18a to 3.3.18c.

Here we report instead the formula necessary to convert a second rank tensor (such as the strain tensor e_{ij}) from a spherical basis (r, θ, ϕ) to a cartesian basis (x, y, z):

$$\begin{bmatrix} e_{xx} & e_{xy} & e_{xz} \\ e_{yx} & e_{yy} & e_{yz} \\ e_{zx} & e_{zy} & e_{zz} \end{bmatrix} =$$

$$\begin{bmatrix} \sin\theta\cos\phi & \cos\theta\cos\phi & -\sin\phi \\ \sin\theta\sin\phi & \cos\theta\sin\phi & \cos\phi \\ \cos\theta & -\sin\theta & 0 \end{bmatrix} \begin{bmatrix} e_{rr} & e_{r\theta} & e_{r\phi} \\ e_{\theta r} & e_{\theta\theta} & e_{\theta\phi} \\ e_{\phi r} & e_{\phi\theta} & e_{\phi\phi} \end{bmatrix} \begin{bmatrix} \sin\theta\cos\phi & \sin\theta\sin\phi & \cos\theta \\ \cos\theta\cos\phi & \cos\theta\sin\phi & -\sin\theta \\ -\sin\phi & \cos\phi & 0 \end{bmatrix}$$

Even in this case we are referring to a cartesian frame in which the vertical z-axis points upward. With reference to section 3.4, if we want to convert the singular strain tensor e_{ij}^s from a spherical set of coordinates to the cartesian one we chose for our problem (fig. 6.3), we need to apply the same rotation matrices $R^1(\frac{\pi}{2})$ and $R^2(\pi)$ we wrote previously:

$$e_{ij}^s(x_1, x_2, x_3) = R^2 R^1 e_{ij}^s(x, y, z) R^{1,T} R^{2,T}$$

where the superscript "T" means the transpose of the matrix. If we develop the necessary calculations, we achieve the expressions in eqs. 3.4.15a to 3.4.15c.

6.7 Evaluation of the non-singular shear stress components

Here we report the expressions of the shear components of the non-singular strain tensor that we omitted in section 3.4:

$$e_{12}^{ns} = \frac{1}{2}\left(\frac{\partial u_1}{\partial x_2} + \frac{\partial u_2}{\partial x_1}\right)$$

$$e_{13}^{ns} = \frac{1}{2}\left(\frac{\partial u_1}{\partial x_3} + \frac{\partial u_3}{\partial x_1}\right)$$

$$e_{23}^{ns} = \frac{1}{2}\left(\frac{\partial u_2}{\partial x_3} + \frac{\partial u_3}{\partial x_2}\right)$$

If we substitute eqs. 3.3.1 to 3.3.3 into the previous expressions and we develop them, we obtain

$$e_{12}^{ns} = B \int_{-a}^{a} dx_1' \int_{-\sqrt{a^2-(x_1')^2}}^{\sqrt{a^2-(x_1')^2}} dx_2' \int_{c-\frac{d}{2}}^{c+\frac{d}{2}} dx_3' \ (x_1 - x_1')(x_2 - x_2')\left[-\frac{(3-4\nu)}{R_2^5} + \frac{10x_3(x_3 + x_3')}{R_2^7}\right]$$

$$(6.7.2a)$$

$$e_{13}^{ns} = B \int_{-a}^{a} dx_1' \int_{-\sqrt{a^2-(x_1')^2}}^{\sqrt{a^2-(x_1')^2}} dx_2' \int_{c-\frac{d}{2}}^{c+\frac{d}{2}} dx_3' \ (x_1 - x_1')\left[-\frac{x_3 + x_3'}{R_2^5} - \frac{2x_3}{R_2^5} + \frac{10x_3(x_3 + x_3')^2}{R_2^7}\right]$$

$$(6.7.2b)$$

$$e_{23}^{ns} = B \int_{-a}^{a} dx_1' \int_{-\sqrt{a^2-(x_1')^2}}^{\sqrt{a^2-(x_1')^2}} dx_2' \int_{c-\frac{d}{2}}^{c+\frac{d}{2}} dx_3' \ (x_2 - x_2')\left[-\frac{x_3 + x_3'}{R_2^5} - \frac{2x_3}{R_2^5} + \frac{10x_3(x_3 + x_3')^2}{R_2^7}\right]$$

$$(6.7.2c)$$

where $B = 18KCe_0(1 - 2\nu)$.

It is possible to demonstrate that $e_{12}^{ns} = 0$ from eq. 6.7.2a, employing the property 3.4.4 to simplify the resolution of the triple integral, which this time does have an analytical solution.

The other strain components have been computed through numerical integration, and we have found that they vanish (or at least show negligible values with respect to those of the diagonal components) both on the median plane domain ($x_3 = c$, $x_2 = 0$, $0 \le x_1 \le 10000$) and on the free surface domain ($x_3 = 0$, $x_2 = 0$, $0 \le x_1 \le 10000$). The non-singular shear stress components can be obtained through the constitutive relation $\tau_{ij}^{ns} = 2\mu e_{ij}^{ns}$, $i \ne j$, and they vanish as well in the considered domains.

Bibliography

Aki, K. and Richards, P. G. (2002). *Quantitative seismology.*

Amoruso, A., Crescentini, L., and Berrino, G. (2008). Simultaneous inversion of deformation and gravity changes in a horizontally layered half-space: evidences for magma intrusion during the 1982–1984 unrest at campi flegrei caldera (italy). *Earth and Planetary Science Letters*, 272(1-2):181–188.

Arienzo, I., Moretti, R., Civetta, L., Orsi, G., and Papale, P. (2010). The feeding system of agnano–monte spina eruption (campi flegrei, italy): Dragging the past into present activity and future scenarios. *Chemical Geology*, 270(1-4):135–147.

Babbage, C. (1847). Observations on the temple of serapis, at pozzuoli, near naples, with remarks on certain causes which may produce geological cycles of great extent. *Quarterly Journal of the Geological Society*, 3(1-2):186–217.

Battaglia, M., Troise, C., Obrizzo, F., Pingue, F., and Natale, G. D. (2006). Evidence for fluid migration as the source of deformation at campi flegrei caldera (italy). *Geophysical Research Letters*, 33(1).

Berrino, G., Corrado, G., Luongo, G., and Toro, B. (1984). Ground deformation and gravity changes accompanying the 1982 pozzuoli uplift. *Bulletin volcanologique*, 47(2):187–200.

Biot, M. A. (1941). General theory of three-dimensional consolidation. *Journal of applied physics*, 12(2):155–164.

Bonafede, M., Dragoni, M., and Quareni, F. (1986). Displacement and stress fields produced by a centre of dilation and by a pressure source in a viscoelastic half-space: Application to the study of ground deformation and seismic activity at campi flegrei, italy. *Geophysical Journal of the Royal Astronomical Society*, 87(2):455–485.

Bonafede, M. and Ferrari, C. (2009). Analytical models of deformation and residual gravity changes due to a mogi source in a viscoelastic medium. *Tectonophysics*, 471(1-2):4–13.

Brace, W. and Kohlstedt, D. (1980). Limits on lithospheric stress imposed by laboratory experiments. *Journal of Geophysical Research: Solid Earth*, 85(B11):6248–6252.

Breislak, S. (1798). *Topografia fisica della Campania.* Nella Stamperia di Antonio Brazzini.

Chiarabba, C. and Moretti, M. (2006). An insight into the unrest phenomena at the campi flegrei caldera from vp and vp/vs tomography. *Terra Nova*, 18(6):373–379.

Chiodini, G., Selva, J., Pezzo, E., Marsan, D., Siena, L., D'auria, L., Bianco, F., Caliro, S., Martino, P., Ricciolino, P., et al. (2017). Clues on the origin of post-2000 earthquakes at campi flegrei caldera (italy). *Scientific reports*, 7(1):4472.

Chiodini, G., Vandemeulebrouck, J., Caliro, S., D'Auria, L., Martino, P. D., Mangiacapra, A., and Petrillo, Z. (2015). Evidence of thermal-driven processes triggering the 2005–2014 unrest at campi flegrei caldera. *Earth and Planetary Science Letters*, 414:58–67.

Colella, A., Benedetto, C. D., Calcaterra, D., Cappelletti, P., D'Amore, M., Di Martire, D., Graziano, S., Papa, L., de Gennaro, M., and Langella, A. (2017). The neapolitan yellow tuff: an outstanding example of heterogeneity. *Construction and Building Materials*, 136:361–373.

D'Auria, L., Massa, B., Cristiano, E., Gaudio, C. D., Giudicepietro, F., Ricciardi, G., and Ricco, C. (2014). Retrieving the stress field within the campi flegrei caldera (southern italy) through an integrated geodetical and seismological approach. *Pure and Applied Geophysics*, 172(11):3247–3263.

D'Auria, L., Pepe, S., Castaldo, R., Giudicepietro, F., Macedonio, G., Ricciolino, P., Tizzani, P., Casu, F., Lanari, R., Manzo, M., et al. (2015). Magma injection beneath the urban area of naples: a new mechanism for the 2012–2013 volcanic unrest at campi flegrei caldera. *Scientific reports*, 5:13100.

Davis, P. M. (1986). Surface deformation due to inflation of an arbitrarily oriented triaxial ellipsoidal cavity in an elastic half-space, with reference to kilauea volcano, hawaii. *Journal of Geophysical Research: Solid Earth*, 91(B7):7429–7438.

De Vivo, B. (2006). *Volcanism in the Campania Plain: Vesuvius, Campi Flegrei and Ignimbrites*, volume 9. Elsevier.

Di Vito, M. A., Acocella, V., Aiello, G., Barra, D., Battaglia, M., Carandente, A., Gaudio, C. D., Vita, S. D., Ricciardi, G. P., Ricco, C., et al. (2016). Magma transfer at campi flegrei caldera (italy) before the 1538 ad eruption. *Scientific reports*, 6:32245.

Di Vito, M. A., Isaia, R., Orsi, G., Southon, J. D., Vita, S. D., d'Antonio, M., Pappalardo, L., and Piochi, M. (1999). Volcanism and deformation since 12,000 years at the campi flegrei caldera (italy). *Journal of Volcanology and Geothermal Research*, 91(2-4):221–246.

Dvorak, J. J. and Berrino, G. (1991). Recent ground movement and seismic activity in campi flegrei, southern italy: Episodic growth of a resurgent dome. *Journal of Geophysical Research: Solid Earth*, 96(B2):2309–2323.

Dvorak, J. J. and Mastrolorenzo, G. (1991). *The mechanisms of recent vertical crustal movements in Campi Flegrei caldera, southern Italy*, volume 263. Geological Society of America.

Eshelby, J. D. (1957). The determination of the elastic field of an ellipsoidal inclusion, and related problems. *Proc. R. Soc. Lond. A*, 241(1226):376–396.

Ferrari, C., Bonafede, M., and Belardinelli, M. E. (2016). Libhalfspace: A c++ object-oriented library to study deformation and stress in elastic half-spaces. *Computers & geosciences*, 96:136–146.

Fialko, Y., Khazan, Y., and Simons, M. (2001). Deformation due to a pressurized horizontal circular crack in an elastic half-space, with applications to volcano geodesy. *Geophysical Journal International*, 146(1):181–190.

Gaeta, F. S., Peluso, F., Arienzo, I., Castagnolo, D., Natale, G. D., Milano, G., Albanese, C., and Mita, D. G. (2003). A physical appraisal of a new aspect of bradyseism: The miniuplifts. *Journal of Geophysical Research: Solid Earth*, 108(B8).

Gaudio, C. D., Aquino, I., Ricciardi, G. P., Ricco, C., and Scandone, R. (2010). Unrest episodes at campi flegrei: A reconstruction of vertical ground movements during 1905–2009. *Journal of Volcanology and Geothermal Research*, 195(1):48–56.

Gradshteyn, I. S. and Ryzhik, I. M. (2014). *Table of integrals, series, and products.* Academic press.

Jackson, J. D. (1999). Classical electrodynamics.

Judenherc, S. and Zollo, A. (2004). The bay of naples (southern italy): Constraints on the volcanic structures inferred from a dense seismic survey. *Journal of Geophysical Research: Solid Earth*, 109(B10).

Lamberti, I. (2017). Modelling the stress field induced by changes in temperature and pore pressure in a volcanic region. Bachelor's thesis, Scuola di Scienze, Dipartimento di Fisica e Astronomia, Università di Bologna.

Lima, A., Vivo, B. D., Spera, F. J., Bodnar, R. J., Milia, A., Nunziata, C., Belkin, H. E., and Cannatelli, C. (2009). Thermodynamic model for uplift and deflation episodes (bradyseism) associated with magmatic–hydrothermal activity at the campi flegrei (italy). *Earth-Science Reviews*, 97(1-4):44–58.

Love, A. (1927). *The mathematical theory of elasticity.*

Macedonio, G., Giudicepietro, F., D'auria, L., and Martini, M. (2014). Sill intrusion as a source mechanism of unrest at volcanic calderas. *Journal of Geophysical Research: Solid Earth*, 119(5):3986–4000.

Mindlin, R. D. (1936). Force at a point in the interior of a semi-infinite solid. *Physics*, 7(5):195–202.

Mogi, K. (1958). Relations between the eruptions of various volcanoes and the deformations of the ground surfaces around them. *Earthq Res Inst*, 36:99–134.

Moretti, R., Arienzo, I., Orsi, G., Civetta, L., and D'Antonio, M. (2013). The deep plumbing system of ischia: A physico-chemical window on the fluid-saturated and co2-sustained neapolitan volcanism (southern italy). *Journal of Petrology*, 54(5):951–984.

Moretti, R., Troise, C., Sarno, F., and Natale, G. D. (2018). Caldera unrest driven by co 2-induced drying of the deep hydrothermal system. *Scientific reports*, 8(1):8309.

Natale, G. D., Troise, C., Mark, D., Mormone, A., Piochi, M., Vito, M. A. D., Isaia, R., Carlino, S., Barra, D., and Somma, R. (2016). The campi flegrei deep drilling project (cfddp): New insight on caldera structure, evolution and hazard implications for the naples area (southern italy). *Geochemistry, Geophysics, Geosystems*, 17(12):4836–4847.

Okada, Y. (1992). Internal deformation due to shear and tensile faults in a half-space. *Bulletin of the Seismological Society of America*, 82(2):1018–1040.

Parascandola, A. (1947). *I fenomeni bradisismici del Serapeo di Pozzuoli*. Stabilmento tipografico G. Genovese.

Stefansson, R., Bonafede, M., and Gudmundsson, G. B. (2011). Earthquake-prediction research and the earthquakes of 2000 in the south iceland seismic zone. *Bulletin of the Seismological Society of America*, 101(4):1590–1617.

Trasatti, E., Bonafede, M., Ferrari, C., Giunchi, C., and Berrino, G. (2011). On deformation sources in volcanic areas: modeling the campi flegrei (italy) 1982–84 unrest. *Earth and Planetary Science Letters*, 306(3-4):175–185.

Trasatti, E., Polcari, M., Bonafede, M., and Stramondo, S. (2015). Geodetic constraints to the source mechanism of the 2011–2013 unrest at campi flegrei (italy) caldera. *Geophysical Research Letters*, 42(10):3847–3854.

Troise, C., Natale, G. D., Schiavone, R., Somma, R., and Moretti, R. (2018). The campi flegrei caldera unrest: Discriminating magma intrusions from hydrothermal effects and implications for possible evolution. *Earth-Science Reviews*.

Yang, X.-M., Davis, P. M., and Dieterich, J. H. (1988). Deformation from inflation of a dipping finite prolate spheroid in an elastic half-space as a model for volcanic stressing. *Journal of Geophysical Research: Solid Earth*, 93(B5):4249–4257.

Zencher, F., Bonafede, M., and Stefansson, R. (2006). Near-lithostatic pore pressure at seismogenic depths: a thermoporoelastic model. *Geophysical Journal International*, 166(3):1318–1334.

Zollo, A., Maercklin, N., Vassallo, M., Iacono, D. D., Virieux, J., and Gasparini, P. (2008). Seismic reflections reveal a massive melt layer feeding campi flegrei caldera. *Geophysical Research Letters*, 35(12).